UNIVERSIDADE DE SÃO PAULO
INSTITUTO DE FÍSICA DE SÃO CARLOS

Matheus Fernandes Sousa Lemes

Study of light-matter interaction in single-layer molybdenum disulfide coupled to gold structures

São Carlos

2023

Matheus Fernandes Sousa Lemes

Study of light-matter interaction in single-layer molybdenum disulfide coupled to gold structures

Dissertation presented to the Graduate Program in Physics at the Instituto de Física de São Carlos da Universidade de São Paulo, to obtain the degree of Master in Science.

Concentration area: Theoretical and Experimental Physics

Advisor: Prof. Dr. Euclydes Marega Junior

Correct version

(Original version available on the Program Unit)

São Carlos

2023

Lemes, Matheus Fernandes Sousa
Study of light-matter interaction in single-layer molybdenum disulfide coupled to gold structures / Matheus Fernandes Sousa Lemes; advisor Euclydes Marega Junior - corrected version -- São Carlos 2023.
99 p.

Dissertation (Master's degree - Graduate Program in Theoretical and Experimental Physics) -- Instituto de Física de São Carlos, Universidade de São Paulo - Brasil , 2023.

1. Transition-metal dichalcogenides. 2. Plasmonics. 3. Light-matter interaction. 4. Raman and photoluminescence spectroscopy. I. Marega Junior, Euclydes, advisor. II. Title.

To God be the glory always, because He is worthy.

ACKNOWLEDGEMENTS

First and foremost, I would like to thank God, because without Him I would not be here and I would certainly not have completed this work. Thank you Jesus for giving purpose to my life purpose and filling my heart with love.

Also, I would like to express my gratitude to my parents, Marcia and Gerson. Thank you for all the love, encouragement, and belief. I love you.

To my advisor Prof. Euclydes Marega Junior, thank you for giving me the opportunity to help the development of physics.

To my friend and colleague Ana Clara, I cannot express how grateful I am for all the help, fruitful discussions, and joyful moments.

To all my friends from São Carlos, who have become my family. Victor, Isa, Julia, Alysson, Andressa, Jennifer, Gabi, Lucas, Pr. Cido, Samuel, Carina, Simone, Paulo, Ju, Humberto, Mateus, Jonas, and many others, thank you for all the love, the laugh, the tears. Thank you for just being there for me.

To my colleagues from Room 3, thank you for making my work days easier and funnier.

To Prof. Andras Kis and Guilherme Marega, thank you for the collaboration in providing the samples.

To Prof. Marcio Daldin, Gabriel, Alessandra, and Vinicius, thank you for the collaboration regarding the photoluminescence measurements.

To Marcelo de Assumpção, thank you for the collaboration in the AFM measurements.

To the Brazilian agencies Coordenação de Aperfeiçoamento de Pessoal de Nível Superior – Brazil (CAPES) (grant 88887.609043/2021-00) and Fundação de Amparo à Pesquisa do Estado de São Paulo (FAPESP) who financed this work, thank you for supporting science in Brazil.

Again, many thanks to everybody.

"If the whole universe has no meaning, we should never have found out that it has no meaning: just as if there were no light in the universe and therefore no creatures with eyes, we should never know it was dark. Dark would be without meaning."
C. S. Lewis

"The more I study nature, the more I stand amazed at the work of the Creator. Science brings men nearer to God."
Louis Pasteur

"For God so loved the world that he gave his one and only Son, that whoever believes in him shall not perish but have eternal life."
John 3.16

ABSTRACT

LEMES, M. F. S. **Study of light-matter interaction in single-layer molybdenum disulfide coupled to gold structures**. 2023. 99p. Dissertation (Master in Science) - Instituto de Física de São Carlos, Universidade de São Paulo, São Carlos, 2023.

This dissertation studies the light-matter interactions in MoS_2 monolayers deposited over gold gratings. We aim to characterize this hybrid device's morphological, vibrational, and optical properties. Our investigation started with the characterization of the semiconductor film morphology in different sample regions. We observed large height deformations for the MoS_2 monolayer in the gratings, along with various defects. Then, Raman spectroscopy was used to study the vibrational properties of the two most pronounced Raman modes of MoS_2, namely the E' and A_1' modes. Raman hyperspectral maps showed that the peak positions of those modes are susceptible to the underlying spatial distribution. In particular, by constructing a correlative plot of the A_1' vs. E' peak frequencies, we could evaluate the contributions of strain, doping, and plasmonic effects on the frequency changes of those modes. Interestingly, we observed that the electron concentration on the gold gratings depends on the polarization of the incident radiation, which was attributed to a plasmon-induced hot electron injection. Finally, the emission of exciton and trion states was investigated using photoluminescence (PL) spectroscopy. Partial PL quenching of the MoS_2 over the gold substrate reveals the existence of charge transfer from the semiconductor to the metal. However, the charge transfer is not particularly efficient, probably due to air and water contaminations between the film and substrate that prevents good direct contact. We also observed a polarization-dependent trion to A exciton ratio, which further corroborated the existence of a plasmon-induced doping mechanism. These findings may help elucidate some underlying physics in hybrid MoS_2/Au nanostructures, which can benefit fundamental studies and technological applications.

Keywords: Transition-metal dichalcogenides. Plasmonics. Light-matter interaction. Raman and photoluminescence spectroscopy.

RESUMO

LEMES, M. F. S. **Estudo da interação luz-matéria em monocamadas de dissulfeto de molibdênio acopladas a estruturas de ouro**. 2023. 99p. Dissertação (Mestrado em Ciências) - Instituto de Física de São Carlos, Universidade de São Paulo, São Carlos, 2023.

Esta dissertação apresenta um estudo das interações radiação-matéria em monocamadas de MoS_2 depositadas sobre grades de ouro. Nosso objetivo é caracterizar as propriedades morfológicas, vibracionais e ópticas deste dispositivo híbrido. Em nossa investigação, começamos com a caracterização da morfologia do filme semicondutor em diferentes regiões da amostra. Observamos deformações de altura muito grandes para a monocamada MoS_2 nas grades, juntamente com uma variedade de defeitos. Em seguida, a espectroscopia Raman foi usada para estudar as propriedades vibracionais dos dois modos Raman mais pronunciados do MoS_2, ou seja, os modos E' e A_1'. Os mapas hiperespectrais Raman mostraram que as posições de pico desses modos são altamente sensíveis à distribuição espacial subjacente. Em particular, ao construir um gráfico correlativo das frequências de pico A_1' vs E', pudemos avaliar as contribuições de tensão mecânica, dopagem e efeitos plasmônicos nas mudanças de frequência desses modos. Observamos de forma interessante que a concentração de elétrons nas grades de ouro varia dependendo da polarização da radiação incidente. Essa variação foi atribuída à injeção de elétrons quentes induzida por plasmons. Finalmente, a emissão dos estados exciton e trion foi investigada usando espectroscopia de fotoluminescência (PL). A extinção parcial de PL do MoS_2 sobre o substrato de ouro revela a existência de uma transferência de carga do semicondutor para o metal. No entanto, a transferência de carga não é particularmente eficiente, provavelmente devido à contaminações de ar e água entre o filme e o substrato que impedem um bom contato direto. Também observamos uma relação de trion para éxciton dependente de polarização, o que corroborou ainda mais a existência de um mecanismo de dopagem induzido por plasmons. Essas contribuições podem ajudar a elucidar parte da física subjacente em nanoestruturas híbridas de MoS_2/Au, que podem beneficiar tanto os estudos fundamentais quanto as aplicações tecnológicas.

Palavras-chave: Dicalcogenetos de metais de transição. Plasmônica. Interação luz matéria. Espectroscopia Raman e de fotoluminescência.

LIST OF FIGURES

LIST OF TABLES

LIST OF ABBREVIATIONS AND ACRONYMS

AFM	atomic force microscopy
2D	two-dimensional
BZ	Brillouin zone
CB	conduction band
DFT	density functional theory
FWHM	full width at half maximum
h-BN	hexagonal boron nitride
LSP	localized surface plasmon
MoS_2	molybdenum disulphide
$MoSe_2$	molybdenum diselenide
PL	photoluminescence
SOC	spin-orbit coupling
SPP	surface plasmon polaritons
TMD	transition metal dichalcogenide
VB	valence band
WS_2	tungsten disulphide
WSe_2	tungsten diselenide

LIST OF SYMBOLS

Å	angstrom
$\delta_{i,j}$	Kronecker delta
π	pi
Δ	energy gap
τ	valley index
$\hat{\sigma}_{x,y,z}$	pauli spin matrices
$\varepsilon(\omega)$	dielectric function
ε_0	vacuum dielectric constant
β	SPP wavevector
λ	wavelength

CONTENTS

1 INTRODUCTION

Since the discovery of graphene in 2004, an impressive surge in developing other 2D materials has followed. Some examples are transition metal dichalcogenides (TMDs) (e.g. molybdenum disulfide (MoS_2), molybdenum diselenide ($MoSe_2$), tungsten disulfide (WS_2), etc.), hexagonal boron nitride (h-BN), silicene (2D silicon) and many others (see Fig. 1). In particular, TMDs exhibit distinctive electrical and optical properties that have attracted tremendous scientific and technological interest in electronics and optoelectronics. For instance, monolayers of MoS_2 can sustain current densities 50 times larger than copper (1) and have stiffness comparable to stainless steel. (2) TMDs transition from indirect bandgap semiconductors in the bulk form to direct bandgap semiconductors when thinned to a monolayer. These characteristics make them promising candidates for developing ultra-small and low-power transistors, solar cells, photo-detectors, and light-emitting diodes. (3–9)

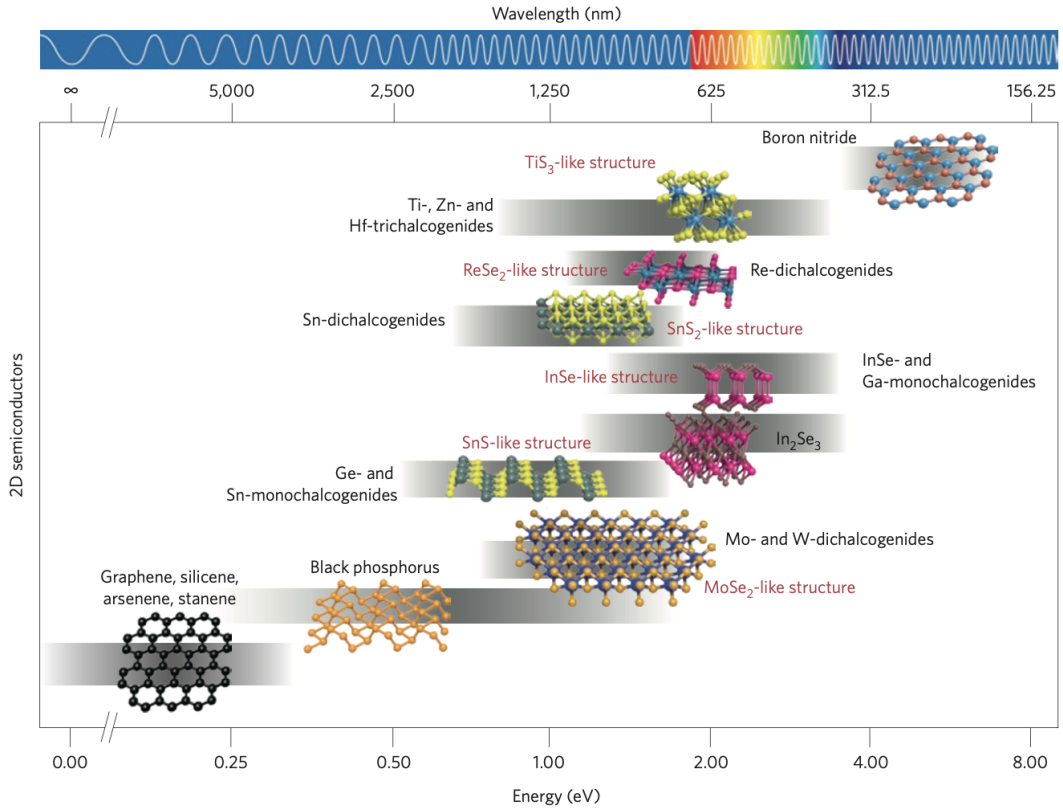

Figure 1 – Comparison of bandgap values (wavelength and energy) for representative two-dimensional materials.

Source: CASTELLANOS-GOMEZ. (10)

However, TMD monolayers have a low optical cross-section due to their atomic thickness, which results in low light absorption (11, 12) and hinders their systematic use in applications based on light-matter interaction. Various designed systems have been studied to improve this interaction in 2D materials, such as chemical treatment (13) and quantum doping (14), but they suffer from a high degree of complexity for practical implementation. One effective way to enhance the optical response of TMD monolayers relies on using plasmonic metal nanomaterials that localize and enhance the electromagnetic field within their proximity. (15–17) Plasmonic devices alone offer a wide range of applications based on extreme light concentration such as nanophotonic lasers (18), biochemical sensors (19), and optical metamaterials (20) (see Fig. 2). In the context of 2D materials, plasmonic nanostructures can increase the optical path length of light through scattering, boost light trapping and improve the performance of the TMD monolayers. (21–23)

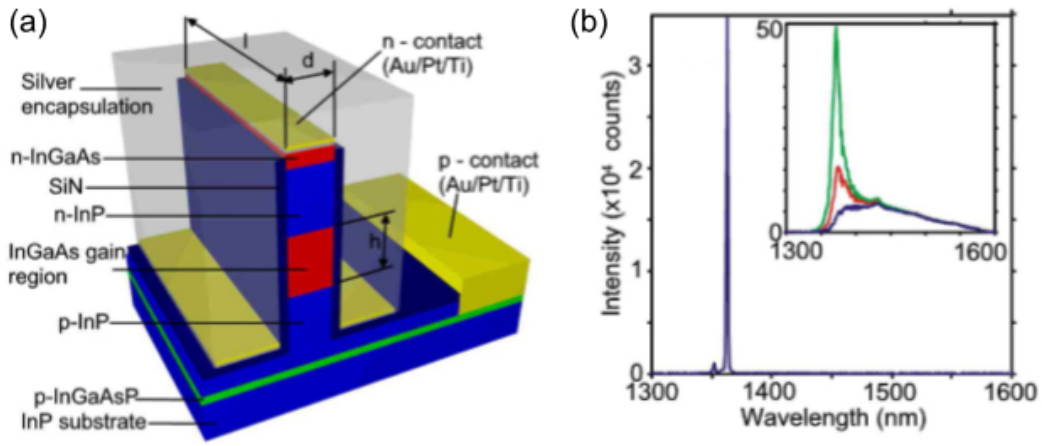

Figure 2 – (a) Schematic representation of a Fabry-Pérot metal-clad plasmonic laser. (b) Laser spectrum at 10 K for the device above the lasing threshold. The inset shows emission spectra below the threshold.

Source: Adapted from HILL *et al.* (24)

This dissertation investigates the structural and optical properties of the MoS_2 monolayer coupled to gold nanostructures in different geometric configurations. First, we provide some theoretical background on the physical concepts presented in this work, focusing on the most relevant aspects needed to follow along. Second, we describe the methods and experimental setup used for growth and characterization. Then, our results are presented and discussed. Finally, we summarize the key points of this work and outline possible routes on this research topic.

2 TRANSITION METAL DICHALCOGENIDES

In this chapter, a general introduction to the TMDs will be presented since a comprehensive description of the field is impossible, given its extent and depth. We discuss the fundamental aspects of these materials relevant to this dissertation, with special attention to the MoS_2 monolayer.

2.1 Crystal structure

TMDs have the general formula MX_2, where M is a transition metal of the groups 4–7 (e.g., W, Mo, Ta, Ti, Nb, and Re) and X is a chalcogen such as S, Se, or Te. Every individual unit is composed of a transition metal layer sandwiched between two chalcogen layers with the M-X bonds predominantly covalent in nature, whereas weak van der Waals forces couple the different units (25) (see Fig. 3a). The TMD monolayer is arranged in a 2D hexagonal Bravais lattice (see Fig. 3b), defined by the two lattice vectors:

$$\begin{cases} \mathbf{a}_1 = \frac{a}{2}\left(\mathbf{x} + \sqrt{3}\mathbf{y}\right) \\ \mathbf{a}_2 = \frac{a}{2}\left(\mathbf{x} - \sqrt{3}\mathbf{y}\right). \end{cases} \tag{2.1}$$

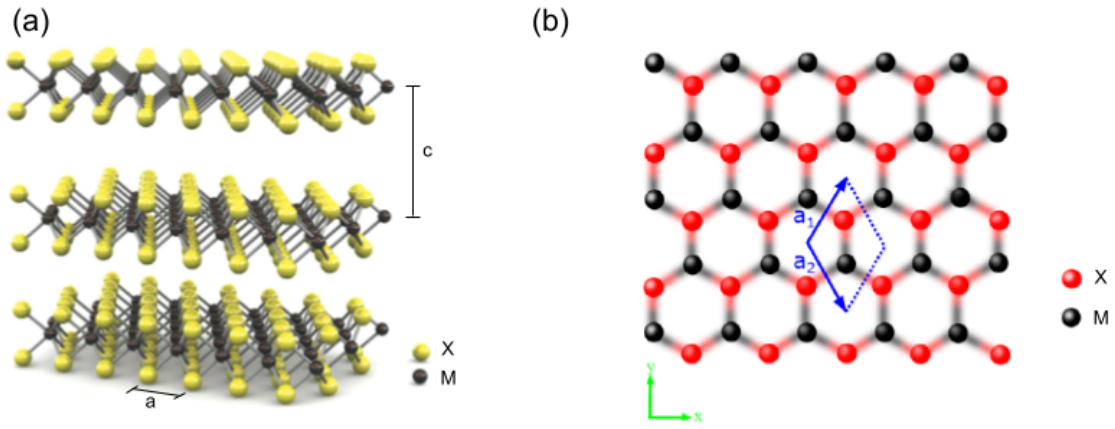

Figure 3 – (a) Three-dimensional representation of an MX_2 structure, in which M represents transition metal atoms (yellow) and X represents chalcogen atoms (black). The lattice constant is a and the interlayer spacing is c. (b) Top view of the same TMD monolayer.

Source: (a) Adapted from RADISAVLJEVIC *et al.* (3); (b) Adapted from LÓPEZ *et al.* (26)

Depending on the atomic stacking configurations, 2D TMDs can be categorized as trigonal prismatic (2H) or octahedral (1T) (see Fig. 4). In the 2H phase, each M atom

is prismatically coordinated with six surrounding X atoms. In contrast, T-phase has a trigonal chalcogen layer on the top and a 180-degree rotated structure at the bottom, forming a distorted octahedron.

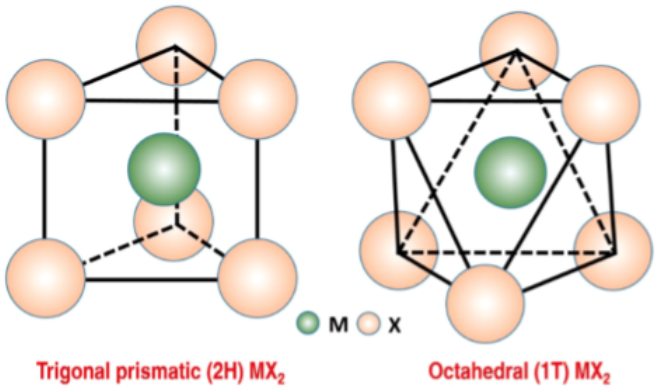

Figure 4 – Unit cell structures of 2H-phase and 1T-phase.

Source: LV *et al.* (27)

The most studied TMD is the MoS_2 monolayer, which has a lattice constant $a = 3.16\,\text{Å}$ and a interlayer spacing $c = 6.5\,\text{Å}$. (3, 28) Also, it is naturally found in the 2H-phase since it has been shown that the 1T-phase is thermodynamically unstable and it returns to the trigonal prismatic structure at room temperature. (29) However, it has been demonstrated that 2H-MoS_2 can be converted into 1T-MoS_2 by intercalating Li or K (30), with the 1T-phase appearing to be a more active hydrogen evolution catalyst than the 2H-phase. (31, 32)

2.2 Electronic properties

2.2.1 Band structure

In this section and the following ones from this chapter, we focus on the MoS_2 material, but the general description should also apply to MoX_2 and WX_2 compounds. To describe any material's electronic properties, the crystal structure's reciprocal lattice needs to be constructed. In the case of 2D materials, the reciprocal lattice is defined by the primitive vectors $\mathbf{b}_1$ and $\mathbf{b}_2$. If the primitive vectors in the direct lattice are $\mathbf{a}_1$ and $\mathbf{a}_2$, then the vectors in the reciprocal lattice can be constructed by satisfying the condition (33)

$$\mathbf{a}_i \cdot \mathbf{b}_j = 2\pi\delta_{ij}, \tag{2.2}$$

where $i, j = 1, 2$ and δ_{ij} is the Kronecker delta.

In the case of the primitive vectors $\mathbf{a}_1$ and $\mathbf{a}_2$ for the TMD monolayer, the vectors $\mathbf{b}_1$ and $\mathbf{b}_2$ are:

$$\begin{cases} \mathbf{b}_1 = \frac{2\pi}{a}\left(\mathbf{x} + \frac{1}{\sqrt{3}}\mathbf{y}\right), \\ \mathbf{b}_2 = \frac{2\pi}{a}\left(\mathbf{x} - \frac{1}{\sqrt{3}}\mathbf{y}\right). \end{cases} \tag{2.3}$$

The primitive cell of the reciprocal lattice is known as the first Brillouin zone (BZ), and it is depicted in Fig 5 for the case of 2D materials.

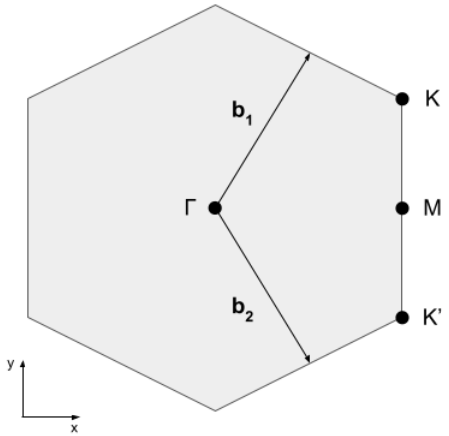

Figure 5 – First Brillouin zone of TMD monolayer with high-symmetry points shown.

Source: By the author.

Usually, bulk TMDs are indirect bandgap semiconductors with a valence band (VB) maximum at the Γ point and a conduction band (CB) minimum at the midpoint along the Γ- K symmetry line. However, when thinned to a monolayer, it becomes a direct bandgap semiconductor located at the K point. This transition was first observed by SPLENDIANI *et al.* with the MoS_2 material (34) and it is depicted in Fig 6 both theoretically (DFT calculations) and experimentally (photoluminescence emission).

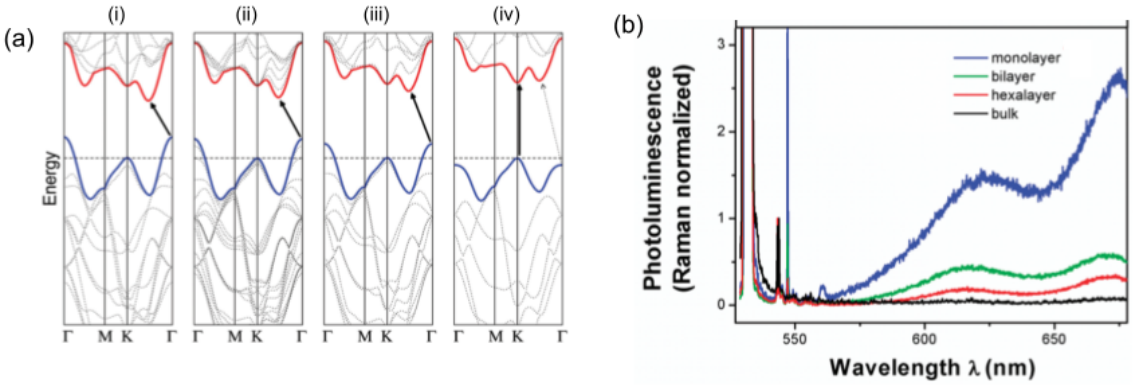

Figure 6 – (a) Band structures calculated from first-principles density functional theory (DFT) for bulk (i), quadrilayer (ii), bilayer (iii), and monolayer (iv) MoS_2. (b) Photoluminescence (Raman normalized) spectra of MoS_2 monolayer, bilayer, hexalayer, and bulk sample. The indirect bandgap is ∼1.2 eV and the direct bandgap is ∼1.9 eV.

Source: Adapted from SPLENDIANI *et al.* (34)

The change in the electronic band structure of the MoS_2 as a function of layer number can be understood in terms of the electron orbitals of different wave vectors and quantum confinement (see Sec. 2.3). The DFT (density functional theory) calculations from SPLENDIANI *et al.* showed that the conduction band states at the K point are primarily due to localized d orbitals at the Mo sites. Since the transition atoms are located in the middle of the unit cell, they have a small interlayer coupling and are unaffected by the change in layer number. In contrast, the states near the Γ point at the valence band and the point of the indirect bandgap at the Γ- K symmetry line on the conduction band originate from a linear combination of d orbitals on the Mo atoms and antibonding p_z orbitals on the S atoms. This results in strong interlayer coupling, consequently leading to a great dependency on the layer thickness.

2.2.2 Spin-orbit coupling

In the monolayer limit, the inversion symmetry of the TMDs is broken since taking the M atom as the inversion center would map the X atom to an empty location. As a consequence, the spin-orbit coupling (SOC) effect is expected to occur in this case. (35) To understand the physics of the TMD monolayer, we can take the MoS_2 as a prototypical example. By constructing a minimal band model based on general symmetry consideration, the two-band $k \cdot p$ Hamiltonian of MoS_2 close to the K point has the form (36):

$$\hat{H}_0 = at\left(\tau k_x \hat{\sigma}_x + k_y \hat{\sigma}_y\right) + \frac{\Delta}{2}\hat{\sigma}_z, \tag{2.4}$$

where $\hat{\sigma}$ denotes the Pauli matrices for the two basis functions, a is the lattice constant, t the effective hopping integral, τ the valley index and Δ the energy gap. In this context,

the term “valley” indicates a local minimum of the band structure and for the case of the TMD monolayer, they are located at the K points (see Fig. 5).

The conduction-band-edge state mostly comprises d_{z^2} orbitals, which makes the first-order SOC splitting vanish. On the contrary, the valence-band-edge state splits since it is primarily composed of metallic orbitals $\frac{1}{\sqrt{2}}(d_{x^2-y^2} \pm id_{xy})$. Approximating the SOC by the intra-atomic contribution $\mathbf{L} \cdot \mathbf{S}$, the total Hamiltonian is given by (36)

$$\hat{H} = at(\tau k_x \hat{\sigma}_x + k_y \hat{\sigma}_y) + \frac{\Delta}{2}\hat{\sigma}_z - \lambda\tau\frac{\hat{\sigma}_z - 1}{2}\hat{s}_z, \tag{2.5}$$

where 2λ is the spin splitting at the valence band top caused by the SOC and $\hat{\sigma}_z$ is the Pauli matrix for a spin. Typical values for the spin splitting in VB of TMD monolayers range from 150 meV in MoS_2 to 430 meV in WS_2. Additionally, time-reversal symmetry requires that the spin splitting at different valleys be opposite, which means the $\pm K$ valleys have different energies for a specific spin orientation. This phenomenon is called spin-valley locking and refers to the fact the spin and valley degrees of freedom are connected. Figure 7 shows a schematic drawing of the band structure at the band edges located at the $\pm K$ points resulting from the spin-orbit coupling effect.

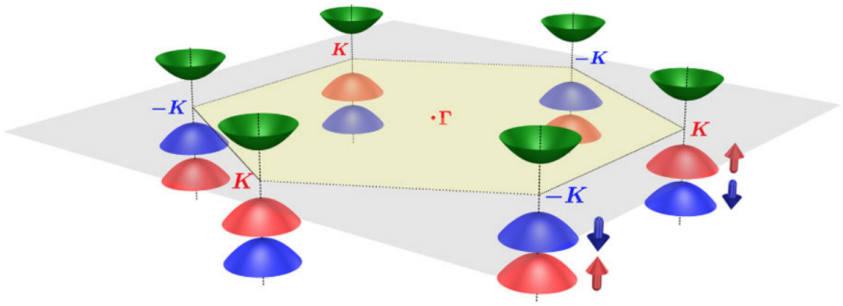

Figure 7 – Schematic drawing of the band structure at the band edges located at the K points.

Source: Adapted from WINKLER. (35)

2.3 Optical properties

The most important optical property of the TMD monolayers is the formation of excitons, which are bound electron-hole pairs. In a semiconductor, the absorption of a photon with suitable energy can promote an electron to the conduction band, leaving a hole in the valence band. When the attraction forces between the two particles are stronger than the thermal fluctuations of the surrounding environment, an excitonic bound state can form before decaying within a certain lifetime. In bulk crystals, the Coulomb interaction between electrons and holes is strongly screened, resulting in the low binding energy of excitons and their observation only at cryogenic temperatures. On the other hand, the dielectric screening in TMD monolayers is significantly reduced (37) because

the electric field lines joining the electron and hole begin to extend outside of the sample, as shown in Fig. 8a. This strong, attractive Coulomb interaction increases the binding energies, which can reach up to 0.5 eV in dielectric modulated environments (38, 39) and generate excitons even at room temperature. Also, it results in the exciton Bohr radius (analogous to the hydrogen atom) on the order of one to a few nanometers, with the correlation between the carriers extending several lattice periods (see Fig. 8b).

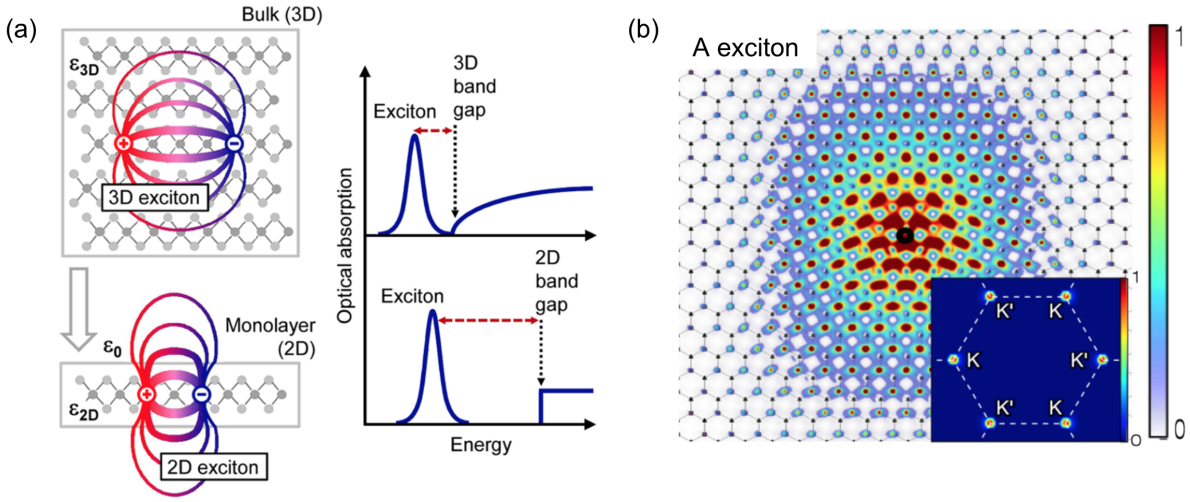

Figure 8 – (a) Change in the dielectric environment for the bulk-to-monolayer transition (left) and subsequent modification of the optical absorption spectra (right). (b) Exciton wavefunction in real space and momentum space (inset).

Source: (a) Adapted from CHERNIKOV. (37); (b) Adapted from QIU; FELIPE; LOUIE. (40)

The complex band structure of TMD monolayers (Fig 9a) gives rise to a spectrum of different types of excitons. They include "bright" excitons, which are optically active and can decay emitting a photon, and "dark" excitons, which cannot recombine radiatively. Dark excitons are generally formed when the recombination transition is spin-forbidden or momentum-forbidden. Such optical selection rules can happen by scattering events with other excitons, phonons, or electrons that induce spin flips or changes in exciton momentum. More specifically, due to the limited momentum carried by photons, radiative transitions for excitons are restricted to the "light cone" shown in Fig. 9b. Since dark excitons are optically inactive, they are usually absent from the photoluminescence (PL) spectrum, but they can be brightened with a magnetic field (41, 42) or using an in-plane detection scheme. (43)

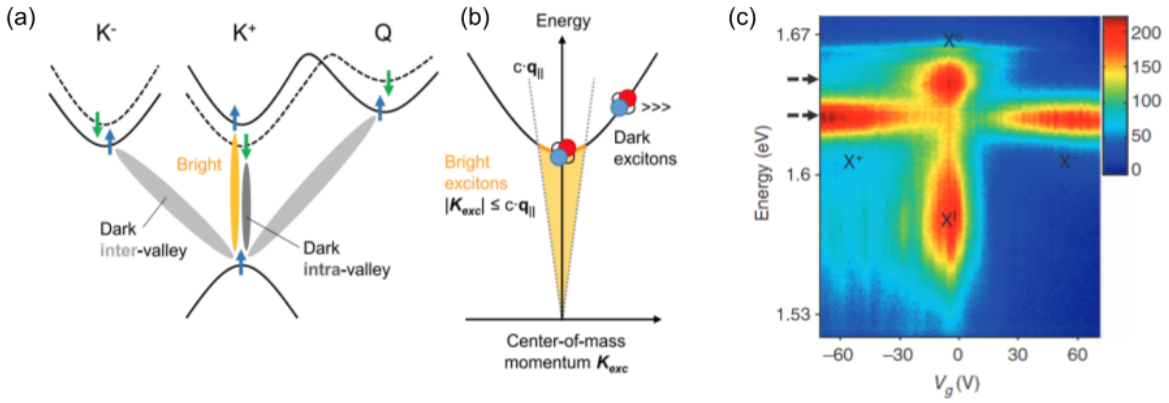

Figure 9 – (a) Bright and dark excitons and band structure of a tungsten-based TMD monolayer. The diagram is simplified for clarity, showing only the upper valence band at +K and the high-symmetry points ±K and Q in the conduction band. (b) Exciton light cone, where excitons inside the cone are bright, and those outside are essentially dark. (c) Gate-dependent PL spetra showing neutral (X^0), charged (X^+ and X^-) and trapped ($X^|$) exciton states in a monolayer $MoSe_2$ field-effect transistor.

Source: (a,b) Adapted from WANG *et al.* (44); (c) Adapted from ROSS *et al.* (45)

In addition to excitons, the strong Coulomb interaction generates many-body effects such as trions, biexcitons, and more complex species (46–50) (see Fig. 9c). Trions are charged excitons formed by two electrons and a hole, or vice versa. They have lower binding energies than excitons and can emerge when excess carriers are introduced to bind to electron-hole pairs. (46) They have been observed using gate-dependent PL measurements. (45) Biexcitons, on the other hand, are neutral four-body quasiparticles composed of two electrons and two holes and can be measured by power-dependent PL. (47–49) Finally, we mention that more complex excitonic species such as five-particle negatively charged biexciton (50) and localized excitons (51, 52), formed at defect sites or by external confinement have been observed, with the latter being a prominent candidate for single-photon devices.

2.4 Vibrational and mechanical properties

Another important feature of TMDs is their unique phonon dispersion, which has been studied using *ab initio* calculations and Raman spectroscopy. Figure 10a shows the main Raman modes for bulk MoS_2, which correspond to the in-plane mode E^1_{2g} and out-of-plane mode A_{1g}. Figure 10b,c shows the behavior of the Raman spectra as a function of the film thickness. Interestingly, as the film approaches the monolayer limit, the frequency difference tends to a specific value, which lies between 18-19 cm^{-1} for MoS_2 over SiO_2/Si

substrate. (53) Besides, the frequency difference for single MoS_2 layers is approximately 3 cm^{-1} smaller than for bilayers, showing that Raman spectroscopy constitutes a useful method for identifying layer thickness.

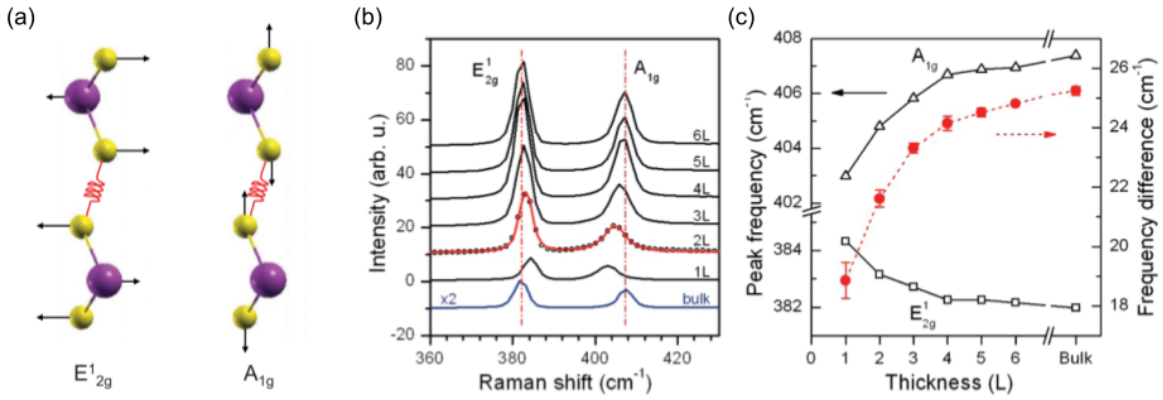

Figure 10 – (a) Schematic illustration of the in-plane phonon mode E^1_{2g} and out-of-plane phonon mode A_{1g}. (b) Raman spectra for mono- and multilayer MoS_2. (c) Peak frequency and frequency difference as a function of the layer thickness.

Source: (a) Adapted from MOLINA-SANCHEZ; WIRTZ. (53); (b,c) Adapted from LEE *et al.* (54)

Additionally, TMDs possess excellent mechanical properties that can be used as key components in flexible electronics. (55,56) For instance, using atomic force microscopy (AFM) nanoindentation to measure the mechanical properties of exfoliated MoS_2 monolayer, researchers have found Young's modulus and breaking strength of 270 ± 100 GPa and 15 ± 3 Nm^{-1}, respectively. (2) Although those values are lower than graphene, they are still greater than stainless steel.

3 PLASMONICS

Plasmonics is a subfield of optics and is concerned with the investigation of electron oscillations in metallic nanostructures known as plasmons and their interaction with light. One very interesting type of those coherent collective oscillations is surface plasmon polaritons (SPPs), which can control and manipulate light at the nanoscale. Here, we describe the essential features of SPPs systems pertinent to this work.

3.1 Classical electromagnetic formalism

3.1.1 Maxwell's equations

In order to describe any classical electromagnetic phenomena, such as the behavior of electric and magnetic fields and their interaction with matter, the macroscopic Maxwell's equations must be introduced. They are a set of coupled differential equations that describe how electromagnetic fields are generated by changes in each other and by the presence of charges and currents. They are given by:

$$\boldsymbol{\nabla} \cdot \mathbf{D} = \rho_f, \tag{3.1a}$$

$$\boldsymbol{\nabla} \cdot \mathbf{B} = 0, \tag{3.1b}$$

$$\boldsymbol{\nabla} \times \mathbf{E} = -\frac{\partial \mathbf{B}}{\partial t}, \tag{3.1c}$$

$$\boldsymbol{\nabla} \times \mathbf{H} = \mathbf{J}_f + \frac{\partial \mathbf{D}}{\partial t}, \tag{3.1d}$$

where $\mathbf{D}$ is the electric field displacement, $\mathbf{B}$ is the magnetic induction, $\mathbf{E}$ is the electric field, $\mathbf{H}$ is the magnetic field, ρ_f is the free charge density and $\mathbf{J}_f$ is the free current density. The definitions of the field $\mathbf{D}$ and $\mathbf{H}$ are, more explicitly:

$$\mathbf{D} = \varepsilon_0 \mathbf{E} + \mathbf{P}, \tag{3.2a}$$

$$\mathbf{H} = \frac{1}{\mu_0}\mathbf{B} - \mathbf{M}, \tag{3.2b}$$

where $\mathbf{P}$ is the polarization field, $\mathbf{M}$ is the magnetization field, ε_0 is the vacuum permittivity and μ_0 is the vacuum permeability. These fields are associated with the density of permanent or induced electric/magnetic dipole moments within a material and describe how this material responds to an applied electric/magnetic field.

For linear materials, the vectors $\mathbf{P}$ and $\mathbf{M}$ are given by:

$$\mathbf{P} = \varepsilon_0 \chi_e \mathbf{E}, \tag{3.3a}$$

$$\mathbf{M} = \chi_m \mathbf{H}, \tag{3.3b}$$

with χ_e and χ_m being the electric and magnetic susceptibility, respectively. Substituting equations (3.3) into equations (3.2) leads to:

$$\mathbf{D} = \varepsilon_0 \mathbf{E} + \mathbf{P} = \varepsilon_0 (1 + \chi_e)\mathbf{E} = \varepsilon_0 \varepsilon_r \mathbf{E} = \varepsilon \mathbf{E}, \tag{3.4a}$$

$$\mathbf{H} = \frac{1}{\mu_0}\mathbf{B} - \mathbf{M} = \frac{1}{\mu_0(1 + \chi_m)}\mathbf{B} = \frac{1}{\mu_0 \mu_r}\mathbf{B} = \frac{1}{\mu}\mathbf{B}, \tag{3.4b}$$

where ϵ and μ are the permittivity and permeability of the material, respectively.

However, the main challenge in characterizing any material is finding an appropriate model for ε and μ. For instance, in inhomogeneous media, the permittivity and permeability depend on the material's location; in anisotropic media, they become tensors. (57,58) Moreover, since real materials are generally dispersive, ε and μ depend on the frequency of the driving fields. (59) In plasmonics, nonetheless, the materials are usually linear, isotropic, and nonmagnetic ($\mu_r = 1$), so we will concern ourselves with only the permittivity, which may be frequency-dependent and is conventionally called the complex dielectric function:

$$\varepsilon(\omega) = \varepsilon_1(\omega) + i\varepsilon_2(\omega). \tag{3.5}$$

3.1.2 Dielectric function of a material

The dielectric function of any material is theoretically calculated by analyzing how the charge distribution inside the media responds to the local fields, which are influenced by the driving fields and the polarized matter. Those models can have varying degrees of approximation, from classical methods to many-body calculations based on quantum field theory. (60) Here, we will focus on two classical models that appropriately describe most situations: the Lorentz model used to describe the response of materials with bounded charge carriers, such as semiconductors and dielectrics, and the Drude model, which describes materials with free carriers, such as metals.

We begin our exploration by discussing the Lorentz model, in which we consider an electron with charge $-e$ and mass m_e bound to a positive and much heavier atomic nucleus. Restricting ourselves to the one-dimensional case for simplicity, we consider three forces present in this system. First, the bond between the charge carriers is represented by a "string" with spring constant k_r that follows Hook's law with a restoring force $\mathbf{F_r} = -k_r \mathbf{x}$, where $\mathbf{x}$ is the electron displacement. Second, we consider damping of the electron

motion by a viscous force $\mathbf{F}_d = -m_e\Gamma\dot{\mathbf{x}}$, with speed $\dot{\mathbf{x}}$ and damping frequency Γ. Finally, we let an external electric field drive this system by the electrostatic force $\mathbf{F_e} = -e\mathbf{E}$. More specifically, we assume a harmonically oscillating electric field $\mathbf{E} = \mathbf{E_0}\exp\{-i\omega t\}$. Newton's second law for this system is

$$m_\mathrm{e}\ddot{\mathbf{x}} = -m_\mathrm{e}\Gamma\dot{\mathbf{x}} - m_\mathrm{e}\omega_0^2\mathbf{x} - e\mathbf{E}, \tag{3.6}$$

where $\omega_0 = \sqrt{k_r/m_e}$.

Equation (3.6) represents a typical damped and driven harmonic oscillator, whose solution is

$$\mathbf{x} = \mathbf{x}_0\exp\{-i\omega t\}, \tag{3.7}$$

with

$$\mathbf{x}_0 = -\frac{e\mathbf{E}_0}{m_\mathrm{e}}\frac{1}{\omega_0^2 - \omega^2 - \mathrm{i}\Gamma\omega}. \tag{3.8}$$

The polarization field is defined as the net electric dipole moment per unit volume. If we call $\mathbf{p}$ the dipole moment of a single dipole and n_e the number of dipoles per unit volume, we can write $\mathbf{P}$ as

$$\mathbf{P} = n_e\mathbf{p} = -n_e e\mathbf{x} = -n_e e\mathbf{x_0}\exp\{-i\omega t\}. \tag{3.9}$$

Substituting Eq. (3.7), Eq. (3.8) and Eq. (3.9) into Eq. (3.4a) and isolating the dielectric function ε, we have

$$\varepsilon_{r,L}(\omega) = 1 + \frac{\omega_p^2}{\omega_0^2 - \omega^2 - \mathrm{i}\Gamma\omega} \equiv \varepsilon_1 + \mathrm{i}\varepsilon_2 \tag{3.10}$$

where $\omega_p^2 = (n_e e^2/\epsilon_0 m_e)$ is called the plasma frequency and represents the rapid oscillations of the electron density within the material.

Let us discuss some general points regarding the complex dielectric function derived above. Figure 11 shows the plots for the real and imaginary parts of $\varepsilon_{r,L}$. For the imaginary part, we can see a clear resonant behavior, with the peak position at ω_0 and full width at half maximum (FWHM) equal to Γ, which shows that the resonance broadening is directly related to the damping frequency. For the real part, there are two important aspects worth mentioning. First, we can see that $\varepsilon_1(\omega)$ is influenced by frequencies far from the resonance. This fact occurs because of the causality-imposed Kramers-Kronig relations (61), which describe that output cannot be determined by the instantaneous value of an input. In other words, it shows that attenuation and dispersion are not independent in real materials, leading to the contribution of all seemingly unimportant frequencies away from the resonance. Second, we note that $\varepsilon_1(\omega)$ can have negative values, which is essential to the field of plasmonics regarding the formation of polaritonic states (see Sec. 3.2). Finally, it is important to point out that for real materials, there is usually more than one type of polarization, such as electronic, ionic, or orientational polarization. (58) Therefore, a more accurate model should incorporate the contributions of various

polarizations across the frequency spectrum with appropriate frequency, damping, and strength.

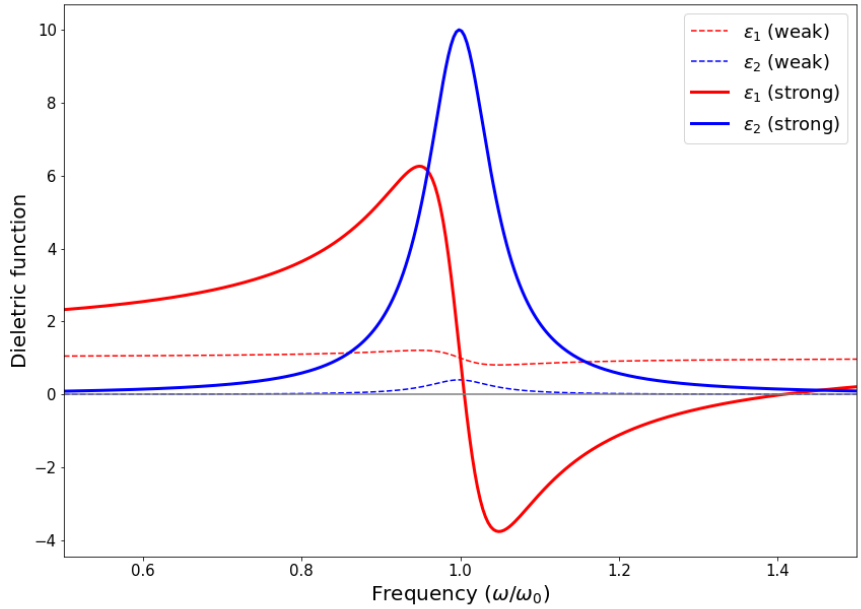

Figure 11 – Real and imaginary parts of dielectric functions calculated according to the Lorentz model. Parameters: $\hbar\omega_0 = 1$ eV, $\Gamma = \omega_0/10$, and $\hbar\omega_p = 0.2$ eV (weak, dashed lines) or $\hbar\omega_p = 1$ eV (strong, solid lines).

Source: By the author.

We will describe the Drude model, which applies to materials with unbounded electrons. To obtain the equation of motion for this model, one must omit the restoring force in equation (3.6):

$$m_e\ddot{\mathbf{x}} = -m_e\Gamma\dot{\mathbf{x}} - e\mathbf{E}. \tag{3.11}$$

Using the same procedure as the Lorentz model, we can derive the dielectric function associated with the Drude model:

$$\varepsilon_{r,D}(\omega) = 1 - \frac{\omega_p^2}{\omega^2 + \mathrm{i}\Gamma\omega} \equiv \varepsilon_1 + \mathrm{i}\varepsilon_2. \tag{3.12}$$

As we can see, the Drude model is a special case of the Lorentz model for $\omega_0 = 0$. For all frequencies from zero to ω_p, the real part of the dielectric function is negative. This is important because the plasma frequency is directly related to the response of metals to incident electromagnetic waves, which will be discussed in more detail in the next section. Here, we note that ω_p can be altered by changing the charge carrier density n_e, allowing for tunability of the optical properties of different materials.

3.1.3 Electromagnetic waves

For materials with no free charges ($\rho_f = 0$) or currents ($\mathbf{J}_f = 0$), Maxwell's equations (3.1) yield two wave equations:

$$\left(\nabla^2 - \varepsilon\mu\frac{\partial^2}{\partial t^2}\right)\left\{\begin{array}{c}\mathbf{E}(\mathbf{x},t)\\ \mathbf{H}(\mathbf{x},t)\end{array}\right\} = 0. \tag{3.13}$$

Assuming a time-harmonic behavior, one can show that the general solutions for the electric and magnetic fields in Eq. (3.13) are (57, 62)

$$\mathbf{E}(\mathbf{x},t) = \mathbf{E_0}\exp\{i\mathbf{k}\cdot\mathbf{x} - i\omega t\}, \tag{3.14a}$$

$$\mathbf{H}(\mathbf{x},t) = \mathbf{H_0}\exp\{i\mathbf{k}\cdot\mathbf{x} - i\omega t\}, \tag{3.14b}$$

where ω is angular frequency and $\mathbf{k} = k\hat{\mathbf{k}} = n\omega/c\hat{\mathbf{k}}$ is the wavevector, with k the wavenumber. The quantity $n \equiv \sqrt{\varepsilon_r\mu_r}$ is the index of refraction of the material, and c is the speed of light in free space.

For nonmagnetic media, we have $\mu_r = 1$, so the optical properties of the material are described by its dispersion relation (dependence with the frequency ω) and the dielectric function ε_r. Additionally, the the x, y, and z components of the wavevector k are related by the relation

$$k^2 = k_x^2 + k_y^2 + k_z^2 = \left(\frac{n\omega}{c}\right)^2 = \left(\frac{n2\pi}{\lambda}\right)^2, \tag{3.15}$$

where we used $\omega/c = 2\pi/\lambda$, with λ the wavelength of the wave. Note that (3.15) demonstrates k_x, k_y, and k_z cannot be increased indiscriminately, showing that dielectric materials have a fundamental resolution limit of $\lambda/2n$, which is called Rayleigh's resolution limit.

To overcome this limitation, one of the components of the wavevector k must be imaginary. For instance, if k_z is imaginary, we have $k_z^2 < 0$, leading to

$$k_x^2 + k_y^2 - |k_z|^2 = n^2(\omega/c)^2. \tag{3.16}$$

It is clear now that k_x and k_y can be increased arbitrarily, allowing for greater confinement than dielectric media. Physically, one way to achieve this is by using plasmonic materials. To understand this fact, it is important to discuss the concept of plasmons. A plasmon is a collective oscillation of the free electrons in a given material. The electron motion can be described by the dielectric function derived from the Drude model. To simplify our discussion, we will consider the case with no losses ($\omega \gg \Gamma$), so Eq. (3.12) becomes

$$\epsilon_r(\omega) \approx 1 - \frac{\omega_p^2}{\omega^2}, \tag{3.17}$$

with three regions of interest: $\omega > \omega_p$, $\omega = \omega_p$, and $\omega < \omega_p$.

For $\omega > \omega_p$, the dielectric function is positive. This results in a real value for the wavenumber k and allows for propagating electromagnetic waves within the media. When $\omega = \omega_p$, we have $\varepsilon_r = 0$ and $k = 0$. This situation describes the volume plasmon, an oscillation with a constant phase across the material. Finally, for $\omega < \omega_p$, the dielectric function becomes negative, allowing k to be a complex number. In this condition, the electromagnetic wave becomes an evanescent field i.e. that decays exponentially. Moreover, since k is a complex number, some components can increase arbitrarily, allowing for resolutions below Rayleigh's resolution limit.

3.2 Surface plasmon polaritons

Surface plasmon polaritons (SPPs) are oscillations of free electrons coupled to a light wave at the boundary between metals and dielectrics. The term *polariton* describes the coupling between the collective excitations in solids, such as free electrons (plasmons), lattice vibrations (phonons), or spins of electrons (magnons), with light. (63–65) To understand the physics of SPPs, we must define the geometry of the system. For simplification, we consider two homogeneous semi-infinite media with the interface at $z = 0$ plane, where for $z > 0$ we have a dielectric with a dielectric function $\varepsilon_{r,d}$ and for $z < 0$ we have a metal with the dielectric function $\varepsilon_{r,m}$ (see Fig. 12a). Assuming harmonic solutions of electromagnetic waves propagating in the x direction with evanescent decay in the perpendicular z-direction, as discussed in the previous section, one has

$$\begin{pmatrix} \mathbf{E}(\mathbf{x},t) \\ \mathbf{H}(\mathbf{x},t) \end{pmatrix} \equiv \begin{Bmatrix} \mathbf{E}(z) \\ \mathbf{H}(z) \end{Bmatrix} \exp(-\mathrm{i}(\omega t - \beta x)), \tag{3.18}$$

where β is the wavevector in the direction of propagation, we can rewrite Eq. (3.13) as

$$\left(\frac{\mathrm{d}^2}{\mathrm{d}z^2} + \left(k_0^2 \varepsilon_\mathrm{r} - \beta^2 \right) \right) \begin{Bmatrix} \mathbf{E}(z) \\ \mathbf{H}(z) \end{Bmatrix} = 0, \tag{3.19}$$

with $k_0 = \sqrt{\varepsilon_0 \mu_0}\omega$.

Now, inserting the proposed solutions in Eq. (3.18) into Maxwell's equations, we find that only a transverse magnetic mode (TM) with components (E_x, E_z, H_y) and a transverse electric mode (TE) with components (E_y, H_x, H_z) can exist. (59) Additionally, applying the boundary conditions to the two modes shows that only the TM mode is capable of generating surface waves at the interface, with the respective field amplitudes given by (66)

$$E_{x,\ \mathrm{d/m}}(z) = \pm \mathrm{i} \frac{k_{\mathrm{d/m}}}{\omega \varepsilon_0 \varepsilon_{\mathrm{r,d/m}}} \exp(\mathrm{i}\beta x) \exp\left(\mp k_{\mathrm{d/m}} z \right), \tag{3.20a}$$

$$E_{z,\ \mathrm{d/m}}(z) = -\frac{\beta}{\omega \varepsilon_0 \varepsilon_{\mathrm{r,d/m}}} \exp(\mathrm{i}\beta x) \exp\left(\mp k_{\mathrm{d/m}} z \right), \tag{3.20b}$$

$$H_{y,\ \mathrm{d/m}}(z) = \exp(\mathrm{i}\beta x)\exp\left(\mp k_{\mathrm{d/m}} z\right), \tag{3.20c}$$

where k_d and k_m are the wavevectors, perpendicular to interface (z-direction), in the dielectric material and metal, respectively. Finally, using the continuity conditions (that the tangential components of **E** and **H** are continuous at $z = 0$), one can show that (66)

$$\frac{k_{\mathrm{d}}}{k_{\mathrm{m}}} = -\frac{\varepsilon_{\mathrm{r,d}}}{\varepsilon_{\mathrm{r,m}}}, \tag{3.21a}$$

$$k_{\mathrm{d/m}}^2 = \beta^2 - k_0^2 \varepsilon_{\mathrm{r,d/m}}. \tag{3.21b}$$

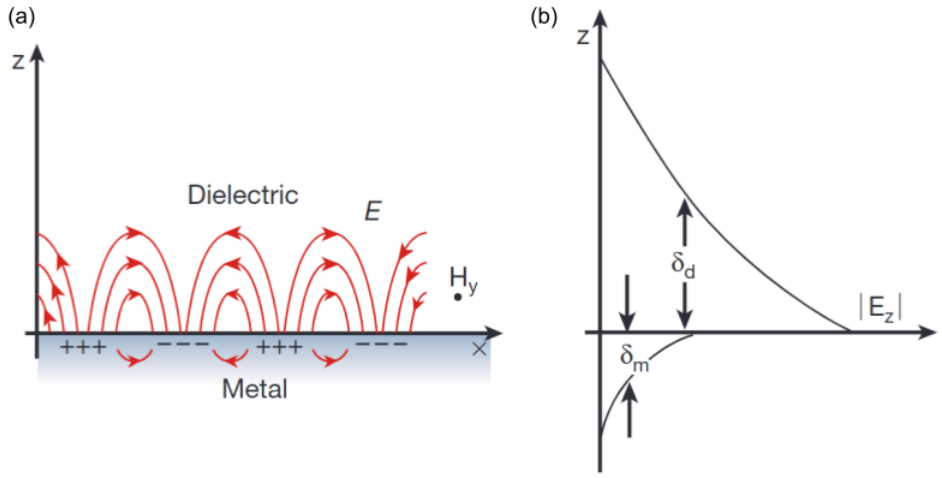

Figure 12 – (a) Illustration of the evanescent electromagnetic field and surface charges at the interface between a dielectric material and a metal. (b) z-component of the electric field as a function of the distance perpendicular to the surface.

Source: (a,b) Adapted from BARNES; DEREUX; EBBESEN. (67)

Since we are searching for solutions with an evanescent decay, we conclude from Eq. (3.20) that the real part of the wavevectors $k_{d,m}$ are positive. To fulfill this condition, according to Eq. (3.21a), we must have $\varepsilon_{r,d}$ and $\varepsilon_{r,m}$ with opposite signs. Generally, dielectrics have a positive real part of the dielectric function, resulting in the need for materials with a negative real part of the dielectric function. Metals are such materials that naturally possess this property, with noble metals having high plasma frequencies that allow SPP generation at optical frequencies. (68) However, as we have shown in Fig. 11, even materials with bound electrons can have negative permittivities, such as highly doped semiconductors. (69) Moreover, the penetration depths shown in Fig. 12b are given by $\delta_{\mathrm{d/m}} = 1/\left|k_{\mathrm{d/m}}\right|$ and characterizes the SPPs confinement with regard to the interface.

Following our discussion, if we combine Eqs. (3.21a) and (3.21b) we arrive at the dispersion relation of SPPs

$$\beta(\omega) = k_0(\omega)\sqrt{\frac{\varepsilon_{\mathrm{r,d}}(\omega)\varepsilon_{\mathrm{r,m}}(\omega)}{\varepsilon_{\mathrm{r,d}}(\omega) + \varepsilon_{\mathrm{r,m}}(\omega)}}. \tag{3.22}$$

Figure 13 shows the plot for (3.22), considering $\varepsilon_{r,d} = 1$, $\varepsilon_{r,m} = 1 - \omega_p^2/\omega^2$, and $\Gamma = 0$, as well as the light dispersion in free space. It is clear that for small β, the dispersion of SPPs lies very close to the light line, showing that the polariton state is "light-like". As β increases, the SPP dispersion exhibits a nonlinear characteristic and approaches the limit $\omega_{\mathrm{SPP}} = \omega_p/\sqrt{1+\varepsilon_{r,d}}$. Moreover, we can see that SPPs have a greater in-plane wavevector than free-space light. Because momentum must be conserved, this condition implies that the excitation of SPPs by free-space light is impossible. One solution to overcome the momentum mismatch is using a prism coupling mechanism to enhance the momentum of incident light (70). Another solution is to rely on diffraction and scattering effects, where using gratings or some other types of surface corrugations, one can match the necessary momentum to achieve the coupling between SPP and light. (71)

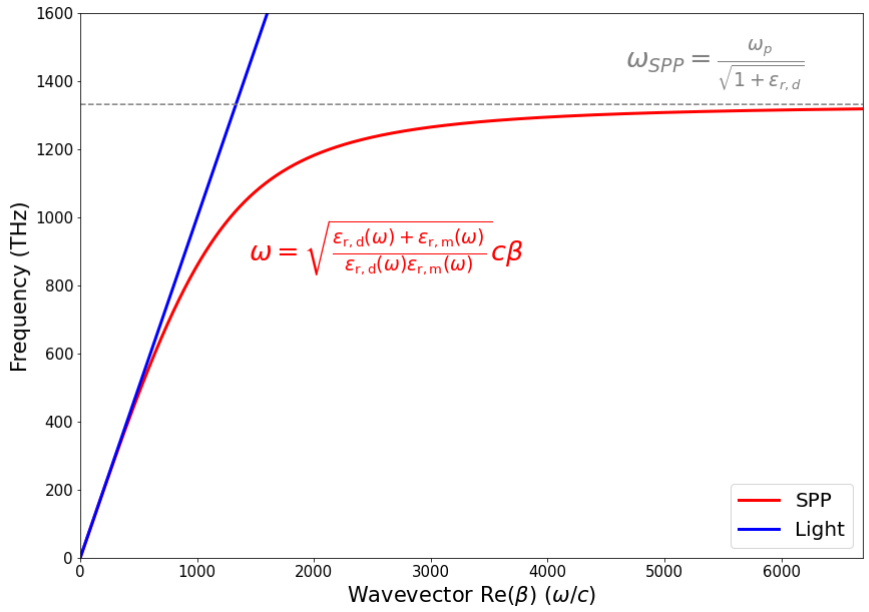

Figure 13 – Dispersion relation of SPPs and light in free space. The parameters for this simulation were: $\omega_p \approx 12$ x 10^{15} rad/s, $\Gamma = 0$, $\varepsilon_{r,d} = 1$, $\varepsilon_{r,m} = 1 - \omega_p^2/\omega^2$, and $c = 1$.

Source: By the author.

3.3 Localized surface plasmons

Besides SPPs, another fundamental plasmonic excitation is worth mentioning: localized surface plasmons (LSPs). LSPs are non-propagating collective oscillations of electron plasma that arise when the interface is spatially restricted in the lateral direction, as

in the case of metallic nanostructures. To understand how these excitations can influence the optical properties of the whole system, we consider a simple geometry of a metallic nanoparticle: a spherical metallic particle with the dielectric function ε_m, with radius R, surrounded by a dielectric material with the dielectric function ε_d and illuminated by an electromagnetic plane wave with wavelength λ. Usually, these particles are much shorter than the wavelength of light ($R \ll \lambda$), so the phase of the electromagnetic wave is practically constant over the entire particle. Therefore, to calculate the fields inside and outside of the particle, we can use the quasi-static approximation, i.e., retardation effects are negligible. Figure 14 shows a schematic illustration of the problem.

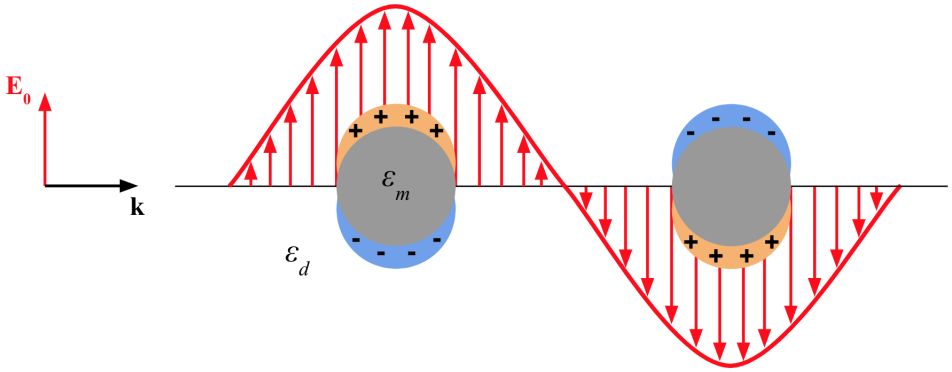

Figure 14 – Schematic illustration of two metallic nanoparticles being illuminated by an electromagnetic wave with wavevector **k** and electric field $\mathbf{E_0}$.

Source: By the author.

Note that the electric field $\mathbf{E_0}$ induces a polarization of the free electrons, and since we are considering motionless ionic cores, a restoring force is created. Solving Maxwell's equations for this particular case, we can calculate the induced dipole moment inside the particle as (59):

$$\mathbf{p} = \varepsilon_0 \varepsilon_\mathrm{d} 4\pi R^3 \frac{\varepsilon_m(\omega) - \varepsilon_\mathrm{d}}{\varepsilon_m(\omega) + 2\varepsilon_\mathrm{d}} \mathbf{E_0} = \varepsilon_0 \varepsilon_\mathrm{d} \alpha \mathbf{E_0}, \tag{3.23}$$

where $\alpha = 4\pi R^3(\varepsilon_m - \varepsilon_d)/(\varepsilon_m + 2\varepsilon_d)$ is called the polarizability. It is important to point out that we are using the description based on a single dipole moment instead of the dipole moment density because we are describing a single isolated particle. Nevertheless, it is possible to see that the resonant condition for α occurs when $\varepsilon_m + 2\varepsilon_d = 0$. Since the real part of ε_d is generally positive, we conclude that $\mathrm{Re}(\varepsilon_m)$ must be negative and thus arrive at the same conclusion as for the SPP case: the particle has to be metallic. Additionally, solving Maxwell's equations allows one to obtain the electric field inside and outside of the sphere (59):

$$\mathbf{E_{in}} = \frac{3\varepsilon_d}{\varepsilon_m(\omega) + 2\varepsilon_d} \mathbf{E_0}, \tag{3.24a}$$

$$\mathbf{E_{out}} = \mathbf{E_0} + \frac{3\hat{\mathbf{r}}(\hat{\mathbf{r}} \cdot \mathbf{p}) - \mathbf{p}}{4\pi\varepsilon_0\varepsilon_d} \frac{1}{r^3}, \tag{3.24b}$$

where $\hat{\mathbf{r}}$ is the unit vector and r is the distance in the direction towards the point of interest.

The ratio $|\mathbf{E_{in/out}}|/|\mathbf{E_0}|$ determines the electric field enhancement at the vicinity of the nanoparticle. Figure 15a shows this electric enhancement for the case of a silver nanosphere using numerical calculations. One can see a small deviation from the symmetric dipole fields predicted by Eq. (3.24b) for the scattered electric field outside of the particle. It is caused by non-negligible retardation effects that are not captured by the simple quasi-static approximation. For more complex geometries, an analytical treatment is impracticable and one must fully resort to numerical methods, such as discrete dipole approximation (DDA), finite-difference time-domain (FDTD), or finite element methods (FEM). Figure 15b shows a complex geometry of two coupled hybrid multilayer core-shell spheres, which can achieve a field enhancement of more than 2 orders of magnitude greater than a single solid silver nanosphere.

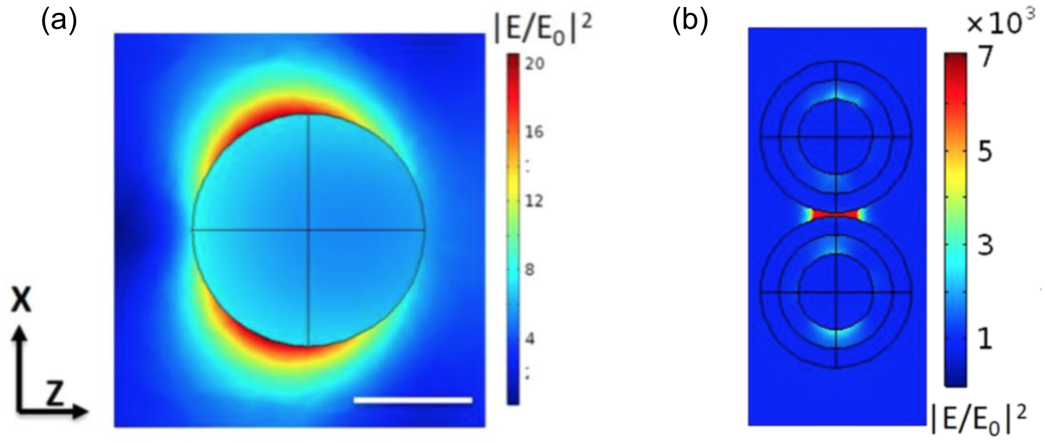

Figure 15 – (a), (b) Electric field distribution plotted for a solid metallic particle (a) and for two coupled hybrid multilayer core-shell spheres (b).

Source: Adapted from PARIA; ZHANG; BARMAN. (72)

4 METHODOLOGY

In this chapter, we present an overview of the methods used to fabricate and characterize a hybrid device composed of a MoS_2 monolayer coupled to gold gratings. First, we illustrate the microfabrication steps required to produce the plasmonic nanostructures, the atomic-thin film of MoS_2, and the transfer procedure of the monolayer to the gold gratings. Then, the second part will describe the structural and optical measurement techniques used in this dissertation. Finally, we conclude with a brief description of the procedure used for the numerical simulations.

4.1 Device fabrication

4.1.1 Gold structures

The growth of the gold gratings and monolayer MoS_2 was made at the École Polytechnique Fédérale de Lausanne (EPFL) in Switzerland by our collaborators G. Marega and A. Kis. As we discussed in chapter 3, metals are good candidates for plasmonic devices since they exhibit a negative real permittivity at optical frequencies. More specifically, conventional metals such as gold and silver are commonly used in plasmonics since they possess small ohmic losses and high direct current (DC) conductivity, although novel materials with smaller interband losses and adjustable dielectric permittivity have been studied recently. (73) Additionally, silver is well known to degrade in air, so gold was the material used in this dissertation for the plasmonic devices.

The first step in fabricating gold plasmonic structures is the production of thin, high-quality metal films. The electron-beam (e-beam) evaporation technique was used to accomplish this task since it allows the deposition of high-quality films with good adhesion and fast deposition rates. Figure 16 shows the system used for this technique. Overall, the procedure for e-beam evaporation is the following:

- Preparation of the substrate and metal source: the substrate is generally made of silicon or glass and properly cleaned to avoid impurity contamination. The metal is placed on a crucible made of a material with a high melting point, such as graphite ($\sim$ 3650 °C) or tungsten ($\sim$ 3400 °C);
- Creating a vacuum: thermal evaporation needs to be carried out at high vacuum, typically 10^{-6} Pa, to remove gases or impurities that might interfere in the process;
- Heating the metal source and monitoring deposition: the metal is heated using an electron beam, in which high-energy electrons transfer their kinetic energy to the metal, causing rapid heating and evaporation. The electron beam is created using an

electron source, an accelerating electrode, and a focusing system. A quartz crystal microbalance is placed in the vacuum chamber to monitor the film thickness, so the source material is deposited onto the sensor at the same rate as onto the substrate. This crystal vibrates and its vibration frequency changes as the film is deposited, allowing for monitoring the film thickness in real time;

- Cooling down the system: once the desired film thickness is reached, the electric current is turned off and the vacuum chamber is allowed to cool down. The thin metal film is then ready for further processing.

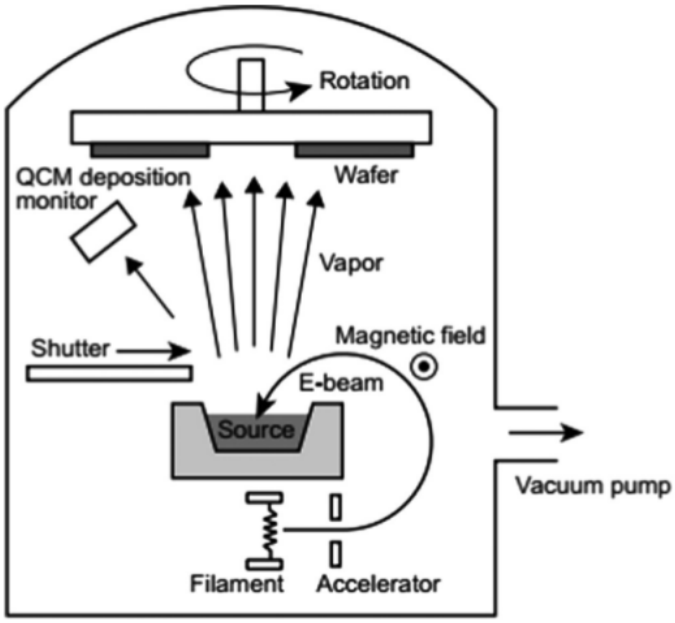

Figure 16 – Schematic diagram for the e-beam evaporation system.

Source: Adapted from ZHANG; HOSHINO. (74).

After the thermal evaporation step is completed, the film is subjected to a lithography phase to fabricate square metallic gratings. In this work, electron-beam lithography combined with ion-beam-assisted etching was used. A simple schematic diagram can be seen in Figure 17. First, the polymethyl methacrylate (PMMA) resist is spin-coated onto the Au film. Then, the resist-coated sample is loaded into an electron beam lithography system, where the exposed regions of the resist undergo a chemical change, making them more soluble. After exposure, an appropriate developer solution removes the soluble regions, creating the patterned resist layer. The patterned resist serves as a mask for ion-beam etching, allowing for the removal of the gold material and forming the desired structure. Finally, the leftover PMMA from the sample is removed using deionized water, acetone, and isopropanol, resulting in the desired patterned structure. In this dissertation,

we studied two gratings with different geometric parameters. Both gratings have a nominal slit depth of 50 nm, but different slit widths. More specifically, the nominal values for the widths were 100 nm and 50 nm. Also, their periodicity (distance between adjacent slits) is 1000 nm.

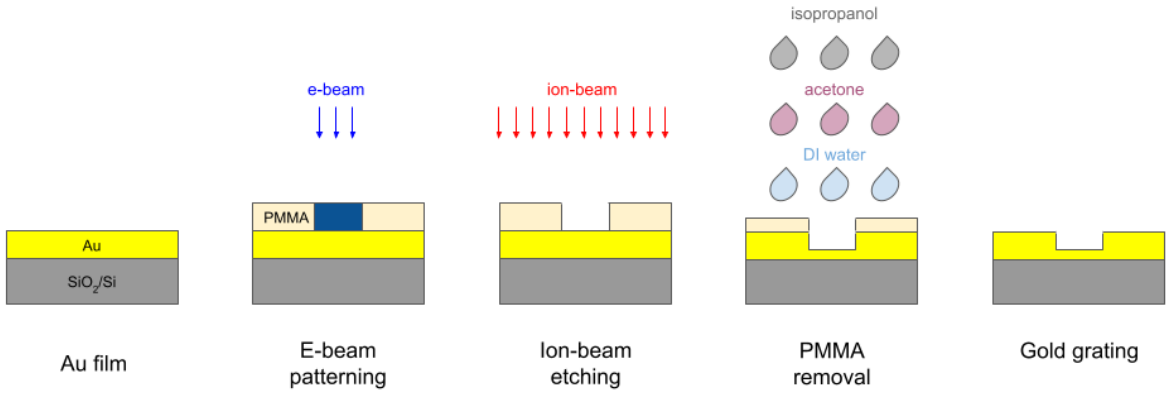

Figure 17 – Schematic illustration of electron beam lithography combined with ion-beam assisted etching.

Source: By the author.

4.1.2 Two-dimensional material

Currently, there are various methods of producing atomically thin materials, which can be divided into two groups: the "top-down" method of exfoliation from bulk crystals and the "bottom-up" method from precursor materials. The top-down method was used in the initial research stage of 2D TMDs, which relied on the mechanical exfoliation of bulk crystals. This technique is still used because it is simple and yields high-quality thin layers. However, it suffers from significant shortcomings preventing its use in industrial applications, such as unpredictable flake thickness, domain sizes, and slow manufacturing time. (75) For these reasons, the bottom-up approach was developed, offering the possibility of large-area growth of TMD films with high uniformity, scalability, and integration with other optical and mechanical systems. (76–78) The basic idea is to use heated gaseous or solid precursors and deliver them to a reaction chamber where they can combine to produce monolayers. The most common method is chemical vapor deposition (CVD), which involves using inorganic precursors with low vapor pressure, such as MoO_3 and sulfur. While this approach has been successful, it allows limited control over the deposition rate and nucleation density since the low vapor-pressure precursors must be loaded inside a heated zone of the reactor chamber. (79) To overcome this issue, the metal-organic CVD (MOCVD) method was developed, allowing greater flexibility and control over evaporation and mass flow rates. (80)

Here, we will provide a simple overview of the process, but the curious reader is

encouraged to see Ref. (79–81) for more details. Figure 18a shows a schematic illustration of a typical large-area MoS_2 film growth by MOCVD. Before growth, c-plane sapphire substrate wafers are annealed at $\sim$ 1000 °C in the air and treated with potassium hydroxide (KOH). Then, an aqueous solution of sodium molybdate (Na_2MoO_4) is spin-coated onto the substrate, which provides the molybdenum (Mo) precursor and alkali metal promoter (Na) for the monolayer growth, and placed in the growth chamber. Finally, the sulfur (S) precursor is delivered to the quartz tube by liquid $(C_2H_5)_2S$ with argon and hydrogen as the carrier gases. The reaction mechanism occurs at a growth temperature of 850 °C for $\sim$ 20 min, allowing the formation of a large-area continuous film. Figure 18b shows photos of the wafers before and after MoS_2 deposition. Figure 18c shows the proposed mechanism by the researchers for the monolayer growth.

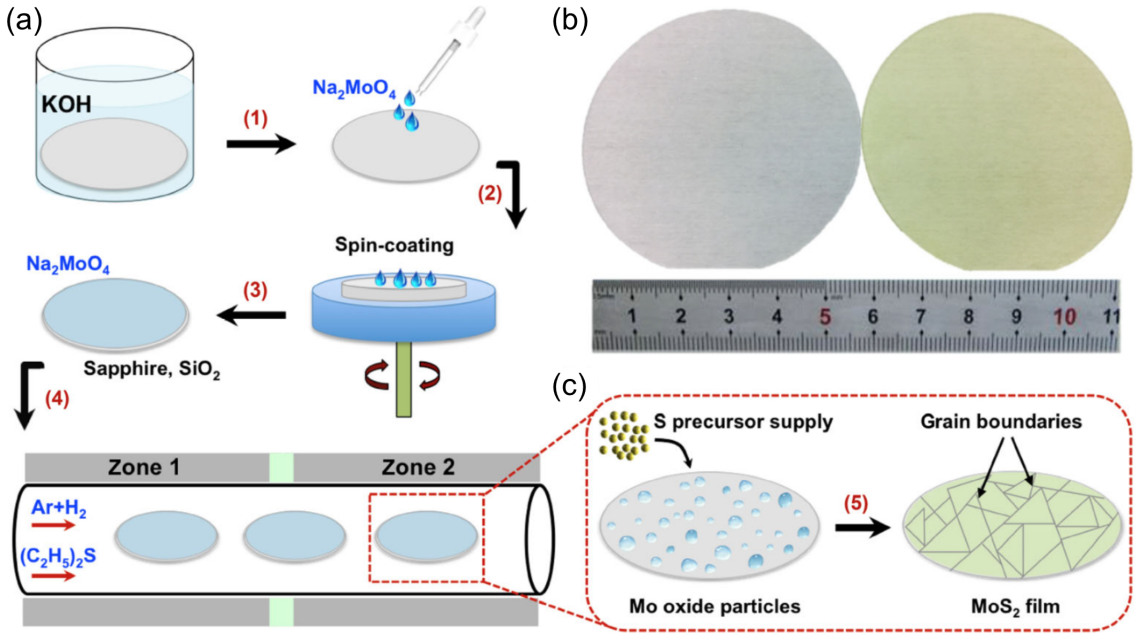

Figure 18 – (a) Illustration of the MoS_2 growth process by MOCVD. (b) Photos of the wafers before (left) and after (right) the MoS_2 deposition. (c) Proposed growth mechanism.

Source: Adapted from CUN *et al.* (79)

4.1.3 Transfer procedure

The MOCVD-grown material is transferred to the gold gratings by delamination, using a thermal release tape (TRT) and PMMA as a support layer. Initially, the PMMA is spin-coated onto the wafer containing the MoS_2 monolayer and heated at 180 °C. Next, a TRT with the same size as the grown material is attached to the MoS_2 sample. It is important to note that using a TRT provides a strategy to delaminate TMD layers without using etchants or solvents that render the substrate unusable for another growth

process. Then, the PMMA/MoS_2 /sapphire sample is placed in deionized water, which can penetrate between the TMD layer and sapphire substrate by scratching the corners of the film. Finally, the PMMA/MoS_2 system is lifted off, transferred manually to the target substrate, and put in a hot plate at 135 °C for removing the thermal release tape. The procedure is illustrated in Fig. 19a. Figure 19b shows a photo of the final system, while Fig. 19c depicts a schematic illustration of the hybrid device based on the plasmonic structures and the MoS_2.

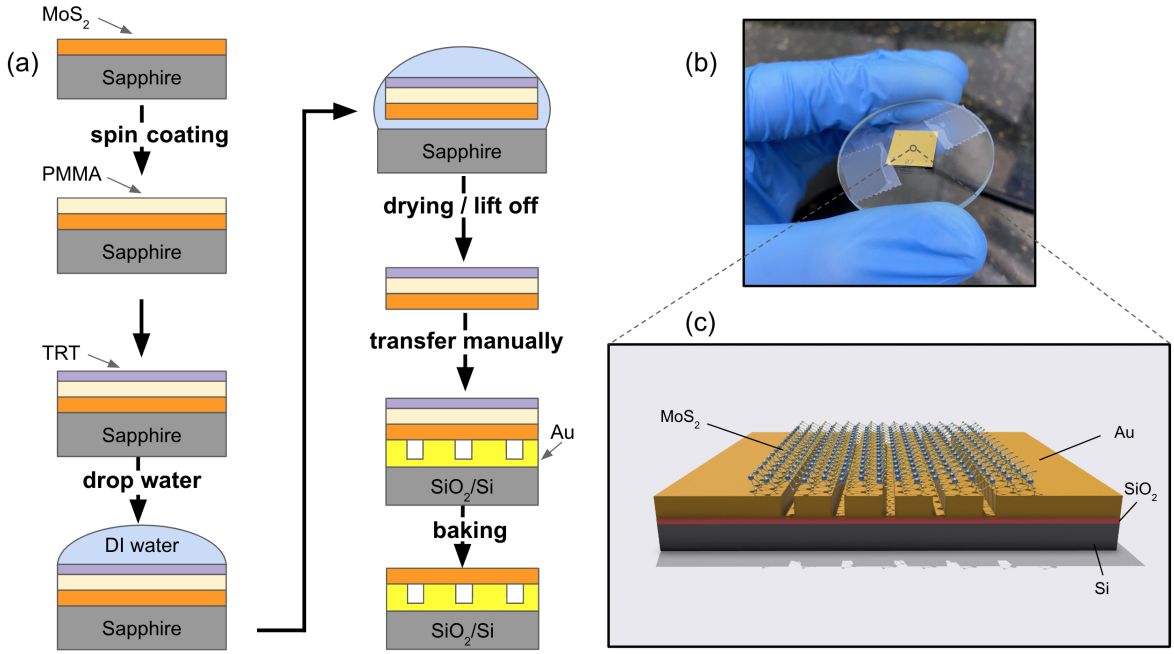

Figure 19 – (a) Procedure for PMMA-assisted transfer of MoS_2 on a sapphire substrate. (b) Photo of the final sample. (c) Schematic illustration of the MoS_2-gold hybrid device.

Source: By the author.

4.2 Characterization techniques

4.2.1 Atomic force microscopy

Atomic force microscopy (AFM) is a type of scanning probe microscopy that involves the interaction between a very sharp tip (radius of a few to tens of nanometres) and the sample surface. Scanning the surface with the tip and monitoring its deflection allows the operator to achieve high-resolution topographic images and more advanced physical properties maps such as modulus, adhesion, conductivity, etc. Moreover, AFM is suitable for ambient conditions and controlled environments with one single piece of equipment, making it a flexible platform for studying 2D materials. The core of an AFM instrumentation consists of a spring-like cantilever with a sharp tip at the free end, a piezoelectric actuator that is used to drive the tip or sample, an optical setup for measuring the interaction between the tip and the sample, and a fast feedback control loop

(see Fig. 20a). The optical setup is composed of a laser beam that impinges on the cantilever head and a position-sensitive photodetector. Monitoring the reflected beam allows accurate measurement of the motion of the tip and, as a consequence, a precise 2D or 3D image reconstruction of the sample surface.

The interaction forces may be attractive or repulsive depending on the distance between the tip and the sample. A simple but effective model to describe this effect is the Lennard-Jones potential. (82) For long distances ($d \geq 1$ μm), there is no interaction. As the tip approaches the sample ($d \leq 50$ nm), van der Waals forces emerge, resulting in attractive forces between the atoms of the tip and the sample. Those forces increase with decreasing distance until the separation is short enough ($d \sim 0.5$ nm), where the Pauli exclusion principle dominates, and the interaction becomes repulsive. Figure 20b show the Lennard-Jones potential as a function of the separation distance. Moreover, it shows the regions of the three AFM operating regimes: contact mode, non-contact mode, and tapping mode.

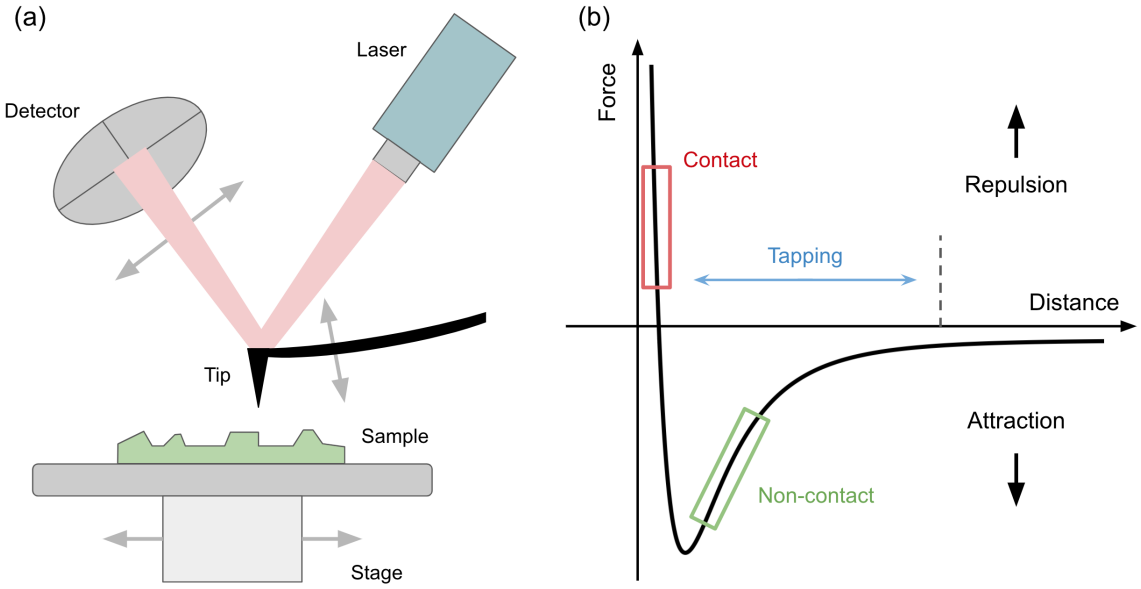

Figure 20 – (a) Principle of operation of an AFM. (b) Lennard-Jones potential as a function of the separation distance shows the attractive and repulsive regimes and the corresponding AFM operating modes.

Source: By the author.

Initially, AFM was used in contact mode, where the tip continually interacts with the sample surface. While this enabled the formation of high-resolution images and advanced electric measurements, it also resulted in tip wearing and sample damage, making it detrimental to various applications. To solve this problem, an intermittent contact mode called tapping mode was created, where the cantilever oscillates near its resonance frequency. When the tip is close to the surface, the forces acting on the cantilever cause its

oscillation amplitude to vary. The feedback control loop sends a corrective voltage signal to the piezoelectric actuator that maintains a constant cantilever amplitude, calibrated to height information and subsequent topographic images. Moreover, a phase image that monitors the phase lag between the signal that drives the cantilever oscillation and its output signal can be obtained, where variations in the phase lag show the variations in the mechanical properties of the sample surface. All AFM data in this dissertation were acquired using Bruker's Dimension Icon AFM in the IFSC laboratory. The intermittent tapping mode and Si tip of approximately 7 nm were used to extract the morphological information about the samples.

4.2.2 Photoluminescence spectroscopy

When light interacts with the medium, different optical processes can occur. They can be those where the frequency of the incident electromagnetic wave is unchanged by its interaction with the sample, such as reflection and Rayleigh scattering, or processes in which the frequency is altered by the sample, including photoluminescence (PL) and Raman scattering (see next section). PL is a powerful technique for characterizing the optical response of a wide variety of materials and was the first technique used to observe the indirect-to-direct bandgap transition in monolayer MoS_2 as discussed in chapter 2. The process consists of the absorption of a photon by the material and the emission of a photon with lower energy by the process known as spontaneous emission. It is important to point out that the spontaneous emission cannot be explained by the classical electromagnetic theory and a fully quantum mechanical treatment of the electromagnetic radiation is required for a precise description (the interested reader is referred to Ref. (83) for more details).

To gain a better understanding of the theoretical background of absorption and spontaneous emission, we can use the instructive case of a two-level atom interacting with a radiation field, which is given by the Hamiltonian

$$H = H_{atom} + H_{rad} + H_{int}, \tag{4.1}$$

where H_{atom}, H_{rad} and H_{int} are the Hamiltonians for the two-level atom, the radiation, and the interaction, respectively. Note that this formulation is inadequate for real solids with energy bands and excitonic effects, but it is nonetheless useful for an intuitive physical approach. One can study this case in the picture of second quantization, where the solution of the Hamiltonian describes the polariton concept. Alternatively, one can use perturbation theory and treat the radiation field as a small perturbation to the eigenstates ϕ and the eigenenergies E_n of the two-level system. (84) Here, we use the latter case. Moreover, employing a semiclassical treatment for the electromagnetic radiation and keeping only the first-order perturbation term, the total Hamiltonian is given by (84)

$$H = H_{atom} - \frac{e}{m}\mathbf{A}\frac{\hbar}{i}\Delta = H_{atom} + H^{(1)}, \tag{4.2}$$

where e is the electric charge, m is the mass of the atom, $\hbar$ is the reduced Planck's constant, i is the imaginary number and $\mathbf{A}$ is the vector potential. Using the time-dependent Schrödinger equation

$$H\psi = i\hbar\frac{\partial\psi}{\partial t}, \tag{4.3}$$

the solutions to the problem are

$$\psi(\boldsymbol{r},t) = \sum_{\mathrm{n}} a_{\mathrm{n}}(t)\varphi_{\mathrm{n}}(\boldsymbol{r})\mathrm{e}^{-\mathrm{i}(E_{\mathrm{n}}/\hbar)t}. \tag{4.4}$$

For $t > 0$, the transition rate w_{ij} from an initial state i to another state j is given by Fermi's golden rule (84, 85)

$$w_{ij} = \frac{2\pi}{\hbar}|H_{ij}^{(1)}|^2\rho(E), \tag{4.5}$$

where $\rho(E)$ is the density of final states and $H_{ij}^{(1)}$ is the transition matrix element given by

$$H_{ij}^{(1)} = \int \psi_j^*(\boldsymbol{r})H^{(1)}\psi_i(\boldsymbol{r})d\tau. \tag{4.6}$$

What is important from Eq. (4.5) is that the transition between two states is essentially given by the transition probability $|H_{ij}^{(1)}|^2$. In the case of absorption, this term is related to the incident electromagnetic field, and in the case of spontaneous emission, it is associated with the perturbation caused by the zero-point amplitude. (85) The optical intensity is proportional to the transition rate given by (4.5) multiplied by the probability that the initial state is occupied and the final state is empty (86)

$$I_{PL} \propto w_{ij}f_c(1-f_v), \tag{4.7}$$

where f_c and f_v are the Fermi-Dirac distributions in the conduction and valence bands, respectively.

From a practical standpoint, a typical PL experiment in solids can be described as follows. First, the sample is excited by a laser with an energy higher than the material's bandgap. Following the photon absorption, electrons are promoted to the conduction band, leaving a hole in the valence band. Then, both particles undergo energy and momentum relaxation in the form of Coulomb and phonon scattering towards the band extremes. Finally, the electron-hole pair can recombine radiatively, emitting a photon with an energy equal to the bandgap. A schematic illustration of the general principle of PL emission can be seen in Fig. 21. In this work, the measurements were made using a conventional PL setup located at the Federal University of São Carlos (UFSCar) in collaboration with Prof. Marcio Daldin. A schematic representation is shown in Fig. 22a. The excitation source was a laser centered at 532 nm, transmitted to the optical setup via a single-mode optical fiber. An aspheric lens with a 5 mm diameter, a focal distance of 1.6 mm, and a numerical aperture (NA) of 0.64 is used to focus the laser onto the sample and to collect the emitted signal (spatial resolution is 700 nm). The sample is placed in a

piezoelectric stage that controls the x, y, and z direction with a 10 nm spatial resolution. A multi-mode optical fiber sends the PL signal to a 150 lines/mm diffraction grating and then to a charge-coupled device (CCD) photon detector. The spectra are acquired using homemade software with an integration time of 10 s and 3 accumulations. All measurements were made at ambient conditions with a laser power of approximately 3.9 mW. We should also note that the incident radiation is not linearly polarized, but the larger component is in the x-direction (see Fig. 22b)

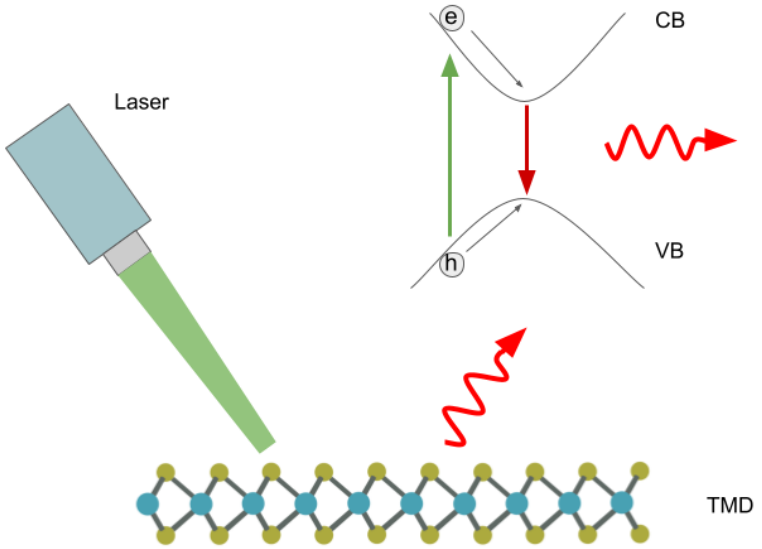

Figure 21 – General principle of PL spectroscopy. CB and VB stand for conduction band and valence band, respectively.

Source: By the author.

For TMDs, the PL spectrum is highly dominated by excitonic transitions, such as neutral and charged excitons (see Sec. 2.3). As we have seen in previous chapters, excitons are bound electron-hole pairs originating due to the Coulomb interaction between the charge carriers. Usually, excitons can be classified into two limiting cases. For a strong Coulomb interaction, usually in ionic crystals, the electron, and hole are tightly bound together in the same or nearest-neighbor unit cell and are known as Frenkel excitons. (85) For most semiconductors, the electron and hole are only weakly bound, resulting in delocalization at a crystal position. (85) In this case, they are known as Wannier-Mott excitons. Formally, excitons in TMDs can be understood as an intermediate case between Frenkel and Wannier-Mott excitons, since they have small radii due to the reduced dielectric screening but present an electronic structure similar to the Wannier-Mott regime. (44) However, in most cases, the Wannier-Mott description of excitonic effects in TMDs with a few modifications (to account for small exciton radii and large wave function spread in momentum space) is sufficient, and it is the approach used in this dissertation. (87)

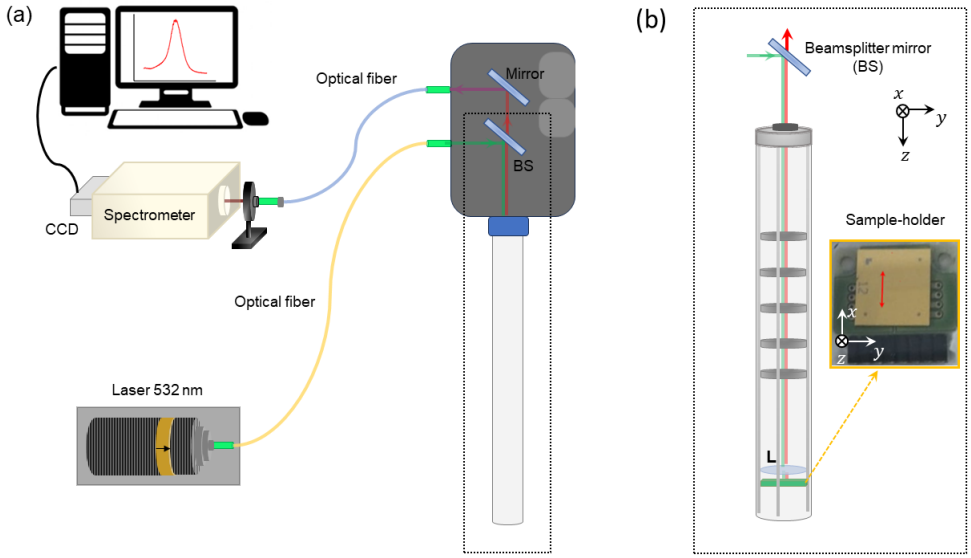

Figure 22 – (a) A schematic illustration of the conventional PL setup used in this dissertation in collaboration with Prof. Marcio Daldin. (b) Detailed representation of the stick where the sample is placed.

Source: By the author.

4.2.3 Raman spectroscopy

Besides photoluminescence, a small fraction of the incident light might be scattered inside the medium. The key difference between these two processes is that photoluminescence involves real excitation of electrons, whereas virtual excitations are sufficient in light scattering. More specifically, light can be elastically scattered, where the frequency is unchanged, or inelastically scattered, with a change in the frequency of the emitted wave. One of the most important cases of inelastic scattering is the Raman scattering mechanism, first reported by C. V. Raman in 1928 and which resulted in his Nobel Prize award in physics in 1930 (88). In solids, the term is usually associated with the scattering of light by optical phonons (quanta of lattice vibrations), but it can be used, in principle, to describe the inelastic scattering by other collective excitations. (89)

The first approach to describe the Raman scattering process is to use the classical macroscopic theory of electromagnetic waves interacting with a medium. If one considers an infinite crystal at a finite temperature with dielectric susceptibility $\overleftrightarrow{\chi}$, the polarization vector $\mathbf{P}$ can be written in terms of the incident electric field $\mathbf{E}$ as (85)

$$\mathbf{P} = \overleftrightarrow{\chi} \cdot \mathbf{E}. \tag{4.8}$$

The electric field is written as a plane wave

$$\mathbf{E}(\mathbf{r}, t) = \mathbf{E}_0(\mathbf{k}_i, \omega_i) \cos(\mathbf{k}_i \cdot \mathbf{r} - \omega_i t), \tag{4.9}$$

where $\mathbf{k}_i$ and ω_i are the wavevector and frequency of the incident light, respectively. Note that fluctuations in the susceptibility tensor $\overleftrightarrow{\chi}$ will induce variations in the polarization

vector. At finite temperatures, those fluctuations are caused mainly by atomic vibrations of the crystal lattice (phonons in quantum mechanics) and can be written in terms of the atomic displacement vector $\mathbf{Q}(\mathbf{r},t)$ as (85)

$$\mathbf{Q}(\mathbf{r},t) = \mathbf{Q}(\mathbf{q},\omega_0)\cos\left(\mathbf{q}\cdot\mathbf{r}-\omega_0 t\right), \tag{4.10}$$

with wavevector $\mathbf{q}$ and frequency ω_0. However, since the amplitudes of these vibrations are small compared to the lattice constant, one can expand $\overleftrightarrow{\chi}$ as a Taylor series in $\mathbf{Q}(\mathbf{r},t)$ to find

$$\overleftrightarrow{\chi}(\mathbf{k}_i,\omega_i,\mathbf{Q}) = \overleftrightarrow{\chi_0}(\mathbf{k}_i,\omega_i) + \left(\frac{\partial\overleftrightarrow{\chi}}{\partial\mathbf{Q}}\right)_0 \mathbf{Q}(\mathbf{r},t) + \ldots, \tag{4.11}$$

where $\overleftrightarrow{\chi_0}$ is the electric susceptibility of the medium without fluctuations. Substituting Eqs. (4.9), (4.10) and (4.11) into Eq. (4.8) and rearranging the terms yields

$$\mathbf{P}(\mathbf{r},t,\mathbf{Q}) = \mathbf{P}_0(\mathbf{r},t) + \mathbf{P}_{ind}(\mathbf{r},t,\mathbf{Q}) + \ldots. \tag{4.12}$$

The term $\mathbf{P}_0$ is given by

$$\mathbf{P}_0(\mathbf{r},t) = \overleftrightarrow{\chi_0}(\mathbf{k}_i,\omega_i)\mathbf{E}_0(\mathbf{k}_i,\omega_i)\cos\left(\mathbf{k}_i\cdot\mathbf{r}-\omega_i t\right) \tag{4.13}$$

and represents the polarization vector oscillating with the same frequency as the incident electromagnetic wave, the so-called Rayleigh scattering. The term $\mathbf{P}_{ind}$ is given by

$$\begin{aligned}\mathbf{P}_{ind}(\mathbf{r},t,\mathbf{Q}) =& \frac{1}{2}\left(\frac{\partial\overleftrightarrow{\chi}}{\partial\mathbf{Q}}\right)_0 \mathbf{Q}(\mathbf{q},\omega_0)\mathbf{E}_0(\mathbf{k}_i,\omega_i) \\ & \left\{\cos((\mathbf{k}_i-\mathbf{q})\cdot\mathbf{r}-(\omega_i-\omega_0)t) + \cos((\mathbf{k}_i+\mathbf{q})\cdot\mathbf{r}+(\omega_i+\omega_0)t)\right\}.\end{aligned} \tag{4.14}$$

We can see that the induced polarization has two components representing the inelastic light scattered by the medium. The first term has a wavevector $\mathbf{k}_S = \mathbf{k}_i - \mathbf{q}$ and a frequency $\omega_i - \omega_0$ and is called Stokes scattering. The second term has a wavevector $\mathbf{k}_{AS} = \mathbf{k}_i + \mathbf{q}$ and a frequency $\omega_i + \omega_0$ and is called anti-Stokes scattering. The physical interpretation of those two scattered fields will become clearer when the quantum mechanical approach is introduced. Before that, we note that energy and momentum must be conserved in both cases. For typical experiments in the backscattered configuration, it implies that the maximum value of $|\mathbf{q}|$ is about twice the photon wavevector. If the incoming light is in the visible range (e.g., 500 nm), the wavevector is in the order of 10^7 m^{-1}, which is about 1/1000 smaller than the wavevector of a common crystal with a lattice constant of $a \approx 3$ Å. In other words, the wavevector $\mathbf{q}$ is limited to the center of the Brillouin zone around the Γ point. Finally, we point out that

$$\overleftrightarrow{R} = \left(\frac{\partial\overleftrightarrow{\chi}}{\partial\mathbf{Q}}\right)_0 \mathbf{Q}(\mathbf{q},\omega_0) \tag{4.15}$$

is known as the first-order Raman tensor, and it is very useful for determining the Raman selection rules based on the symmetry requirements of a particular medium (for more

details, see Ref. (85)). The intensity of the scattered radiation can be calculated by considering the time-averaged power radiated by the induced polarizations into a unit solid angle. (85) In terms of the Raman tensor, the intensity is proportional to

$$I_s \propto |\mathbf{E}_i \cdot \overleftrightarrow{R} \cdot \mathbf{E}_s|^2, \tag{4.16}$$

where $\mathbf{E}_i$ and $\mathbf{E}_s$ are the polarization of the incident and scattered radiations, respectively.

Although the classical theory is instructive for an initial understanding of the Raman scattering process, it gives an incomplete picture since the radiation fields are not explicitly quantized, nor the electron-phonon interaction is included. To solve this problem, a quantum mechanical formalism is needed. Here, we will briefly introduce this topic, but a more detailed explanation can be found in Refs. (85,89,90). The Hamiltonian of the system is given by (85)

$$H = H_e + H_p + H_r + H_{er} + H_{ep} = H_0 + H_1. \tag{4.17}$$

The term $H_0 = H_e + H_p + H_r$ represents the unperturbed Hamiltonian, where H_e, H_p and H_r are the Hamiltonian from the electron, phonon, and radiation, respectively. The other term $H_1 = H_{er} + H_{ep}$ corresponds to the Hamiltonian of perturbation, where H_{er} describes the interaction between the electron and the radiation, and H_{ep} describes the electron-phonon interaction. Schematically, the one-phonon Raman scattering can be described in the following steps:

1. The system is the initial state $|i\rangle$;
2. An incident photon is absorbed by the medium, creating an electron-hole pair (via H_{er}) and sending the system to the state $|a\rangle$;
3. The electron-hole pair is inelastically scattered to another state $|b\rangle$ by either emitting (Stokes scattering) or annihilating (anti-Stokes scattering) a phonon via the Hamiltonian H_{ep};
4. The electron-hole pair returns to the ground state by recombining radiatively and emitting a photon. The final state is denoted $|f\rangle$.

Figure 23a shows a schematic illustration of this process. Since we have a spontaneous emission of a photon in the last step, this process is known as spontaneous Raman scattering and, just as in the PL case, a rigorous quantization of the radiation fields is required for a complete understanding of the process. It is important to point out that although the electrons remain unchanged after the scattering process is finished, they mediate the Raman scattering of phonons. Moreover, we can see that the anti-Stokes process can only occur if the system is initially excited, meaning that the intensity of the Stokes scattering is usually much higher than the anti-Stokes scattering. One can use the third-order

perturbation theory described in the last section to calculate the scattering probability for phonons. An elegant description using Feynman diagrams is provided in Ref. (85). Finally, for completeness, we comment that scattering processes involving more than one phonon can be calculated using higher orders of perturbation.

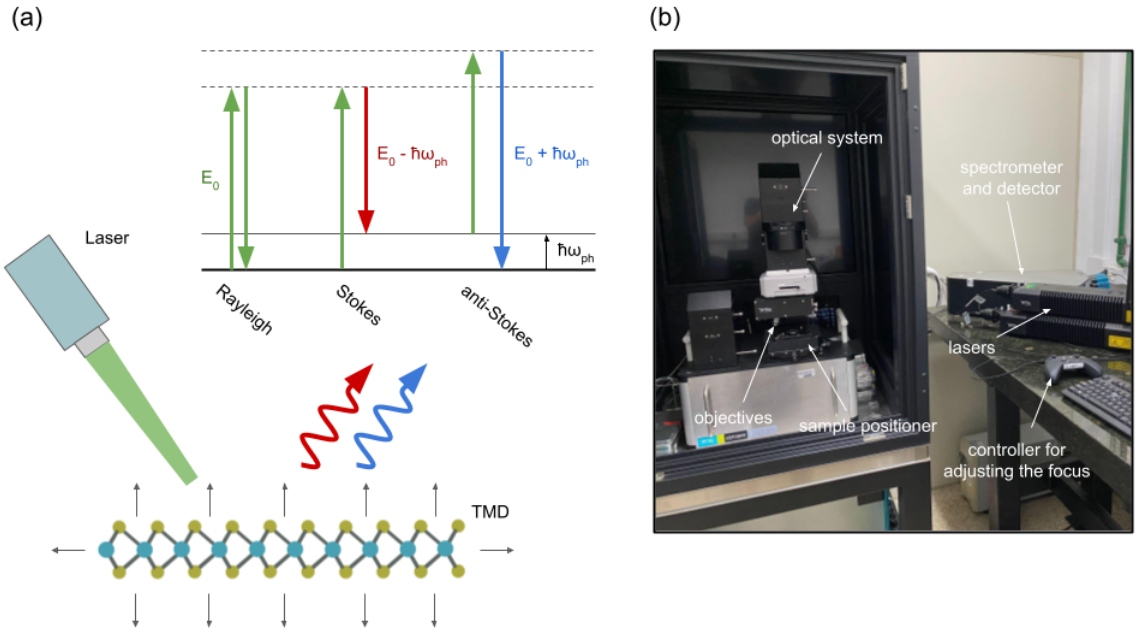

Figure 23 – (a) Schematic diagram of the different possibilities of light scattering in solids. The dashed lines correspond to virtual states. (b) Photo of the confocal Raman microscopy setup used in this dissertation.

Source: By the author.

Experimentally, the measurement of a Raman spectrum requires the following components: a source of monochromatic light, an optical system to collect the scattered field, a spectrometer to analyze the spectra, and a sensitive detector to detect the scattered radiation. Since Raman signals are usually small, the system must be optimized for meaningful measurements. In this work, the Raman spectra were acquired using a WITec alpha300 RAS confocal Raman microscope (for more information on confocal microscopy see Appendix A) in the backscattering configuration, with all the measurements being made at room temperature. Figure 23b shows a photo of the equipment. A more detailed schematic of the Raman measurement system is shown in Fig. 24a. The excitation source used was a CW diode-pumped laser centered at 532 nm with a spot size of approximately 500 nm and it is transmitted to the microscope via a single-mode optical fiber. Then, it is reflected by a dichroic mirror (high transmission starting at 95 cm^{-1}) and focused onto the sample by a 100X objective lens with a NA=0.9. Control of the x and y positions is made by manual stages with micrometer resolution. The emitted radiation passes through the dichroic mirror and a 532 nm long-pass filter, which allows only wavelengths longer than 532 nm to be transmitted. Subsequently, the signal is transmitted via a multi-mode optical

fiber to the acquisition system. The spectrometer comprises a 1200 lines/mm diffraction grating (blaze at 500 nm) and a CCD photon detector.

The laser power was kept at 26.5 mW in all experiments to obtain a good signal-to-noise ratio. Regarding the acquisition process, two types of measurements were made. A single spectrum with high integration time and a number of accumulations was acquired for different regions on the sample to study the general behavior of the Raman signals. For MoS_2 deposited over SiO_2/Si, an integration time of 10 s and 3 accumulations was used. For MoS_2 deposited over the gold substrate or the metallic gratings, we chose an integration time of 10 s and 10 accumulations since the signal is weaker in those regions. Moreover, hyperspectral maps were acquired to investigate the spatial distribution of the Raman signals. It is important to point out that the system can make automated scanning at a small area with a high resolution using a PZT. The lateral displacements can also be made manually for the location of the structures. Here, we used an integration time of 0.2 s and 1 accumulation. Fig. 24b shows a sequence of steps illustrating the acquisition and processing of the color maps. First, a sample region is selected using the optical image (i). After the measurement, an intensity map is generated (ii), where each pixel (red square) in the image represents a single spectrum. Then, the baseline is subtracted (iii) for each pixel using a spline interpolation to acquire the corrected spectra (iv). Finally, each peak was fitted with a Lorentzian function to study common parameters such as amplitude, peak position, and linewidth. We should note that before each measurement, the Raman signals were calibrated using the silicon peak position (for our experiments, it was ~ 522 cm^{-1}). All analyses were made using the WITec Project FIVE 5.2 software.

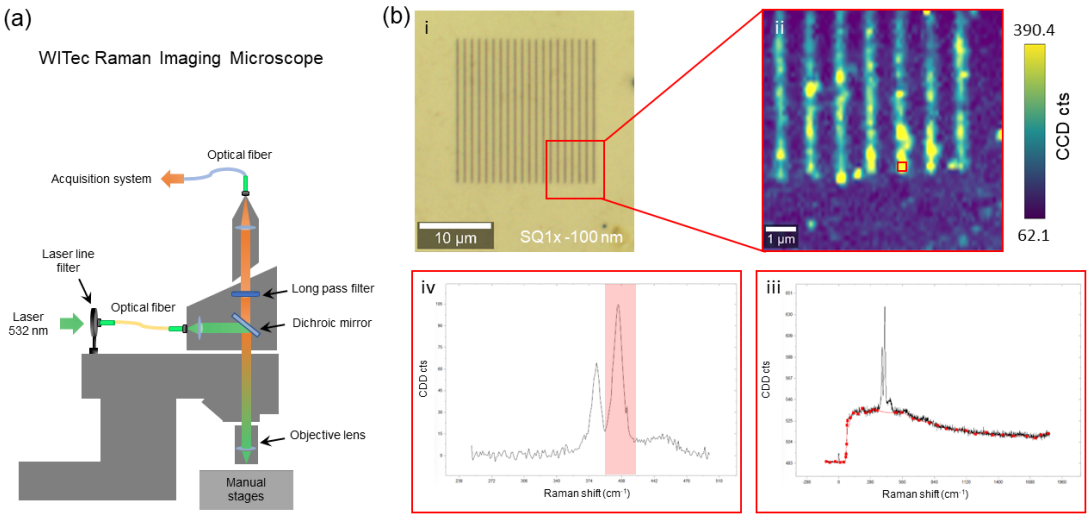

Figure 24 – (a) Detailed schematic diagram the WITec alpha300 RAS confocal Raman microscope. (b) A sequence of steps illustrating the acquisition and processing of the color maps.

Source: By the author.

4.3 Numerical simulations

Since Maxwell's equations can only be solved analytically for simple problems, we performed numerical simulations on the gold gratings to understand how the plasmonic platform might influence the physical properties of the MoS_2 monolayers. One of the most popular techniques for solving electromagnetic problems is the finite-difference time-domain (FDTD) method, first proposed by K. Yee in 1966. (91) The idea is to discretize Maxwell's equations in space and time using second-order centered difference approximations, so dx, dy, dz, and dt become Δx, Δy, Δz, and Δt, respectively. The ingenuity of Yee's algorithm resides in how the electric and magnetic fields are allocated in space and how the time evolution of the system is calculated (for more details, see Ref. (92)). The cell locations are defined so the electric field components pass through the grid lines as shown in Fig. 25a. Additionally, the electric and magnetic field components are shifted in space by half a cell. This unit cell, known as the Yee cell, allows the calculation of the spatial derivatives of the fields. For instance, the derivative of H_z with respect to x at the point $(i, j, k + 1/2)$ at time $n\Delta t$ is

$$\left.\frac{\partial H_z}{\partial x}\right|^{n}_{i,j,k+1/2} = \frac{H_z|^{n}_{i+1/2,j,k+1/2} - H_z|^{n}_{i-1/2,j,k+1/2}}{\Delta x} + \mathcal{O}[(\Delta x)^2]. \tag{4.18}$$

The other five spatial derivatives are obtained similarly. For the time derivatives, the fields E and H are updated by one half-time step known as leapfrog time-marching. (92) More specifically, the components of the magnetic field are defined at half-time steps, resulting

$$\left.\frac{\partial E}{\partial t}\right|^{n+1/2} \approx \frac{E|^{n+1} - E|^{n}}{\Delta t} = \frac{1}{\varepsilon}(\boldsymbol{\nabla} \times H)^{n+1/2} \tag{4.19a}$$

$$\left.\frac{\partial H}{\partial t}\right|^{n+1} \approx \frac{H|^{n+3/2} - H|^{n+1/2}}{\Delta t} = -\frac{1}{\mu}(\boldsymbol{\nabla} \times E)^{n+1} \tag{4.19b}$$

Combining the spatial arrangement and leapfrog time-marching methods allow the complete discretization of Maxwell's equations and the subsequent calculation of the spatial and temporal field profiles.

In this work, the Yee algorithm was implemented using the Ansys Lumerical FDTD software. It allows the design and modeling of plasmonic devices with advanced functionalities, such as 3D CAD importing, fully vectorial, high NA beam sources, and a comprehensive materials database for dielectric functions. For example, dispersive materials with tabulated refractive index or specific models such as Drude or Lorentz can be used. Additionally, the software is equipped with mesh refinement options, which is advantageous for complex structures that need a smaller mesh. In all simulations, perfectly matched layers (PMLs) were used on each boundary to eliminate unwanted reflections at the interface, but other boundary conditions such as periodic or Bloch can also be employed. Finally,

a Gaussian beam with high NA was used as the excitation source to closely mimic the experimental conditions in the simulation. As an example, Fig. 25b shows the simulated electric field distribution over a gold grating, where the width, depth, and periodicity (distance to the next slit) are 50 nm, 80 nm, and 1000 nm, respectively. The excitation source was a focused Gaussian beam (NA=0.9) centered at 800 nm and polarized perpendicular to the slits (x direction).

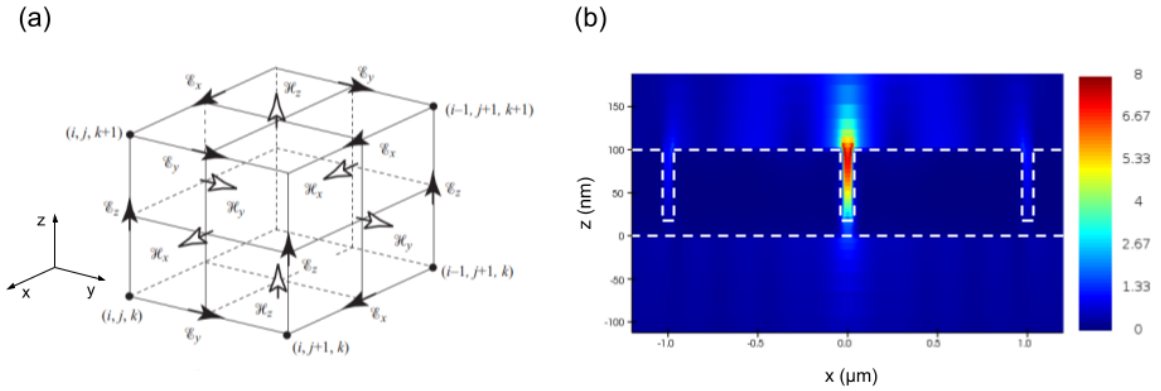

Figure 25 – (a) Yee cell and subsequent assignment of fields. (b) FDTD simulation of the electric field distribution over a gold grating excited by a focused Gaussian beam polarized in the x direction.

Source: (a) Adapted from INAN; MARSHALL. (92); (b) By the author.

5 RESULTS AND DISCUSSION

In this chapter, the results of our work are presented and discussed. First, we describe the structural characteristics of our device. Then, the vibrational properties of MoS_2 at different sample regions are investigated, where strain, doping, and plasmonic effects play a critical role. Finally, using photoluminescence measurements, we studied how those external perturbations might affect the exciton and trion emissions, the main optical transitions in 2D TMDs.

5.1 Morphological characterization of MoS_2/Au hybrid device

The first step to characterizing the MoS_2/Au hybrid device was to investigate its morphological properties. As described in Sec. 4.1.1, two square gratings with different geometric parameters were studied in this dissertation. Both have a nominal slit depth of 50 nm and periodicity of 1000 nm, but widths of 50 and 100 nm. They are denoted as SQ1-50 and SQ1-100 (SQ stands for square). Figure 26 shows a scanning electron microscopy (SEM) image of both structures before the MoS_2 transfer procedure where the periodic array of slits produced by the e-beam lithography combined with ion-beam assisted etching can be seen. The gratings have an area of approximately 20 x 20 μm^2. However, due to a low lateral resolution, the width of slits cannot be properly measured, but they appear smaller for the SQ1-50 structures. We should mention that the SEM technique is outside the scope of this work, but more information can be found in Ref. (93).

AFM images were acquired to better understand the morphology of our devices when the monolayer is deposited over the metallic gratings. Figure 27 shows the height and phase images for the SQ1-50 and SQ1-100 structures covered with a MoS_2 monolayer. The patterned array of slits for both structures has an area of approximately 20 x 20 μm^2, corroborating the SEM measurements. Moreover, one can see that the two gratings exhibit a fairly pronounced degree of morphological heterogeneity. Interestingly, a variety of defects/imperfections are readily observed in both images, which might have originated from the various fabrication processes. For instance, the e-beam evaporation method used for the deposition of the Au film can create small metallic clusters due to non-uniform film deposition. The ion-beam etching phase can also form rough surfaces when used on polycrystalline substrates. Another reason for the rough surface morphology can be the PMMA residues left over from the lithography and transfer procedures. Finally, the explanation might be contamination from air exposure since these samples have been used for other experiments under ambient conditions before. We should also point out that, although the phase images might suggest that the regions with the slits and defects are

softer than other areas, a conclusive interpretation is challenging since the phase is not only sensitive to variations in composition and viscoelasticity but topometric differences as well.

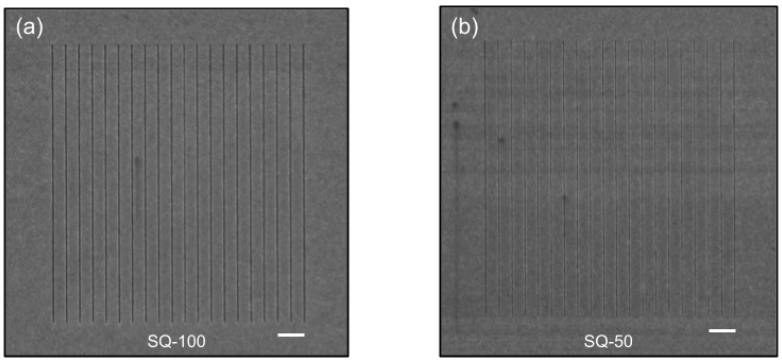

Figure 26 – (a,b) Scanning electron microscopy images for the SQ1-100 (a) and SQ1-50 (b) gratings. The scale bar is 2 μm.

Source: By the author.

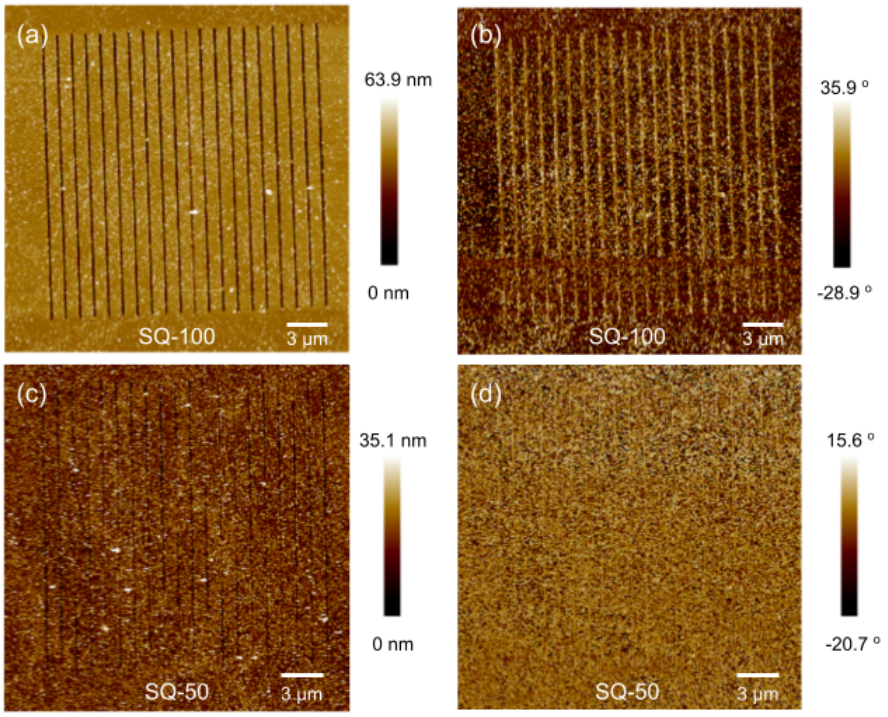

Figure 27 – (a,b) Topographical (a) and phase (b) images for the SQ1-100 structure. (c,d) Topographical (c) and phase (d) images for the SQ1-50 structure.

Source: By the author.

Figure 28 shows magnified, high-resolution topographical and phase images of the MoS_2 deposited over the structures and their respective height profiles. Even in this small

region, the slit width varies considerably. The SQ1-100 ranges from 104 to 128 nm with an average value of 111 nm, whereas for the SQ1-50, it lies between 55 and 79 with an average value of 67 nm. Regardless of those variations, one important characteristic we can measure is the height profile of the monolayer when suspended over the slit (Figs. 28c and 28f). For the SQ1-100, the film deformation at the slits was approximately 47 nm, and, in some regions, the film is actually in contact with some defects at the bottom of the slit. In contrast, the height deformations for the SQ1-50 are 39 nm since the slit width is smaller in this case. Nevertheless, those deformations are much larger than MoS_2 monolayer suspended over the Si substrate. For instance, BERTOLAZZI *et al.* measured the height profile of MoS_2 suspended over an array of circular holes 550 nm in diameter and found deformations on the order of 5 nm. (2) The reason for a large film deformation in our case originates from the strong interaction between MoS_2 and the gold substrate, which has been reported in other works. (94, 95) More specifically, the interaction between the S and the Au atoms has been described as a covalent-like quase-bonding at the film/substrate interface. (96) In contrast, the height deformations for the SQ1-50 are on the order of 39 nm since the slit width is smaller in this case. Besides vertical deformations, the strong interaction of the semiconducting monolayer and gold substrate combined with a lattice mismatch of 5.4% (97) leads to an induced strain at the interface, which will be discussed in the next section.

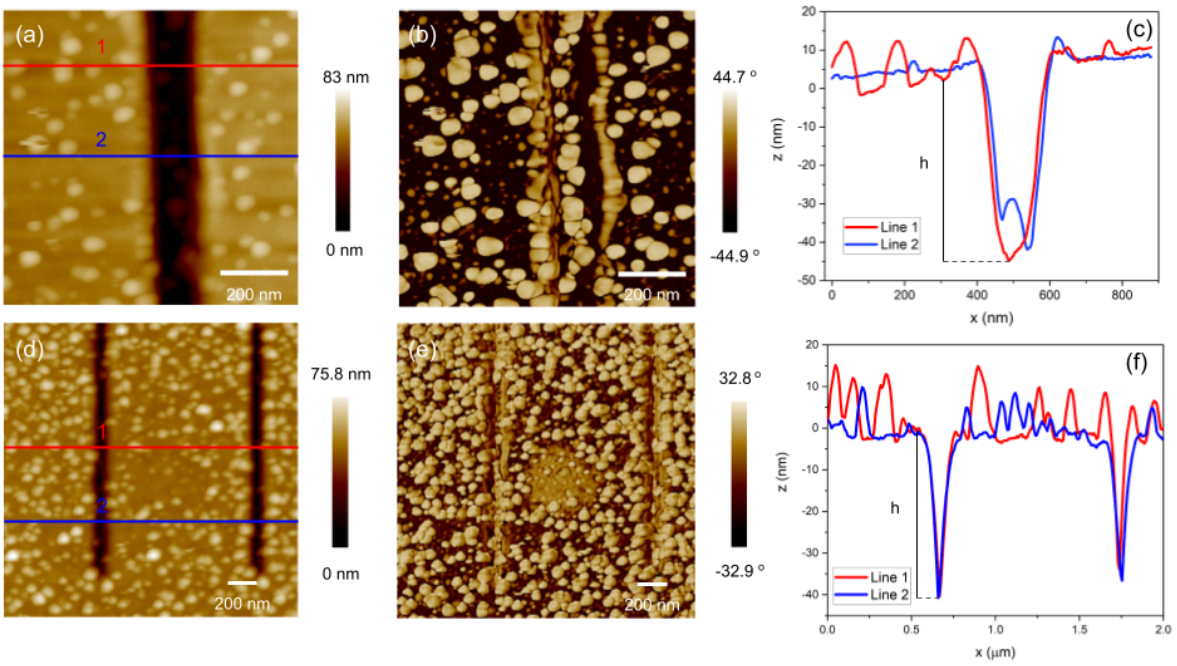

Figure 28 – (a,b) High-resolution topographical (a) and phase (b) images for the SQ-100 structure. (c) Corresponding height profile. (d,e) High-resolution topographical (d) and phase (e) images for the SQ-50 structure. (f) Corresponding height profile.

Source: By the author.

5.2 Vibration properties probed by Raman spectroscopy

5.2.1 Characteristic Raman modes of MoS_2

Given the morphology analysis presented in the last section, particularly the strong interaction between MoS_2 and gold, we investigated how the vibrational properties of the monolayer are affected by the Au substrate and metallic grating. As described in Sec. 4.2.3, Raman spectroscopy is an effective technique to study the lattice vibrations of crystals, which can be classified based on the irreducible representation of the symmetry group. (98) Figure 29a shows the phonon dispersion curve of MoS_2 monolayer calculated by density functional theory within the local density approximation. (53) It has three acoustic and six optical branches at the Γ point, which is the only allowed phonon wavevector for first-order Raman processes when using visible light. The most important Raman active modes for MoS_2 monolayers (TMD monolayers in general) are the in-plane mode E' and out-of-plane A_1', since their peak position shows opposite trends as a function of the thickness, allowing the layer number identification through their relative frequency difference. (53, 54) The displacement of the E' and A_1' modes are shown in Fig. 29b (for completeness, the lower energy mode E'' is also shown since it is observed in some of our experiments). A typical measured Raman spectrum of MoS_2 monolayer over SiO_2/Si can be seen in Fig. 29c, where the spectrum for the semiconductor material had to be amplified 100 times because of the strong Raman signal from the silicon substrate. The frequency difference of $\sim 19\ \mathrm{cm}^{-1}$ between the A_1' and E' modes confirms that MoS_2 flakes are indeed monolayers. (53) Moreover, second-order modes of MoS_2, commonly known as 2LA band in the literature (99), can be seen. However, a comprehensive spectral analysis of those higher-order modes is beyond the scope of this dissertation.

The Raman spectrum is significantly changed when the MoS_2 is deposited over another substrate, such as gold or gold gratings. Figure 30 shows the Raman spectra of MoS_2 monolayer deposited over the Au film or the metallic gratings SQ1-100 and SQ1-50 described in the last section. The two structures were also rotated 90° to study the polarization effect. From now on, the unrotated gratings are denoted SQ1x-100 and SQ1x-50, whereas the 90-degree-rotated gratings are denoted SQ1y-100 and SQ1y-50. The characteristic E' and A_1' peaks as well as E'' and second-order modes can be observed in all structures. One can see that the regions where the MoS_2 is deposited over the gold substrate, which are called supported regions in this work, show that the intensity of the E' mode is greater than the A_1'. In contrast, for the regions where the monolayer is deposited over the gratings, denoted as suspended regions, this intensity relation is altered, with a greater intensity of the out-of-plane lattice vibration in comparison to the in-plane mode. Besides, the peak positions of the E' and A_1' modes also change in comparison to the MoS_2/Si. More specifically, both modes soften in the supported and suspended regions, although the frequency separation is greater in the supported case.

Since many factors can be responsible for altering the amplitude and frequency position of a Raman mode, such as strain, doping, and plasmonic effects, Raman mapping was used to extract relevant statistical information on the physical processes involved in our system.

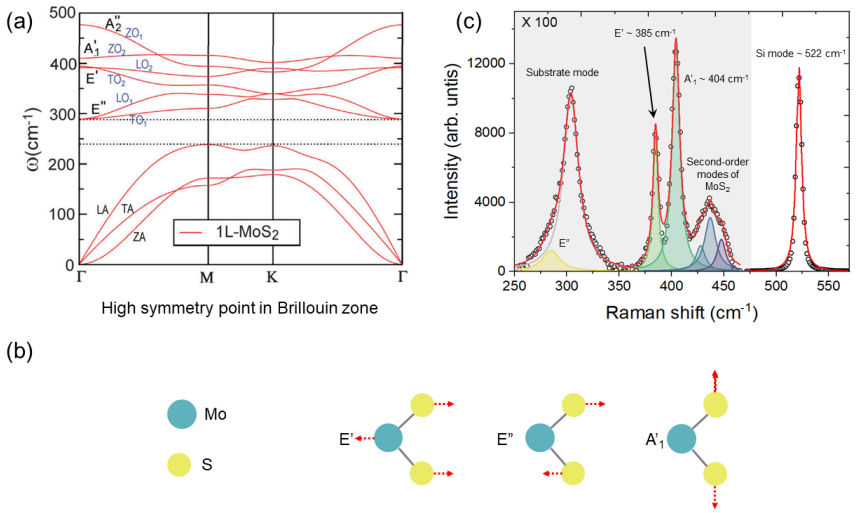

Figure 29 – (a) Phonon dispersion curve for MoS_2 monolayer calculated using DFT. (b) Mode displacement for the E', A_1', and E'' modes. (c) Raman spectrum of MoS_2 over Si substrate.

Source: (a) MOLINA; WIRTZ. (53); (b,c) By the author.

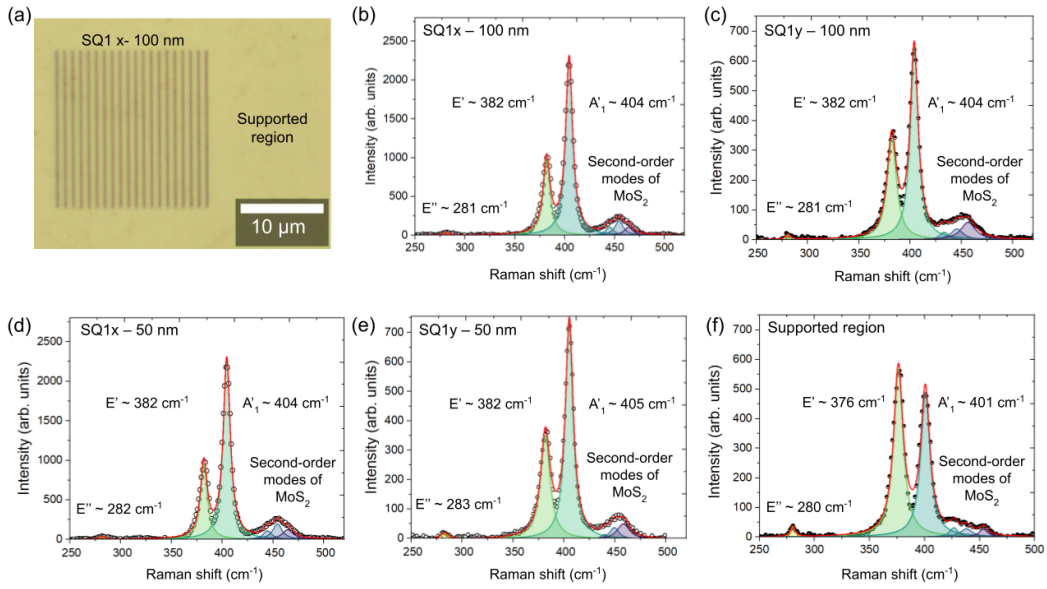

Figure 30 – (a) Representative optical image showing the suspended and supported regions. (b-f) Raman spectra of MoS_2 monolayer deposited over the square gratings (b-e) and the gold substrate (f).

Source: By the author.

5.2.2 Amplitude and peak position for different regions

Raman hyperspectral mapping analysis was carried out for all the structures on a 8 x 8 μm^2 area, exemplified in the Fig. 31a,d for the SQ1x-100 and SQ1x-50 structures. To increase the resolution in the direction of the grating, a matrix of 80 x 50 spectra was collected for the SQ1x-100 and SQ1x-50, whereas for the SQ1y-100 and SQ1y-50, the matrix consisted of 50 x 80 spectra. Each pixel in the final image corresponds to a Raman spectrum, allowing the visualization of the spatial distribution of various parameters from a particular mode, such as amplitude, peak position, and linewidth. Figure 31b,c,e,f shows the measured A_1'/E' intensity ratio in the scanned area for all structures. One can see a general trend in the relationship between the amplitudes of both modes. More precisely, the A_1'/E' ratio is smaller than one for the Au-supported MoS_2 sample and it is more significant than one when the film is suspended, confirming the initial observation previously discussed (local variations in this trend can be seen due to non-uniformity in the MoS_2 monolayer). Although the gold substrate affects the mode displacement of both modes, we have found that the amplitude of the A_1' mode is more sensitive to this effect. This behavior can be explained by the strong interaction between the Au and S atoms, which restricts the amplitude of the out-of-plane lattice vibration when the MoS_2 is in contact with the gold substrate. (96,100) Indeed, this interaction has been used for the exfoliation of large-area TMD monolayers by gold-assisted mechanical exfoliation. (101) For the suspended regions, the Au-S interaction decreases, allowing the proper mode displacement for the A_1' mode.

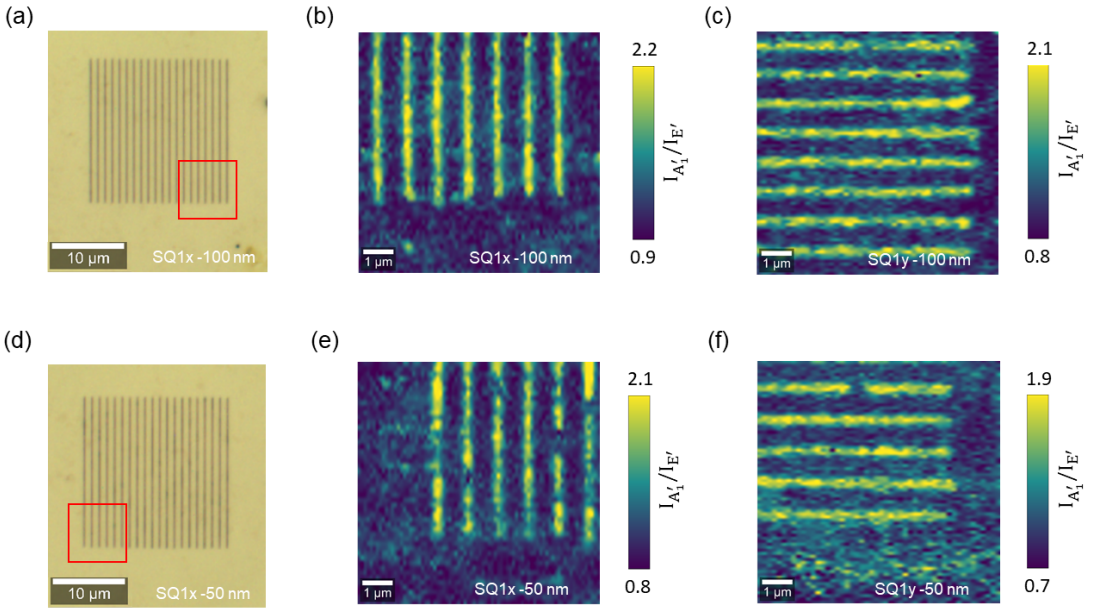

Figure 31 – (a,d) Optical image for the SQ1x-100 (a) and SQ1x-50 (d) illustrating the region where the Raman mapping was performed. (b,c,e,f) Amplitude mapping showing the measured A_1'/E' intensity ratio for all structures.

Source: By the author.

To further study how the metal substrate and metallic gratings modify the Raman spectra of the MoS_2 monolayer, we measured the spatial distribution of the peak frequency position of the two characteristic Raman modes, denoted $\omega_{E'}$ and $\omega_{A_1'}$. Figure 32 shows the color maps of the E' and A_1' peak frequencies as well as the peak position as a function of the position along the two lines indicated in the maps for the SQ1x-100 structure. One can see that the E' mode is well-modulated by the grating pattern. In both regions, the peaks are red-shifted (the Raman shifts are smaller) in comparison to the MoS_2 over the Si substrate, and these shifts are larger for the supported case (see Fig. 32b). In contrast, the position of the A_1' shows a less pronounced correlation with the supported and suspended regions, where a clear distinction between the two topographical cases, comparable to the E' mode, cannot be made. However, the peaks also show a slight red-shift regarding the silicon case. The color maps of the $\omega_{E'}$ and $\omega_{A_1'}$ for the other structures showed a similar pattern, so they are presented in Appendix B. In the literature, the frequency changes of the vibrational modes of the MoS_2 monolayer similar to ours have been reported, which were attributed to various physical mechanisms, such as strain, doping, and plasmonic effects. (102, 103) In the next section, we investigate those mechanisms to gain additional insight into the underlying physics that may be at play.

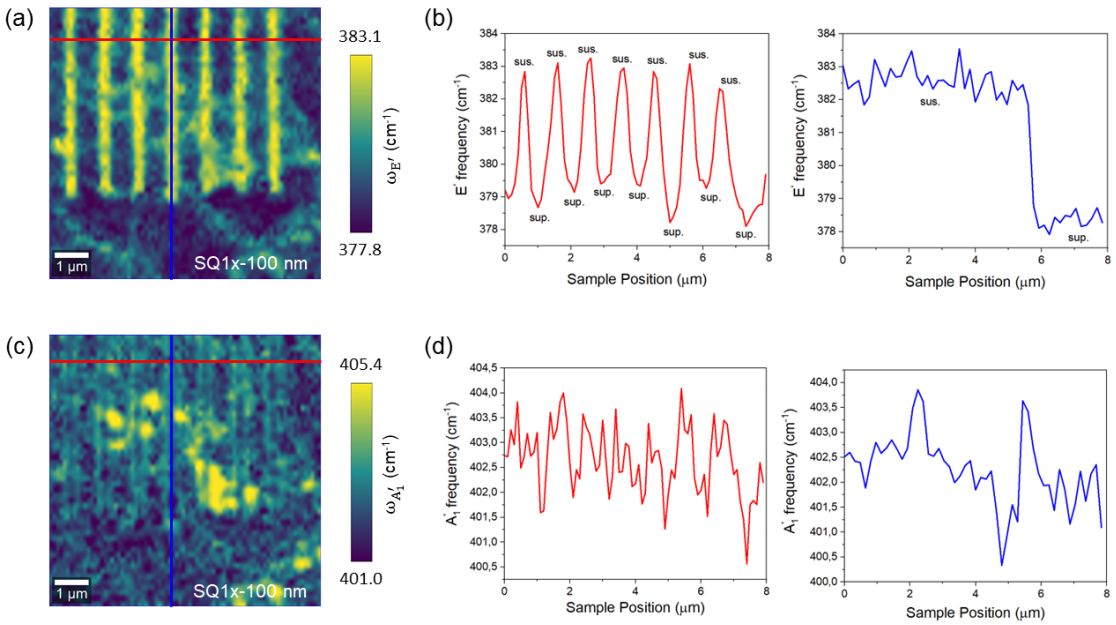

Figure 32 – (a) Color map of the peak position for the E' mode. (b) Peak position as a function of the position along two lines in (a). (c) Color map of the peak position for the A_1' mode. (d) Peak position as a function of the position along two lines in (c). Both maps correspond to the SQ1x-100 structure. In the abbreviations, "sus." means suspended, and "sup." means supported.

Source: By the author.

5.2.3 Observation of strain, doping, and plasmonic effects

An effective method for quantitatively evaluating the contributions of strain, doping, and plasmonic effects on the frequency changes of the Raman modes is to construct a correlative plot of the A_1' vs E' peak frequencies from their respective color maps. Such an approach has been successfully applied to the characterization of the 2D and G peaks in graphene (104–106) and has been recently used for MoS_2 monolayer as well. (102,107) Here, we have also applied this method and, for better comprehension, have separated the analysis for the SQ1-100 and SQ1-50 structures.

Before we present our results, we should briefly explain the effects of strain and doping in the frequency changes of the Raman modes. Strain refers to the deformation of an object relative to a reference configuration. For 2D materials, the two commonly observed cases of strain are the biaxial and uniaxial strains. The former refers to deformations in two of the three spatial directions (usually the plane defined by the 2D material), while the latter considers deformations where the material is bent or stretched along a single axis. Following the works of LI *et al.* (104) and MOHIUDDIN *et al.* (105), for a phonon mode m with frequency ω_m, the change in the peak frequency due to the strain is associated with two parameters: Grüneisen parameter γ_m and the shear deformation potential β_m. By definition, γ_m is

$$\gamma_m = -\frac{1}{\omega_m}\frac{\partial \omega_m}{\partial \epsilon_h} \tag{5.1}$$

and β_m is

$$\beta_m = \frac{1}{\omega_m}\frac{\partial \omega_m}{\partial \epsilon_s}. \tag{5.2}$$

The term $\epsilon_h = \epsilon_{ll} + \epsilon_{tt}$ is the hydrostatic component of the applied strain, with ϵ_{ll} the longitudinal component of the strain and ϵ_{tt} is the transverse component of the strain. Also, $\epsilon_s = \epsilon_{ll} - \epsilon_{tt}$ is the shear component of the applied strain. The frequency change of a particular mode $\Delta\omega_m = \omega_m - \omega_m^0$, where ω_m^0 is the reference frequency, is given by (108)

$$\Delta\omega_m = -\omega_m^0 \gamma_m \epsilon_h \pm \frac{1}{2}\beta_m \omega_m^0 \epsilon_s. \tag{5.3}$$

For a biaxial strain, we have $\epsilon_{ll} = \epsilon_{tt} = \epsilon$, so Eq. (5.3) reduces to

$$\Delta\omega_m = -2\omega_m^0 \gamma_m \epsilon. \tag{5.4}$$

However, under uniaxial strain we have $\epsilon_{ll} = \epsilon$ and $\epsilon_{tt} = -\nu\epsilon$, where ν is the Poisson's ratio. (105) Then, Eq. (5.3) is given by

$$\Delta\omega_m = -\omega_m^0 \gamma_m (1-\nu)\epsilon \pm \frac{1}{2}\beta_m \omega_m^0 (1+\nu)\epsilon. \tag{5.5}$$

In the case of a biaxial strain, a common cause is the lattice mismatch at the interface of two crystal structures, since the material under study will usually be deposited over

a substrate. In contrast, the presence of an external force in just one direction usually causes an uniaxial strain, which can be seen in materials suspended over slits or grooves. Figure 33 shows a schematic diagram of the two types of strain considered in this work for the case of a TMD monolayer. Besides, charge doping also affects the peak position of the Raman modes. It follows that the position is altered by a factor of $k_m n$, where k_m is the shift rate of Raman peak as a function of the electron concentration n. (102, 109) Including this effect in Eq. (5.3), we have that the final expression for the changes in the Raman frequency is given by

$$\Delta\omega_m = -\omega_m^0 \gamma_m \epsilon_h \pm \frac{1}{2}\beta_m \omega_m^0 \epsilon_s + k_m n. \tag{5.6}$$

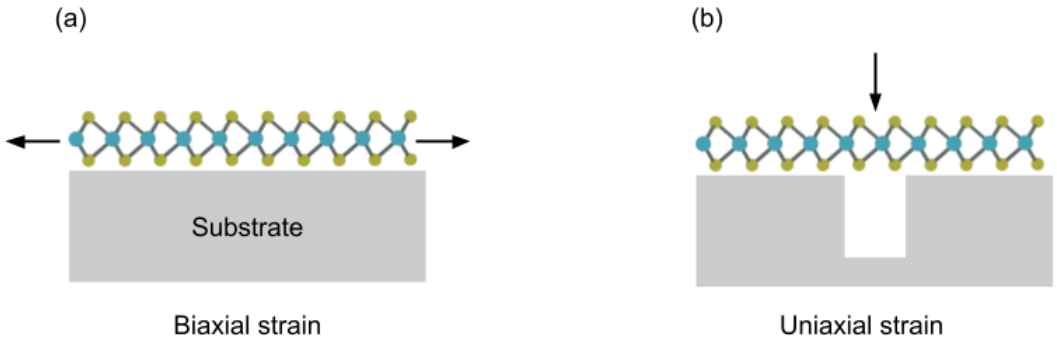

Figure 33 – (a,b) Schematic diagram for the two types of strain considered in this work, namely the biaxial (a) or uniaxial (b) strain.

Source: By the author.

In the case of MoS_2, these parameters are reported in the literature. For a biaxial strain, the Grüneisen parameters for the E' and A_1' modes of MoS_2 monolayer are $\gamma_{E'} = 0.68$ and $\gamma_{A_1'} = 0.21$, respectively. (110) For an out-of-plane uniaxial strain, to the best of our knowledge, only the Grüneisen parameter and shear deformation potential for the E' mode is known since the A_1' mode is essentially insensitive to applied strain. (111) Those values are $\gamma_{E'} = 1.1$ and $\beta_{E'} = 0.78$. (112) Also, the Poisson's ratio is $\nu = 0.29$. (113) For the case of electron doping, the shift rates for each mode are $k_{E'} = -0.33$ x 10^{-13} cm and $k_{A_1'} = -2.2$ x 10^{-13} cm. (102) Finally, the reference frequencies for the peak positions of the E' and A_1' Raman modes are taken from a suspended MoS_2 membrane, where the substrate effects can be excluded and the deformations can be controlled. The values are $\omega_{E'}^0 = 385$ cm^{-1} and $\omega_{A_1'}^0 = 405$ cm^{-1}. (110)

Given this theoretical background, we can present and discuss our results. The correlative plot of the A_1' vs E' peak frequencies for the MoS_2 monolayer deposited over Si or Au substrate is shown in Fig. 34. To help the understanding of this plot, parallel lines corresponding to constant biaxial strain or constant doping were drawn, which can be

calculated by fixing the values of ϵ or n in Eq. (5.6) and solving the linear set of equations for the A_1' and E' modes. The straight black line represents the case for $\epsilon = 0$, and the dashed black lines parallel to it correspond to $\pm 0.3\%$ variations in strain. Correspondingly, the straight red line represents the case for $n = 0$, and the dashed red lines correspond to ± 0.4 x 10^{13} cm^{-2} variations in the electron doping. The lines of zero strain and zero doping cross at the point $(385, 405)$ cm^{-1}, which represents the reference case of free-standing MoS_2. From the Fig. 34, the MoS_2 monolayer deposited over SiO_2/Si experiences a slight compressive strain with an average value of $\epsilon = -0.1\%$, which might be related to the adhesion properties of MoS_2 monolayer over the silicon substrate. (114) In addition, we observe an average electron density of $n = 0.1$ x 10^{13} cm^{-2} corresponding to a n-type doped film. This can be explained by the natural propensity of MoS_2 monolayer to exhibit n-type conductivity when grown via CVD-based methods, where hydrogen present during the growth process provides an effective donor level near the conduction band minima. (115)

For the MoS_2 deposited over the gold substrate, one can see that the data cloud is located in a region of the $\epsilon - n$ plane corresponding to a tensile biaxial strain and n-type doping. Although the supported regions for the SQ1-100 and SQ1-50 should be essentially the same, small variations in morphology might lead to slightly different substrate-induced effects. Expecting this behavior, we show in Fig. 34 two graphs corresponding to the supported regions near SQ1-100 and SQ1-50 structures. The average tensile strains and electron concentrations for the supported regions near the SQ1-100 are $\epsilon = 1\%$, $n = 0.3$ x 10^{13} cm^{-2} (SQ1x-100) and $\epsilon = 1\%$, $n = 0.3$ x 10^{13} cm^{-2} (SQ1y-100). A tensile biaxial strain at the interface originates from the lattice mismatch between MoS_2 and Au, in which the lattice parameter of Au is about 5.4% larger than MoS_2. (97) Other authors have measured strains similar to ours for the MoS_2/Au system, where large ϵ values up to 1.2% have been observed. (100) Interestingly, the measured n-type doping for the supported region, which is higher than MoS_2/Si, is contrary to previous works that observed an electron transfer from MoS_2 to Au. (116) However, one should note that transferred MoS_2 monolayer grown by CVD-based methods usually encloses a buffer layer of air and water contaminations, preventing a good contact with the metal substrate, effectively preserving the natural n-type. (117) In addition, the MoS_2/Si and MoS_2/Au regions are very distant from each other, so variations of the concentrations of hydrogen gases are expected, which would also influence the doping levels. From Fig. 34b, one can see that the behavior of the supported regions near SQ1-50 structures is very similar to the regions near the SQ1-100 gratings. The average tensile strains and electron concentrations are $\epsilon = 0.9\%$, $n = 0.3$ x 10^{13} cm^{-2} (SQ1x-50) and $\epsilon = 0.9\%$, $n = 0.2$ x 10^{13} cm^{-2} (SQ1y-50). A smaller tensile strain for the supported regions near the SQ1-50 structures in comparison to the regions near the SQ1-100 might be due to the higher concentration of defects (see Fig. 28), which allows the MoS_2 monolayer not exactly to conform to the lattice parameter of the Au

substrate. Finally, we can see that rotating the polarization by 90^o has no statistical difference in the measured strain and doping. Table 1 summarizes these findings.

Table 1 – Average values of the strain and doping for MoS_2 over Si and Au substrate. In the abbreviations, "sup." means supported.

Parameter	Si	SQ1x-100-sup	SQ1y-100-sup	SQ1x-50-sup	SQ1y-100-sup
ϵ (%)	-0.1	1.0	1.0	0.9	0.9
n (10^{13} cm^{-2})	0.1	0.3	0.3	0.3	0.2

Source: By the author

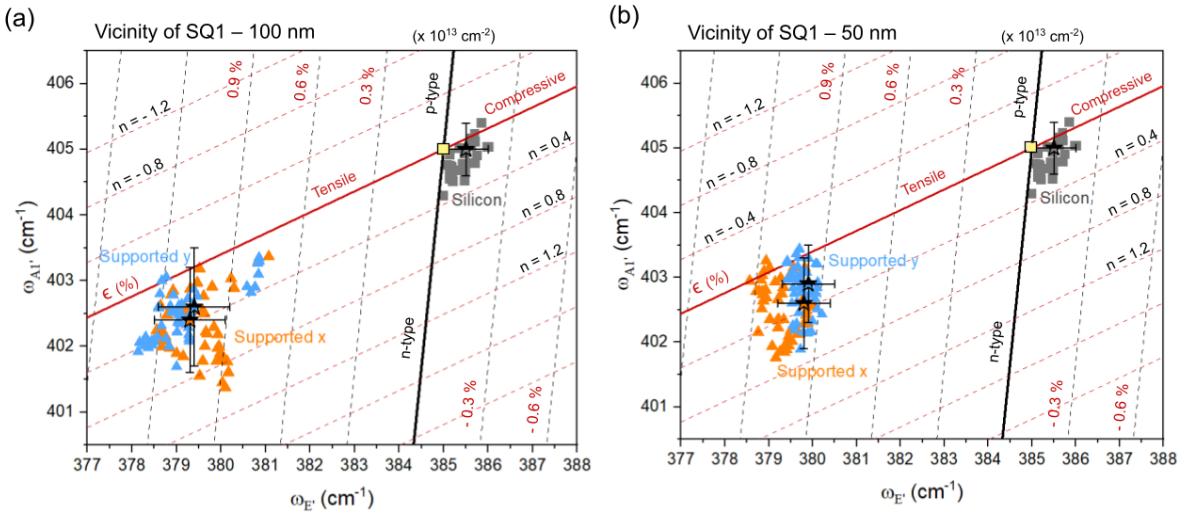

Figure 34 – (a,b) Correlative plot of the A_1' vs E' peak frequencies for the Si and Au substrates. Due to differences in morphology, the Au-supported regions have been separated in two cases: the vicinity of SQ1-100 (a) and SQ1-50 (b) structures. The average values of the clusters of points are also indicated. The yellow square represents the reference case of free-standing MoS_2.

Source: By the author.

The plot of the A_1' vs E' peak frequencies for the suspended regions is shown in Fig. 35. Here, the MoS_2 monolayer is subjected to a uniaxial strain in the out-of-plane direction, so the guidelines used in the Fig. 34 had to be modified (besides legibility, this is another reason why we had to separate the graphs for the supported and suspended regions). From the graphs, we note that the data is located in a region of the $\epsilon - n$ plane corresponding to a tensile uniaxial strain and n-type doping for both structures. The average strain and doping values for all the structures can be seen in Table 2. One can see that the electron concentration in the gratings is higher than in the supported regions, which is consistent with the fact that the MoS_2 monolayer has lesser contact with the gold surface, preventing the charge transfer mechanism. Additionally, a polarization

dependence in the strain and doping values for both structures can be perceived from the correlative plots. Previous works have demonstrated that the E'^{-} and E'^{+} modes, which originated from the splitting term in (5.6) caused by the shear deformation potential, do posses a polarization dependence. (118, 119) Nevertheless, we did not observe in our measurements a splitting of the E' mode, only an increase in the linewidth.

Table 2 – Average values of the strain and doping for MoS_2 over the suspended regions. In the abbreviations, "sus." means suspended.

Parameter	SQ1x-100-sus	SQ1y-100-sus	SQ1x-50-sus	SQ1y-50-sus
ϵ (%)	0.9	0.7	1.0	0.7
n (10^{13} cm^{-2})	1.0	0.7	0.5	0.3

Source: By the author

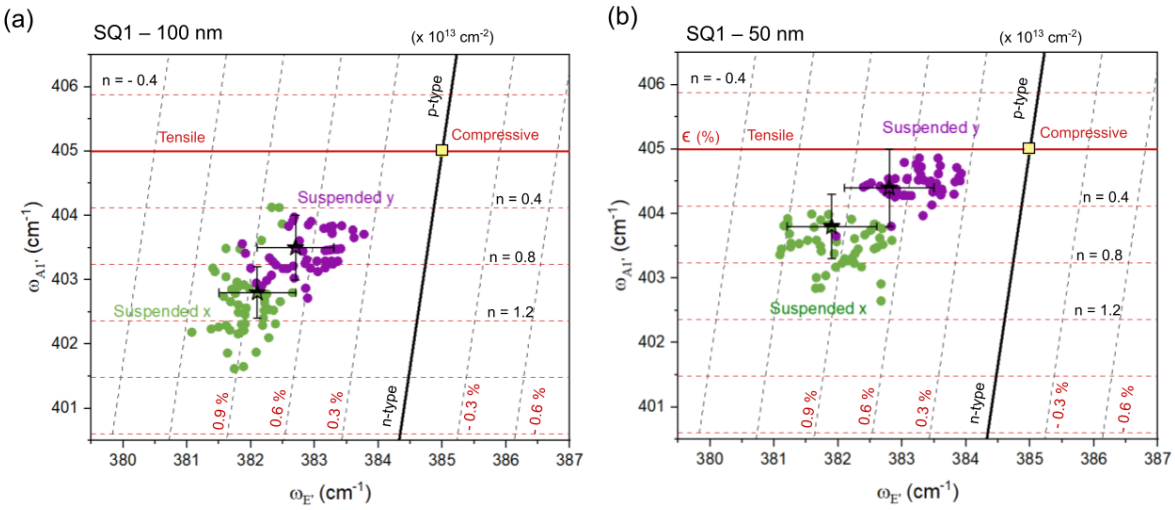

Figure 35 – (a,b) Correlative plot of the A_1' vs E' peak frequencies for the SQ1-100 (a) and SQ1-50 structures (b). The average values of the clusters of points are also indicated. The yellow square represents the reference case of free-standing MoS_2.

Source: By the author.

However, the linewidth color maps can be used to distinguish between the different kinds of strain, which are shown in Fig. 36 for the SQ1x-100 and SQ1x-50 structures. In the case of an applied uniaxial strain, the full width at half maximum (FWHM) of the E'^{-} mode is expected to increase due to the changes in the lattice symmetry. (112) In contrast, when the MoS_2 is subjected to a biaxial strain, the in-plane mode usually does not show an appreciable increase in the linewidth. (100). This contrasting behavior can be seen in the Fig. 36a,c. Also, the linewidth color maps for the A_1' mode are presented (see Fig. 36b,d) and they show a larger FWHM at the supported regions, probably because in those regions

the out-of-plane mode is influenced by the strain and doping levels. (100, 102) Since the SQ1y-100 and SQ1y-50 structures showed a similar behavior between the supported and suspended regions for the linewidth their FWHM color maps are presented in Appendix B.3.

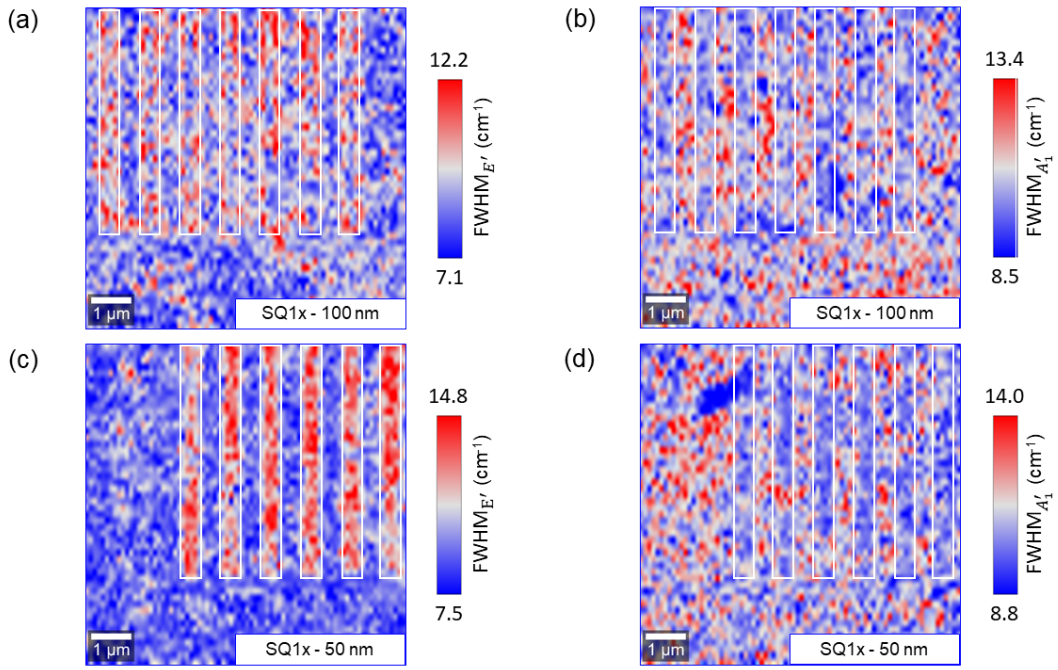

Figure 36 – (a-d) Linewidth of the E' and A_1' Raman modes for the SQ1x-100 (a,b) and SQ1x-50 (c,d) structures. The solid white rectangles serve only as a guide to represent the gold gratings.

Source: By the author

In regard to the polarization-dependent doping levels, the explanation might be due to plasmon-induced hot electron injection. Indeed, numerical simulations show a distinct behavior of the electric field distribution when the incident radiation is linearly polarized perpendicular or parallel to the slits. Figure 37 shows the calculated magnitude and z-component of electric field distributions for the SQ1x-100 and SQ1y-100 (for the simulation of the SQ1-50 structures see Appendix C). It is clear that the generation of plasmons (SPPs or LSPs) only occurs when the polarization of the electric field is perpendicular to the gratings. After generation, those plasmons decay via different mechanisms, such as interband transitions, Landau damping, or electron-electron scattering into so-called "hot carriers". Those hot carriers may have sufficient energy to overcome the binding force that keeps them inside the metal and effectively transfer charge into the adjacent material, such as a semiconductor (120), thus offering an explanation for the polarization dependence of the doping levels in the suspended regions.

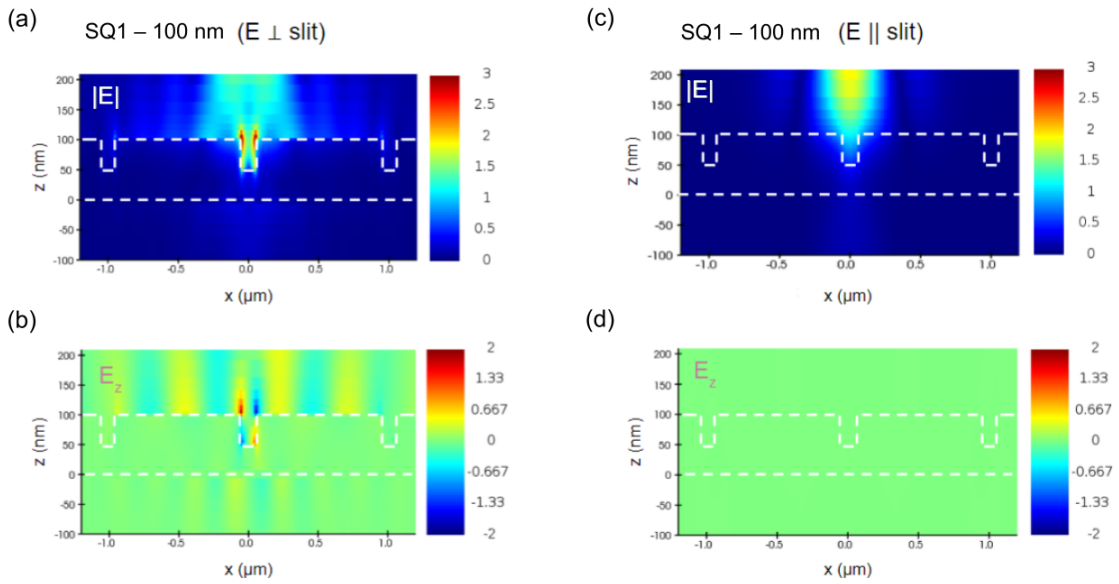

Figure 37 – (a-d) Magnitude and z-component of the electric field distribution for the SQ1x-100 (a,b) and SQ1y-100 (c,d) structures. The dashed white lines serve only as a guide to represent the gold gratings.

Source: By the author

5.3 PL measurements of exciton and trion states

To complete our analysis, photoluminescence measurements were performed to understand better the effect of the external perturbations discussed in the last section on the emission properties of the exciton and trion states of MoS_2 monolayer. Figure 38a shows a comparison of the PL spectra for the semiconductor film in the supported and suspended regions. One can see a quenching of the PL signal, which is commonly attributed to the charge transfer of the photogenerated carriers between MoS_2 and Au, leading to an effective exciton dissociation. (121). Figure 38b shows an energy band diagram for the MoS_2/Au system before and after contact, where the different work functions cause a band bending near the interface between the two materials. However, in our case, we observed a partial quenching, which implies that the charge transfer mechanism is not very efficient, corroborating the analysis performed in the Raman spectroscopy section. In addition, the suspended regions show a much higher signal and slight blue shift than the supported regions. The stronger intensity is explained by the absence of substrate-induced charge transfer, and the higher emission energy is due to a smaller strain compared to the Au-supported region since the strain is known to cause a redshift of the PL peak positions. (122)

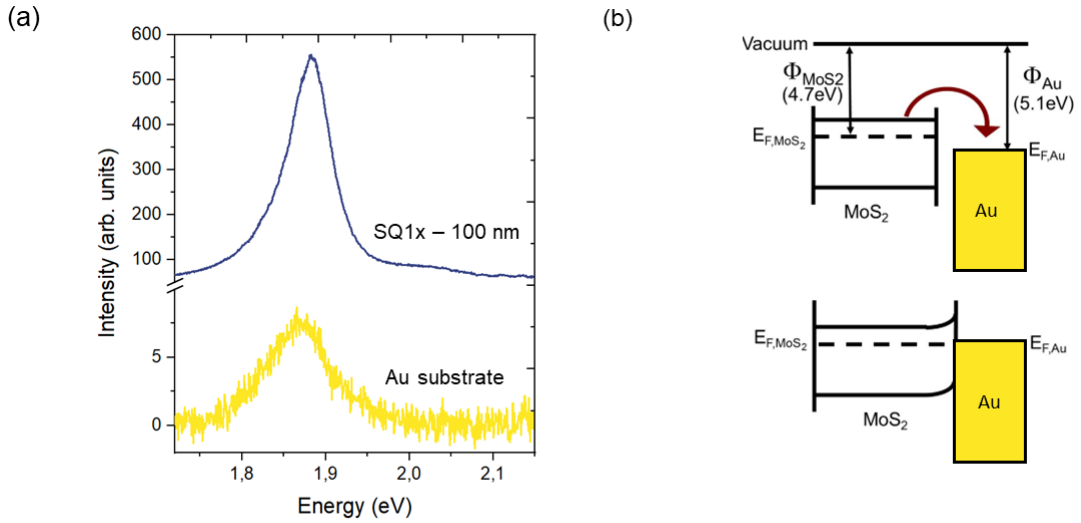

Figure 38 – (a) PL spectra of MoS_2 monolayer over the Au substrate and the SQ1x-100 grating. (b) Energy band diagram for MoS_2 and Au before (top) and after (bottom) contact between the two materials.

Source: (a) By the author; (b) Adapted from BHANU *et al.* (121)

Additional information can be acquired by looking at the normalized PL spectra for the MoS_2 deposited over different regions, namely Si or Au substrate and the metallic gratings, as shown in Fig. 39. Notably, three peaks, fitted using Lorentzian functions, can be identified. They correspond to the A and B excitons originating from the direct transitions between valence and conduction bands at the K point and the negative trion A^-. (46) Table 3 summarizes the calculated parameters from the normalized spectra. For MoS_2/Si, we can see a high ratio for the intensities of the trion and A exciton, consistent with n-type conductivity observed in the Raman measurements. In the case of MoS_2/Au, we can see a decrease in the trion population compared to the A exciton, accompanied by an extinction of the B exciton (although the signal-to-noise ratio is much smaller). This contrasts with the doping levels calculated using the Raman hyperspectral maps, where the MoS_2 over the Au-supported regions showed a pronounced n-type doping level. It has been suggested that Raman spectroscopy might not be particularly accurate for determining the structural and electronic properties of MoS_2 (123), so additional studies are necessary to establish which experimental technique is more adequate for characterizing 2D TMDs. In the suspended regions, the spectra become better defined, i.e., less noisy. We can clearly see that the ratio between the trion and A exciton is larger for the grating than the MoS_2 over the gold substrate due to a decrease in the direct contact between the MoS_2 and gold. Finally, this ratio is greater when the grating is perpendicular to the incident radiation (SQ1x-100 and SQ1x-50), which agrees with the doping levels calculated using the Raman maps and the numerical simulations for the electric field distribution. Interestingly, the trion population appears to be greater in the

SQ1x-100 in comparison to the SQ1x-50 despite the fact that the simulated electric field showed a very similar behavior in both structures. Since the SQ1x-50 gratings and its surrounding environment presented a large variety of defects, this could be an indication that the plasmon-induced hot electron injection might be less efficient in this structure.

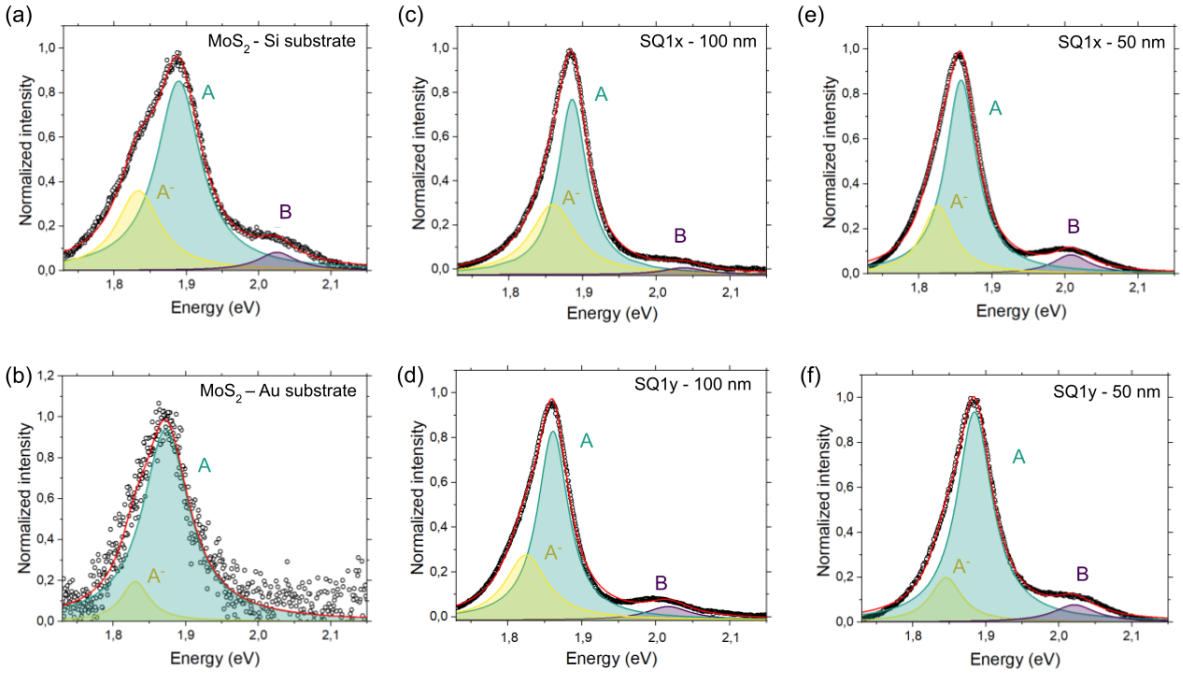

Figure 39 – (a-f) Normalized PL spectra for different regions in the sample.

Source: By the author

Table 3 – Calculated parameters from the normalized PL spectra for the MoS_2 monolayer deposited over different sample regions.

Parameter	Si	Au	SQ1x-100	SQ1y-100	SQ1x-50	SQ1y-50
A position (eV)	1.88	1.87	1.89	1.86	1.86	1.88
A^- position (eV)	1.83	1.83	1.86	1.82	1.83	1.85
B position (eV)	2.02	-	2.04	2.02	2.01	2.02
$I_{A^-}/I_{A^-} + I_A$ (%)	29.0	11.1	38.2	31.9	26.4	15.9
I_B/I_A (%)	8.6	-	6.0	10.5	11.8	10.0

Source: By the author

6 CONCLUSION AND PERSPECTIVES

In this dissertation, the morphological, vibrational, and optical properties of MoS_2 deposited over gold gratings were investigated. In the first part, we focused on the characterization of the morphology of the semiconductor film in different regions of the sample. We showed that the MoS_2 monolayer is subjected to large height deformations in the suspended areas. We also measured and discussed the defects observed in the AFM measurements.

In the second part, we investigated how vibrational properties of the MoS_2 are affected by the variations in substrate and morphology. Using Raman spectroscopy, we noted that the intensity ratio of the E' and A_1' modes strongly depends on the surrounding environment. More specifically, the amplitude of the A_1' mode strongly depends on the interaction between the Au and S atoms, where the mode displacement is restricted when MoS_2 is deposited over the gold substrate. Additionally, it was observed that the peak positions of the characteristic Raman modes of MoS_2 are susceptible to the induced external perturbations. By constructing a correlative plot of the A_1' vs. E' peak frequencies, we evaluated the contributions of strain, doping, and plasmonic effects on the frequency changes of those modes. We observed that the MoS_2 at the Au-supported regions is subjected to a biaxial tensile strain and an intriguing n-type doping level. The n-type conductivity probably means that the transferred MOCVD MoS_2 does not have good direct contact with the gold substrate. For the suspended regions, we noted that the electron concentrations were dependent on the polarization of the incident radiation, which was attributed to the plasmon-induced hot electron injection mechanism. We should also point out that, to our knowledge, this is the first work that simultaneously considers the effect of the biaxial and uniaxial strain in a strain-engineered TMD monolayer using Raman spectroscopy.

Finally, we studied the emission properties of the exciton and trion states of the MoS_2 monolayer. The partial quenching of the PL indicates that a charge transfer between MoS_2 and Au exists, but this mechanism is not very efficient because of the lack of a good MoS_2/Au contact. Moreover, a polarization-dependent trion to A exciton ratio further corroborates the existence of a plasmon-induced doping mechanism. It should be noted that some measurements conflicted with the results from the Raman spectroscopy, suggesting that complementary studies are necessary to establish which experimental technique is more adequate to investigate the electronic properties of the MoS_2 monolayer deposited over metallic gratings.

To conclude this work, we provide a few prospects for future studies on these two-dimensional transition-metal dichalcogenides and, more broadly, 2D materials. It is

clear that substrate-induced effects play an important role in the vibrational and optical properties of these materials. Control of the exciton dynamics in MoS_2 monolayers has been achieved by using a hyperbolic metamaterial (HMM) substrate (124) while the growth of MoS_2 using graphene as the substrate has been shown to produce a stable, strain-free MoS_2 layer and the realization of van der Waals heterostructure via epitaxy. (123) In addition, the possibility to modulate various properties of 2D materials based on strain engineering is a promising strategy that has attracted extensive research interests. In particular, a spatially modulated biaxial tensile strain has been shown to realize "artificial atoms" on a MoS_2 monolayer. (125) Another interesting prospect is the study of plasmon-enhanced nonlinear optical processes in 2D materials, where second-harmonic generation enhancement has been demonstrated using a hybrid plasmonic nanostructure. (126) One can see that many exciting routes on the rich physics of 2D materials exist and that further works will help advance this research field.

REFERENCES

1 LEMBKE, D.; KIS, A. Breakdown of high-performance monolayer MoS_2 transistors. **ACS Nano**, ACS Publications, v. 6, n. 11, p. 10070–10075, 2012.

2 BERTOLAZZI, S.; BRIVIO, J.; KIS, A. Stretching and breaking of ultrathin MoS_2. **ACS Nano**, ACS Publications, v. 5, n. 12, p. 9703–9709, 2011.

3 RADISAVLJEVIC, B. *et al.* Single-layer MoS_2 transistors. **Nature Nanotechnology**, Nature Publishing Group, v. 6, n. 3, p. 147–150, 2011.

4 WANG, X.-R.; SHI, Y.; ZHANG, R. Field-effect transistors based on two-dimensional materials for logic applications. **Chinese Physics B**, IOP Publishing, v. 22, n. 9, p. 098505, 2013.

5 BAO, W. *et al.* High mobility ambipolar MoS_2 field-effect transistors: Substrate and dielectric effects. **Applied Physics Letters**, American Institute of Physics, v. 102, n. 4, p. 042104, 2013.

6 FREY, G. *et al.* Optical-absorption spectra of inorganic fullerene-like MS_2 (M = Mo, W). **Physical Review B**, APS, v. 57, n. 11, p. 6666, 1998.

7 ISLAM, M. R. *et al.* Tuning the electrical property via defect engineering of single-layer MoS_2 by oxygen plasma. **Nanoscale**, Royal Society of Chemistry, v. 6, n. 17, p. 10033–10039, 2014.

8 MAK, K. F. *et al.* Atomically thin MoS_2: a new direct-gap semiconductor. **Physical Review Letters**, APS, v. 105, n. 13, p. 136805, 2010.

9 CHOUDHARY, N. *et al.* Two-dimensional lateral heterojunction through bandgap engineering of MoS_2 via oxygen plasma. **Journal of Physics**, IOP Publishing, v. 28, n. 36, p. 364002, 2016.

10 CASTELLANOS-GOMEZ, A. Why all the fuss about 2d semiconductors? **Nature Photonics**, Nature Publishing Group, v. 10, n. 4, p. 202–204, 2016.

11 LI, Z. *et al.* Active light control of the MoS_2 monolayer exciton binding energy. **ACS Nano**, ACS Publications, v. 9, n. 10, p. 10158–10164, 2015.

12 TONNDORF, P. *et al.* Photoluminescence emission and raman response of monolayer MoS_2, $MoSe_2$, and WSe_2. **Optics Express**, Optica Publishing Group, v. 21, n. 4, p. 4908–4916, 2013.

13 AMANI, M. *et al.* Near-unity photoluminescence quantum yield in MoS_2. **Science**, American Association for the Advancement of Science, v. 350, n. 6264, p. 1065–1068, 2015.

14 KONSTANTATOS, G. *et al.* Hybrid graphene–quantum dot phototransistors with ultrahigh gain. **Nature Nanotechnology**, Nature Publishing Group, v. 7, n. 6, p. 363–368, 2012.

15 FERNÁNDEZ-GARCÍA, R. *et al.* Design considerations for near-field enhancement in optical antennas. **Contemporary Physics**, Taylor & Francis, v. 55, n. 1, p. 1–11, 2014.

16 SRIRAM, P. *et al.* Hybridizing strong quadrupole gap plasmons using optimized nanoantennas with bilayer MoS_2 for excellent photo-electrochemical hydrogen evolution. **Advanced Energy Materials**, Wiley Online Library, v. 8, n. 29, p. 1801184, 2018.

17 PARK, Q.-H. Optical antennas and plasmonics. **Contemporary Physics**, Taylor & Francis, v. 50, n. 2, p. 407–423, 2009.

18 BERINI, P.; LEON, I. D. Surface plasmon–polariton amplifiers and lasers. **Nature Photonics**, Nature Publishing Group, v. 6, n. 1, p. 16–24, 2012.

19 RODGERS, P. **Nanoscience and technology**: a collection of reviews from nature journals. Singapore: World Scientific, 2009.

20 HESS, O. *et al.* Active nanoplasmonic metamaterials. **Nature Materials**, Nature Publishing Group, v. 11, n. 7, p. 573–584, 2012.

21 VALENTI, M. *et al.* The role of size and dimerization of decorating plasmonic silver nanoparticles on the photoelectrochemical solar water splitting performance of $BiVO_4$ photoanodes. **ChemNanoMat**, Wiley Online Library, v. 2, n. 7, p. 739–747, 2016.

22 LINIC, S.; CHRISTOPHER, P.; INGRAM, D. B. Plasmonic-metal nanostructures for efficient conversion of solar to chemical energy. **Nature Materials**, Nature Publishing Group, v. 10, n. 12, p. 911–921, 2011.

23 CHEN, M. *et al.* Photocurrent enhancement of hgte quantum dot photodiodes by plasmonic gold nanorod structures. **ACS Nano**, ACS Publications, v. 8, n. 8, p. 8208–8216, 2014.

24 HILL, M. T. *et al.* Lasing in metal-insulator-metal sub-wavelength plasmonic waveguides. **Optics Express**, Optical Society of America, v. 17, n. 13, p. 11107–11112, 2009.

25 KADANTSEV, E. S.; HAWRYLAK, P. Electronic structure of a single MoS_2 monolayer. **Solid State Communications**, Elsevier, v. 152, n. 10, p. 909–913, 2012.

26 LÓPEZ, R. R. R. *et al.* **Optical properties of transition metal dichalcogenides on GaAs**. 2018. 74f. Dissertation (Master in Science) - Instituto de Ciências Exatas, Universidade Federal de Minas Gerais, Belo Horizonte, 2018.

27 LV, R. *et al.* Transition metal dichalcogenides and beyond: synthesis, properties, and applications of single-and few-layer nanosheets. **Accounts of Chemical Research**, ACS Publications, v. 48, n. 1, p. 56–64, 2015.

28 WAKABAYASHI, N.; SMITH, H.; NICKLOW, R. Lattice dynamics of hexagonal MoS_2 studied by neutron scattering. **Physical Review B**, APS, v. 12, n. 2, p. 659, 1975.

29 SANDOVAL, S. J. *et al.* Raman study and lattice dynamics of single molecular layers of MoS_2. **Physical Review B**, APS, v. 44, n. 8, p. 3955, 1991.

30 PY, M.; HAERING, R. Structural destabilization induced by lithium intercalation in MoS_2 and related compounds. **Canadian Journal of Physics**, NRC Research Press Ottawa, Canada, v. 61, n. 1, p. 76–84, 1983.

31 VOIRY, D. *et al.* Conducting MoS_2 nanosheets as catalysts for hydrogen evolution reaction. **Nano Letters**, ACS Publications, v. 13, n. 12, p. 6222–6227, 2013.

32 WANG, H. *et al.* Electrochemical tuning of MoS_2 nanoparticles on three-dimensional substrate for efficient hydrogen evolution. **ACS Nano**, ACS Publications, v. 8, n. 5, p. 4940–4947, 2014.

33 GRUNDMANN, M. **Physics of semiconductors**. Berlin: Springer, 2010. v. 11.

34 SPLENDIANI, A. *et al.* Emerging photoluminescence in monolayer MoS_2. **Nano Letters**, ACS Publications, v. 10, n. 4, p. 1271–1275, 2010.

35 WINKLER, R. **Spin-orbit coupling effects in two-dimensional electron and hole systems**. Berlin: Springer, 2003. v. 191.

36 XIAO, D. *et al.* Coupled spin and valley physics in monolayers of MoS_2 and other group-VI dichalcogenides. **Physical Review Letters**, APS, v. 108, n. 19, p. 196802, 2012.

37 CHERNIKOV, A. *et al.* Exciton binding energy and nonhydrogenic rydberg series in monolayer WS_2. **Physical Review Letters**, APS, v. 113, n. 7, p. 076802, 2014.

38 HSU, W.-T. *et al.* Dielectric impact on exciton binding energy and quasiparticle bandgap in monolayer WS_2 and WSe_2. **2D Materials**, IOP Publishing, v. 6, n. 2, p. 025028, 2019.

39 UGEDA, M. M. *et al.* Giant bandgap renormalization and excitonic effects in a monolayer transition metal dichalcogenide semiconductor. **Nature Materials**, Nature Publishing Group, v. 13, n. 12, p. 1091–1095, 2014.

40 QIU, D. Y.; FELIPE, H.; LOUIE, S. G. Optical spectrum of MoS_2: many-body effects and diversity of exciton states. **Physical Review Letters**, APS, v. 111, n. 21, p. 216805, 2013.

41 ZHANG, X.-X. *et al.* Magnetic brightening and control of dark excitons in monolayer WSe_2. **Nature Nanotechnology**, Nature Publishing Group, v. 12, n. 9, p. 883–888, 2017.

42 MOLAS, M. R. *et al.* Brightening of dark excitons in monolayers of semiconducting transition metal dichalcogenides. **2D Materials**, IOP Publishing, v. 4, n. 2, p. 021003, 2017.

43 WANG, G. *et al.* In-plane propagation of light in transition metal dichalcogenide monolayers: optical selection rules. **Physical Review Letters**, APS, v. 119, n. 4, p. 047401, 2017.

44 WANG, G. *et al.* Colloquium: excitons in atomically thin transition metal dichalcogenides. **Reviews of Modern Physics**, APS, v. 90, n. 2, p. 021001, 2018.

45 ROSS, J. S. *et al.* Electrical control of neutral and charged excitons in a monolayer semiconductor. **Nature Communications**, Nature Publishing Group, v. 4, n. 1, p. 1–6, 2013.

46 MAK, K. F. *et al.* Tightly bound trions in monolayer MoS_2. **Nature Materials**, Nature Publishing Group, v. 12, n. 3, p. 207–211, 2013.

47 LI, Z. *et al.* Revealing the biexciton and trion-exciton complexes in bn encapsulated WSe_2. **Nature Communications**, Nature Publishing Group, v. 9, n. 1, p. 1–7, 2018.

48 YOU, Y. *et al.* Observation of biexcitons in monolayer WSe_2. **Nature Physics**, Nature Publishing Group, v. 11, n. 6, p. 477–481, 2015.

49 BARBONE, M. *et al.* Charge-tuneable biexciton complexes in monolayer WSe_2. **Nature Communications**, Nature Publishing Group, v. 9, n. 1, p. 1–6, 2018.

50 PAUR, M. *et al.* Electroluminescence from multi-particle exciton complexes in transition metal dichalcogenide semiconductors. **Nature Communications**, Nature Publishing Group, v. 10, n. 1, p. 1–7, 2019.

51 HE, Y.-M. *et al.* Single quantum emitters in monolayer semiconductors. **Nature Nanotechnology**, Nature Publishing Group, v. 10, n. 6, p. 497–502, 2015.

52 SRIVASTAVA, A. *et al.* Optically active quantum dots in monolayer WSe_2. **Nature Nanotechnology**, Nature Publishing Group, v. 10, n. 6, p. 491–496, 2015.

53 MOLINA-SANCHEZ, A.; WIRTZ, L. Phonons in single-layer and few-layer MoS_2 and WS_2. **Physical Review B**, APS, v. 84, n. 15, p. 155413, 2011.

54 LEE, C. *et al.* Anomalous lattice vibrations of single-and few-layer MoS_2. **ACS Nano**, ACS Publications, v. 4, n. 5, p. 2695–2700, 2010.

55 PU, J. *et al.* Highly flexible MoS_2 thin-film transistors with ion gel dielectrics. **Nano Letters**, ACS Publications, v. 12, n. 8, p. 4013–4017, 2012.

56 CHANG, H.-Y. *et al.* High-performance, highly bendable MoS_2 transistors with high-k dielectrics for flexible low-power systems. **ACS Nano**, ACS Publications, v. 7, n. 6, p. 5446–5452, 2013.

57 ZANGWILL, A. **Modern electrodynamics**. Cambridge: Cambridge University Press, 2013.

58 MCEUEN, P.; KITTEL, C. **Introduction to solid state physics**. Boston: Wiley, 2005.

59 MAIER, S. **Plasmonics**: fundamentals and applications. Boston: Springer, 2007.

60 DRESSEL, M.; GRÜNER, G. **Electrodynamics of solids**: optical properties of electrons in matter. Cambridge: Cambridge University Press, 2002.

61 WATERS, K. R.; MOBLEY, J.; MILLER, J. G. Causality-imposed (Kramers-Kronig) relationships between attenuation and dispersion. **IEEE Transactions on Ultrasonics, Ferroelectrics, and Frequency Control**, IEEE, v. 52, n. 5, p. 822–823, 2005.

62 JACKSON, J. D. **Classical electrodynamics**. New York: John Wiley, 1999.

63 BASOV, D. N. *et al.* Polariton panorama. **Nanophotonics**, De Gruyter, v. 10, n. 1, p. 549–577, 2021.

64 BASOV, D.; FOGLER, M.; ABAJO, F. G. Polaritons in van der waals materials. **Science**, American Association for the Advancement of Science, v. 354, n. 6309, p. aag1992, 2016.

65 LOW, T. *et al.* Polaritons in layered two-dimensional materials. **Nature Materials**, Nature Publishing Group UK London, v. 16, n. 2, p. 182–194, 2017.

66 ZHANG, J.; ZHANG, L.; XU, W. Surface plasmon polaritons: physics and applications. **Journal of Physics D**, IOP Publishing, v. 45, n. 11, p. 113001, 2012.

67 BARNES, W. L.; DEREUX, A.; EBBESEN, T. W. Surface plasmon subwavelength optics. **Nature**, Nature Publishing Group UK London, v. 424, n. 6950, p. 824–830, 2003.

68 HERRERA, L. J. M. *et al.* Determination of plasma frequency, damping constant, and size distribution from the complex dielectric function of noble metal nanoparticles. **Journal of Applied Physics**, AIP Publishing LLC, v. 116, n. 23, p. 233105, 2014.

69 LAW, S.; LIU, R.; WASSERMAN, D. Doped semiconductors with band-edge plasma frequencies. **Journal of Vacuum Science & Technology B**, American Vacuum Society, v. 32, n. 5, p. 052601, 2014.

70 OTTO, A. Excitation of nonradiative surface plasma waves in silver by the method of frustrated total reflection. **Zeitschrift für Physik A**, Springer, v. 216, n. 4, p. 398–410, 1968.

71 ZAYATS, A. V.; SMOLYANINOV, I. I.; MARADUDIN, A. A. Nano-optics of surface plasmon polaritons. **Physics Reports**, Elsevier, v. 408, n. 3-4, p. 131–314, 2005.

72 PARIA, D.; ZHANG, C.; BARMAN, I. Towards rational design and optimization of near-field enhancement and spectral tunability of hybrid core-shell plasmonic nanoprobes. **Scientific Reports**, Springer, v. 9, n. 1, p. 1–9, 2019.

73 NAIK, G. V.; SHALAEV, V. M.; BOLTASSEVA, A. Alternative plasmonic materials: beyond gold and silver. **Advanced Materials**, Wiley Online Library, v. 25, n. 24, p. 3264–3294, 2013.

74 ZHANG, J. X.; HOSHINO, K. Fundamentals of nano/microfabrication and scale effect. **Molecular Sensors and Nanodevices**, Academic Press, p. 43–111, 2019.

75 WATSON, A. J. *et al.* Transfer of large-scale two-dimensional semiconductors: challenges and developments. **2D Materials**, IOP Publishing, v. 8, n. 3, p. 032001, 2021.

76 HE, T. *et al.* Synthesis of large-area uniform MoS_2 films by substrate-moving atmospheric pressure chemical vapor deposition: from monolayer to multilayer. **2D Materials**, IOP Publishing, v. 6, n. 2, p. 025030, 2019.

77 KANG, K. *et al.* Layer-by-layer assembly of two-dimensional materials into wafer-scale heterostructures. **Nature**, Nature Publishing Group UK London, v. 550, n. 7675, p. 229–233, 2017.

78 NAJMAEI, S. *et al.* Vapour phase growth and grain boundary structure of molybdenum disulphide atomic layers. **Nature Materials**, Nature Publishing Group UK London, v. 12, n. 8, p. 754–759, 2013.

79 CUN, H. *et al.* Wafer-scale mocvd growth of monolayer MoS_2 on sapphire and SiO_2. **Nano Research**, Springer, v. 12, p. 2646–2652, 2019.

80 KIM, H. *et al.* Suppressing nucleation in metal-organic chemical vapor deposition of MoS_2 monolayers by alkali metal halides. **Nano Letters**, ACS Publications, v. 17, n. 8, p. 5056–5063, 2017.

81 MAREGA, G. M. *et al.* Low-power artificial neural network perceptron based on monolayer MoS_2. **ACS Nano**, ACS Publications, v. 16, n. 3, p. 3684–3694, 2022.

82 BARBOZA, A. P. M. **Propriedades eletromecânicas de nanoestruturas por Microscopia de Varredura por Sonda**. Tese (Doutorado em Filosofia) - Instituto de Ciências Exatas, Universidade Federal de Minas Gerais, Belo Horizonte, 2012.

83 CORNEY, A. **Atomic and laser spectroscopy**. Oxford: Oxford University Press, 2006.

84 KLINGSHIRN, C. F. **Semiconductor optics**. Boston: Springer, 2012.

85 CARDONA, M.; PETER, Y. Y. **Fundamentals of semiconductors**. Berlin: Springer, 2005. v. 619.

86 KASAP, S. O.; CAPPER, P. **Springer handbook of electronic and photonic materials**. Boston: Springer, 2006. v. 11.

87 ZHANG, C. *et al.* Absorption of light by excitons and trions in monolayers of metal dichalcogenide MoS_2: experiments and theory. **Physical Review B**, APS, v. 89, n. 20, p. 205436, 2014.

88 SINGH, R. CV Raman and the discovery of the Raman effect. **Physics in Perspective**, Springer, v. 4, p. 399–420, 2002.

89 WEBER, W. H.; MERLIN, R. **Raman scattering in materials science**. Boston: Springer, 2000. v. 42.

90 CARDONA, M. **Light scattering in solids 1**. Berlin: Springer, 1975.

91 YEE, K. Numerical solution of initial boundary value problems involving maxwell's equations in isotropic media. **IEEE Transactions on Antennas and Propagation**, IEEE, v. 14, n. 3, p. 302–307, 1966.

92 INAN, U. S.; MARSHALL, R. A. **Numerical electromagnetics**: the FDTD method. Cambridge: Cambridge University Press, 2011.

93 YAO, N.; WANG, Z. L. **Handbook of microscopy for nanotechnology**. Boston: Springer, 2005.

94 LEE, H. *et al.* All-optical control of high-purity trions in nanoscale waveguide. **Nature Communications**, Nature Publishing Group UK London, v. 14, n. 1, p. 1891, 2023.

95 LEE, H. *et al.* Drift-dominant exciton funneling and trion conversion in 2d semiconductors on the nanogap. **Science Advances**, American Association for the Advancement of Science, v. 8, n. 5, p. eabm5236, 2022.

96 HUANG, X. *et al.* Raman spectra evidence for the covalent-like quasi-bonding between exfoliated MoS_2 and Au films. **Science China Information Sciences**, Springer, v. 64, p. 1–9, 2021.

97 GONG, C. *et al.* Metal contacts on physical vapor deposited monolayer MoS_2. **ACS Nano**, ACS Publications, v. 7, n. 12, p. 11350–11357, 2013.

98 SOARES, J. R. **Group theory and Raman spectroscopy applied to the study of vibrational properties of two-dimensional materials**. Thesis (Doctor of Philosophy) - Instituto de Ciências Exatas, Universidade Federal de Minas Gerais, Belo Horizonte, 2014.

99 CARVALHO, B. R. *et al.* Intervalley scattering by acoustic phonons in two-dimensional MoS_2 revealed by double-resonance raman spectroscopy. **Nature Communications**, Nature Publishing Group UK London, v. 8, n. 1, p. 14670, 2017.

100 VELICKY, M. *et al.* Strain and charge doping fingerprints of the strong interaction between monolayer MoS_2 and gold. **The Journal of Physical Chemistry Letters**, ACS Publications, v. 11, n. 15, p. 6112–6118, 2020.

101 VELICKY, M. *et al.* Mechanism of gold-assisted exfoliation of centimeter-sized transition-metal dichalcogenide monolayers. **ACS Nano**, ACS Publications, v. 12, n. 10, p. 10463–10472, 2018.

102 PANASCI, S. E. *et al.* Strain, doping, and electronic transport of large area monolayer MoS_2 exfoliated on gold and transferred to an insulating substrate. **ACS Applied Materials & Interfaces**, ACS Publications, v. 13, n. 26, p. 31248–31259, 2021.

103 SUN, Y. *et al.* Probing local strain at MX_2–metal boundaries with surface plasmon-enhanced raman scattering. **Nano Letters**, ACS Publications, v. 14, n. 9, p. 5329–5334, 2014.

104 LEE, J. E. *et al.* Optical separation of mechanical strain from charge doping in graphene. **Nature Communications**, Nature Publishing Group UK London, v. 3, n. 1, p. 1024, 2012.

105 MOHIUDDIN, T. *et al.* Uniaxial strain in graphene by Raman spectroscopy: G peak splitting, Grüneisen parameters, and sample orientation. **Physical Review B**, APS, v. 79, n. 20, p. 205433, 2009.

106 ARMANO, A. *et al.* Monolayer graphene doping and strain dynamics induced by thermal treatments in controlled atmosphere. **Carbon**, Elsevier, v. 127, p. 270–279, 2018.

107 CHAE, W. H. *et al.* Substrate-induced strain and charge doping in CVD-grown monolayer MoS_2. **Applied Physics Letters**, AIP Publishing LLC, v. 111, n. 14, p. 143106, 2017.

108 THOMSEN, C.; REICH, S.; ORDEJON, P. Ab initio determination of the phonon deformation potentials of graphene. **Physical Review B**, APS, v. 65, n. 7, p. 073403, 2002.

109 CHAE, W. H. *et al.* Substrate-induced strain and charge doping in cvd-grown monolayer MoS_2. **Applied Physics Letters**, AIP Publishing LLC, v. 111, n. 14, p. 143106, 2017.

110 LLOYD, D. *et al.* Band gap engineering with ultralarge biaxial strains in suspended monolayer MoS_2. **Nano Letters**, ACS Publications, v. 16, n. 9, p. 5836–5841, 2016.

111 ZHU, C. *et al.* Strain tuning of optical emission energy and polarization in monolayer and bilayer MoS_2. **Physical Review B**, APS, v. 88, n. 12, p. 121301, 2013.

112 CONLEY, H. J. *et al.* Bandgap engineering of strained monolayer and bilayer MoS_2. **Nano Letters**, ACS Publications, v. 13, n. 8, p. 3626–3630, 2013.

113 COOPER, R. C. *et al.* Nonlinear elastic behavior of two-dimensional molybdenum disulfide. **Physical Review B**, APS, v. 87, n. 3, p. 035423, 2013.

114 DENG, S. *et al.* Adhesion energy of MoS_2 thin films on silicon-based substrates determined via the attributes of a single MoS_2 wrinkle. **ACS Applied Materials & Interfaces**, ACS Publications, v. 9, n. 8, p. 7812–7818, 2017.

115 SINGH, A.; SINGH, A. K. Origin of n-type conductivity of monolayer MoS_2. **Physical Review B**, APS, v. 99, n. 12, p. 121201, 2019.

116 BHANU, U. *et al.* Photoluminescence quenching in gold-MoS_2 hybrid nanoflakes. **Scientific Reports**, Nature Publishing Group UK London, v. 4, n. 1, p. 5575, 2014.

117 POLLMANN, E. *et al.* Large-area, two-dimensional MoS_2 exfoliated on gold: Direct experimental access to the metal–semiconductor interface. **ACS Omega**, ACS Publications, v. 6, n. 24, p. 15929–15939, 2021.

118 LEE, J.-U. *et al.* Strain-shear coupling in bilayer MoS_2. **Nature Communications**, Nature Publishing Group UK London, v. 8, n. 1, p. 1370, 2017.

119 WANG, Y. *et al.* Strain-induced direct–indirect bandgap transition and phonon modulation in monolayer WS_2. **Nano Research**, Springer, v. 8, p. 2562–2572, 2015.

120 KHURGIN, J. B. Fundamental limits of hot carrier injection from metal in nanoplasmonics. **Nanophotonics**, De Gruyter, v. 9, n. 2, p. 453–471, 2020.

121 BHANU, U. *et al.* Photoluminescence quenching in gold-MoS_2 hybrid nanoflakes. **Scientific Reports**, Nature Publishing Group UK London, v. 4, n. 1, p. 5575, 2014.

122 CASTELLANOS-GOMEZ, A. *et al.* Local strain engineering in atomically thin mos2. **Nano Letters**, ACS Publications, v. 13, n. 11, p. 5361–5366, 2013.

123 SITEK, J. *et al.* Substrate-induced variances in morphological and structural properties of MoS_2 grown by chemical vapor deposition on epitaxial graphene and SiO_2. **ACS Applied Materials & Interfaces**, ACS Publications, v. 12, n. 40, p. 45101–45110, 2020.

124 LEE, K. J. *et al.* Exciton dynamics in two-dimensional MoS_2 on a hyperbolic metamaterial-based nanophotonic platform. **Physical Review B**, APS, v. 101, n. 4, p. 041405, 2020.

125 LI, H. *et al.* Optoelectronic crystal of artificial atoms in strain-textured molybdenum disulphide. **Nature Communications**, Nature Publishing Group UK London, v. 6, n. 1, p. 7381, 2015.

126 WANG, Z. *et al.* Selectively plasmon-enhanced second-harmonic generation from monolayer tungsten diselenide on flexible substrates. **ACS Nano**, ACS Publications, v. 12, n. 2, p. 1859–1867, 2018.

127 DIEING, T.; HOLLRICHER, O.; TOPORSKI, J. **Confocal raman microscopy**. Berlin: Springer, 2011. v. 158.

128 JONKMAN, J. *et al.* Tutorial: guidance for quantitative confocal microscopy. **Nature Protocols**, Nature Publishing Group UK London, v. 15, n. 5, p. 1585–1611, 2020.

129 AERT, S. V.; DYCK, D. V.; DEKKER, A. J. den. Resolution of coherent and incoherent imaging systems reconsidered-classical criteria and a statistical alternative. **Optics Express**, Optica Publishing Group, v. 14, n. 9, p. 3830–3839, 2006.

APPENDIX

APPENDIX A – CONFOCAL MICROSCOPY

This appendix presents a basic overview of the confocal microscopy technique, but the interested reader is encouraged to see Ref. (127, 128) for more details. Conventional optical microscopy is a powerful tool for studying the physical and chemical properties of various samples. However, due to the superposition of the features from the focal plane and scattered light from outside of the focus, regular widefield microscopes possess low-depth image resolution. In contrast, confocal microscopes are able to suppress light from above or below the focal point, rendering them higher image contrast. To achieve this, confocal imaging techniques rely on point-to-point image formation, where a point-like source (a laser) is used for illumination and the light is detected through a small pinhole in front of the detector. An image of the sample is obtained by scanning the sample with the laser point by point and line by line. Figure 40 shows a schematic of the essential components common to all confocal microscopes. Besides the enhanced depth contrast, confocal microscopy presents two other advantages. First, by changing the focus to create a 3D dataset, a reconstruction of the entire sample volume can be made. Moreover, the appropriate selection of the pinhole diameter allows an increase in the lateral resolution by a factor of $\sqrt{2}$. (127) However, since a significant part of the light from the sample is blocked by the pinhole, long exposures and highly sensitive detectors are often required.

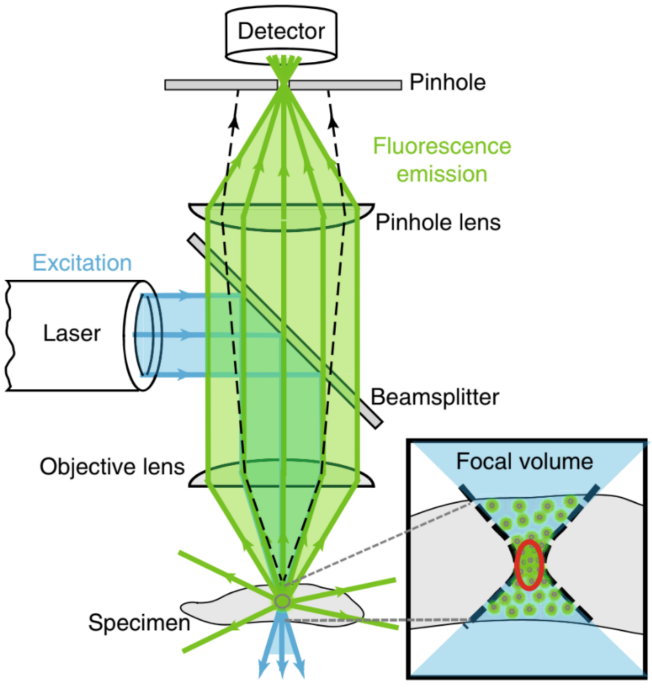

Figure 40 – Principal setup of a confocal microscope.

Source: Adapted from JONKMAN *et al.* (128)

One way to evaluate the response of the optical system to the specimen is by using the intensity point spread function (PSF). It describes the system response in real space to the three-dimensional diffraction pattern of light emitted from a point source in the specimen and transmitted to the image plane through the numerical aperture (NA) objective. Although the PSF is best suitable for point-to-point image formation techniques such as confocal microscopy, it can be used for conventional widefield microscopes, since the specimens can be considered as a superposition of an infinite number of objects having dimensions below the resolution of the system. To facilitate the explanation, we can consider only the intensity distribution of the point spread function in the plane of focus, which is described by the Airy pattern (named after George Biddell Airy). Using the Rayleigh criterion (127), one may define resolution as the minimum separation distance at which the two objects PSFs can be sufficiently distinguished (there is still some ambiguity in the meaning of "sufficiently distinguished" (see Ref. (129))). As a consequence, the width of the PSF becomes an important property to describe the resolution of an optical system. Figure 41 shows the full-width at half maximum (FWHM) of the point spread function for a conventional and a confocal microscope, solidifying the claim of enhanced image contrast for the latter case.

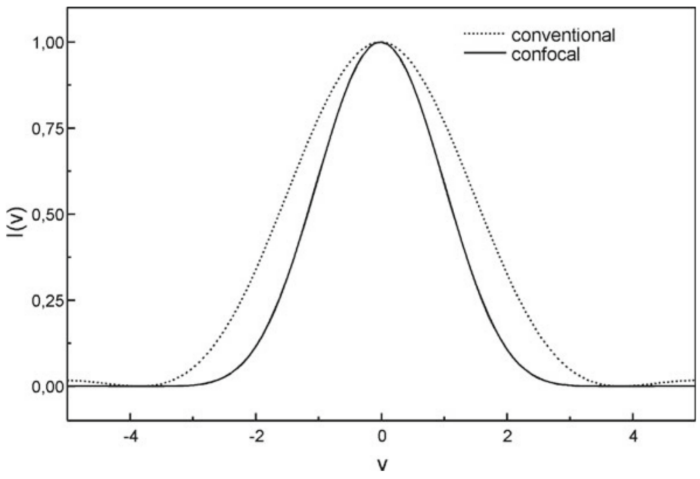

Figure 41 – Comparison of the PSFs for conventional and confocal microscopes.

Source: Adapted from DIEING; HOLLRICHER; TOPORSKI. (127)

APPENDIX B – RAMAN HYPERSPECTRAL MAPPING

B.1 Peak positions

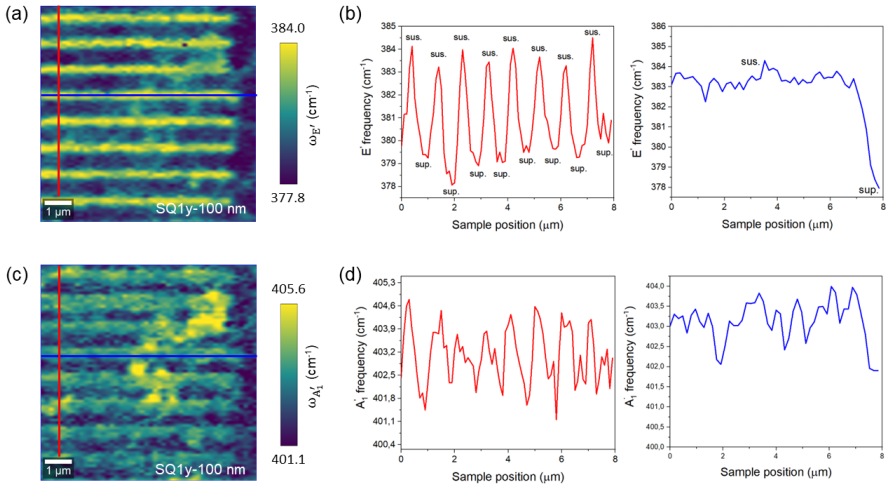

Figure 42 – (a) Color map of the peak position for the E' mode. (b) Peak position as a function of the position along two lines in (a). (c) Color map of the peak position for the A_1' mode. (d) Peak position as a function of the position along two lines in (c). Both maps correspond to the SQ1y-100 structure.

Source: By the author

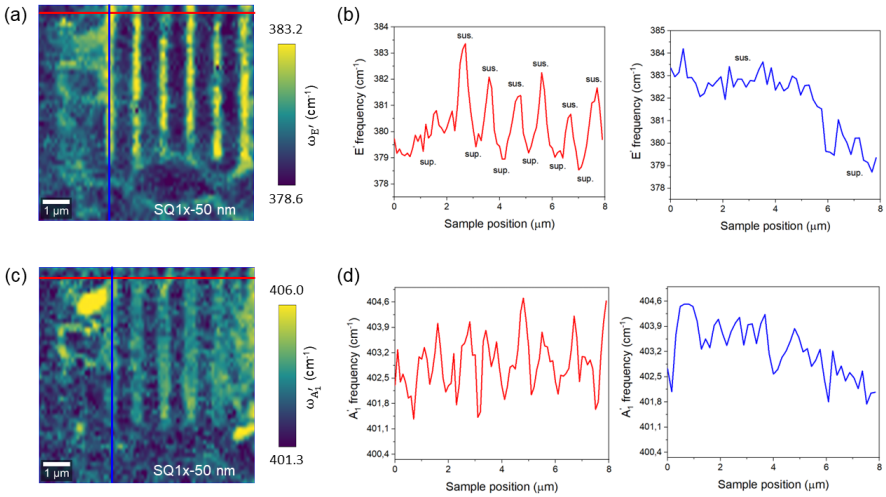

Figure 43 – (a) Color map of the peak position for the E' mode. (b) Peak position as a function of the position along two lines in (a). (c) Color map of the peak position for the A_1' mode. (d) Peak position as a function of the position along two lines in (c). Both maps correspond to the SQ1x-50 structure.

Source: By the author

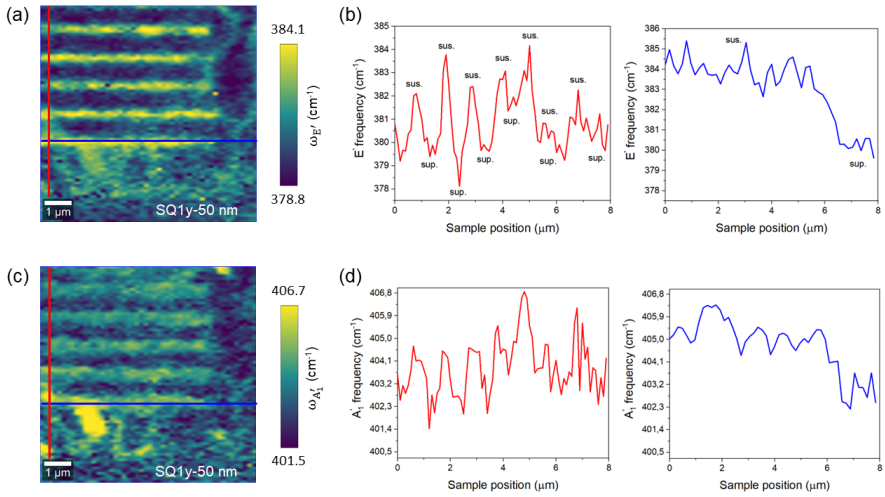

Figure 44 – (a) Color map of the peak position for the E' mode. (b) Peak position as a function of the position along two lines in (a). (c) Color map of the peak position for the A_1' mode. (d) Peak position as a function of the position along two lines in (c). Both maps correspond to the SQ1y-50 structure.

Source: By the author

B.2 Frequency difference

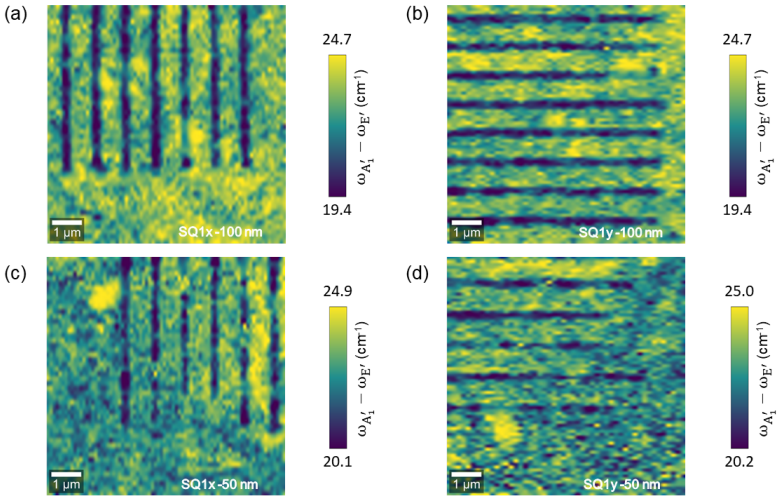

Figure 45 – Frequency difference between the peak positions of the A_1' and E' modes for all structures.

Source: By the author

B.3 Linewidth

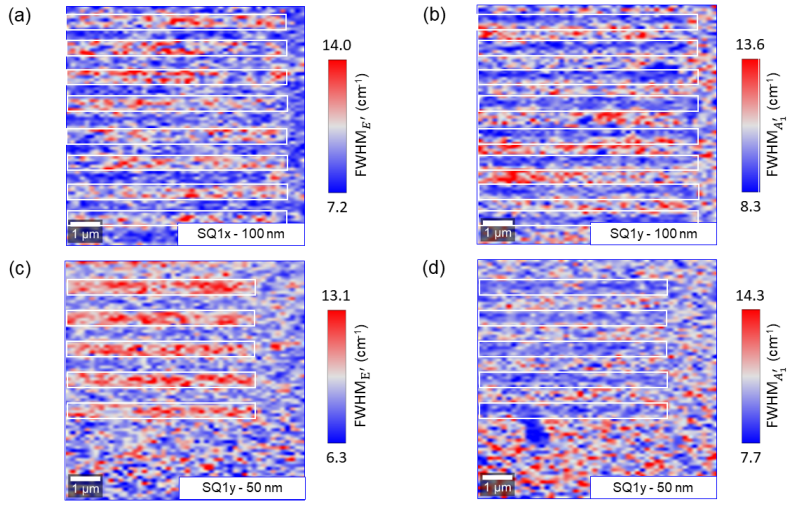

Figure 46 – (a-d) Linewidth of the E' and A_1' Raman modes for the SQ1y-100 (a,b) and SQ1y-50 (c,d) structures. The solid white rectangles serve only as a guide to represent the gold gratings.

Source: By the author

APPENDIX C – ELECTRIC FIELD DISTRIBUTION

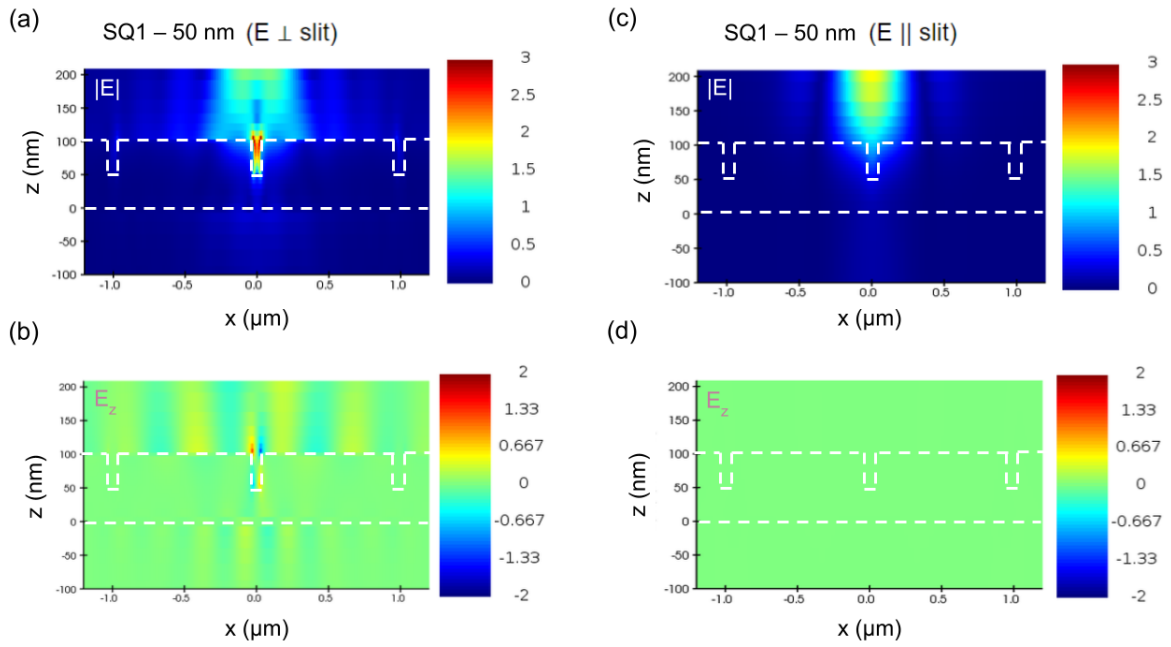

Figure 47 – (a-d) Magnitude and z-component of the electric field distribution for the SQ1x-50 (a,b) and SQ1y-50 (c,d). The dashed white lines serve only as a guide to represent the gold gratings.

Source: By the author

APPENDIX D – BIBLIOGRAPHICAL PRODUCTION

Work presented in congress

LEMES, M. F. S.; MAREGA JR, E. Plasmon-enhanced light-matter interaction in MoS_2 monolayer by gold nanostructures. In: XX BRAZIL MRS MEETING. Foz do Iguaçu. Paraná, 2022.

Work accepted in congress

LEMES. M. F. S.; MAREGA, G. M.; CHIESA, R.; KIS, A.; MAREGA JR, E. Enhancing light-matter interaction in MoS_2 monolayer deposited on metallic nanostructures. In: META, THE INTERNATIONAL CONFERENCE ON METAMATERIALS, PHOTONIC CRYSTALS AND PLASMONICS. Paris. France, 2023.

LEMES. M. F. S.; PIMENTA, A. C. S.; MAREGA, G. M.; CHIESA, R.; KIS, A.; MAREGA JR, E. Second-harmonic generation enhancement of monolayer molybdenum disulfide from gold plasmonic gratings. In: XXI BRAZIL MRS MEETING. Maceió. Alagoas, 2023.

LEMES. M. F. S.; PIMENTA, A. C. S.; MAREGA, G. M.; CHIESA, R.; KIS, A.; MAREGA JR, E. Investigating Raman scattering of MoS_2 monolayer on Au plasmonic grating. In: XXI BRAZIL MRS MEETING. Maceió. Alagoas, 2023.